Trinity College Dublin, The University of Dublin

Transmission Electron Microscopy and Spectroscopy of Carbon-based Nanomaterials

PhD Thesis

Ehsan Rezvani

ASIN Group
School of Chemistry
Faculty of Engineering, Mathematics and Science

January 2016

Declaration of Authorship

I, Ehsan Rezvani, declare that this thesis titled, 'Transmission Electron Microscopy and Spectroscopy of Carbon-based Nanomaterials' and the work presented in it are my own. I confirm that:

- This work was done wholly or mainly while in candidature for a research degree at this University.
- Where any part of this thesis has previously been submitted for a degree or any other qualification at this University or any other institution, this has been clearly stated.
- Where I have consulted the published work of others, this is always clearly attributed.
- Where I have quoted from the work of others, the source is always given. With the exception of such quotations, this thesis is entirely my own work.
- I have acknowledged all main sources of help.
- Where the thesis is based on work done by myself jointly with others, I have made clear exactly what was done by others and what I have contributed myself.

Signed:

Date:

TRINITY COLLEGE DUBLIN, THE UNIVERSITY OF DUBLIN

Abstract

Faculty of Engineering, Mathematics and Science
School of Chemistry

Doctor of Philosophy

Transmission Electron Microscopy and Spectroscopy of Carbon-based Nanomaterials

by Ehsan Rezvani

Carbon-based nanomaterials, such as graphene, Carbon Nanotubes and fullerenes, have attracted a great deal of interest from the materials research community; especially in electronic and sensing applications. Despite all these outstanding properties, these materials pose significant challenges to the established characterisation techniques. Transmission electron microscopy (TEM) is considered as a powerful tool to tackle this challenge due to its capability to achieve images of atomic-scale resolution. Nonetheless, a key requirement for efficient application of TEM, is sample quality. To meet this need, in the first part of this work, modification of the CVD growth of graphene via catalyst optimisation was investigated and is reported in a dedicated chapter. We show that chromium can be used to successfully obtain entirely monolayer graphene films. The second part of this study, comprises HRTEM/EELS investigation of plasma-functionalised graphene; where we propose application of these two methods as a tool to monitor the quality of plasma-treated graphene sheets. We then move on to explore the bonding properties of isotope-enriched graphene studied by Aberration-Corrected TEM. The results show that the bonds in isotope graphene are stronger and remarkably longer comparing to those of "normal" graphene.

Acknowledgements

There are a number of people without whom this thesis might not have been written,and to whom I'm greatly indebted.

I thank my supervisor, Prof. Georg S. Duesberg for his guidance and support.

I would like to thank everyone in the ASIN Group for their support, continual helpful scientific discussions as well as great humour! Their attitude has made coming to work every day for the last four years a very positive and enjoyable experience, and I have always appreciated the lengths that they have all gone to whenever I needed help. Thanks to Hugo and Niall who have been true friends and invaluable sources of support and advice throughout my study. Thanks to Toby for being a wonderful source of reference and aid endlessly and patiently in all matters. Nina is thanked for her assistance with XPS and her support. Thanks to Shishir a former group member, who generously thought me how to design an experiment properly and showed me the stepping stones of graphene research. Kay and Hye-Young are greatly acknowledged for their constant help and advice on electrical measurements and analysis. Without you,none of those electrical data would have got obtained. Sinéad and Maria are thanked for their kind support. Thanks to Riley for his technical assistance without whose hands-on skills, isotope graphene experiment would not be feasible. Thanks to Brendan O'Dowd for his generous helps with schematics and and software issues, regularly putting aside his work to help me for as long as was needed. Christian is thanked for being a good friend..

I have greatly enjoyed working at CRANN as well as Advanced Microscopy Lab (AML). In both institutions there is a wealth of experience and advice. I'd like to thank all the staff and researchers here who contribute to the wonderful working environment.

Finally, special and profound thanks to my parents who have been a great source of encouragement and inspiration to me throughout my life. An hour phone conversation with them at a crucial time, helped me find the strength to continue my work here and helped me come to the decision, once and for all, that obtaining this degree would not be the first challenge in my life that I would not rise to meet. And also for the myriad of ways in which always they've actively supported me in my determination to find and realise my potential and to make this happen. I'd also like to thank my brothers who offered invaluable support and humour over the years. Words can't express how much I love you all and how grateful I am for your support. Without you four, I most certainly would not be where I am today.

Contents

Abbreviations

AC-TEM	**A**berration **C**orrected **T**ransmission **E**lectron **M**icroscope/y
AFM	**A**tomic **F**orce **M**icroscope/y
APS	**A**mmonium **P**er **S**ulfate
BF-TEM	**B**right **F**ield **T**ransmission **E**lectron **M**icroscopy
BSE	**B**ack **S**cattered **E**lectron
CBED	**C**onvergent **B**eam **E**lectron **D**iffraction
CCD	**C**harge **C**oupled **D**evice
CNT	**C**arbon **N**ano **T**ube
CVD	**C**hemical **V**apour **D**eposition
DFT	**D**ensity **F**unctional **T**heory
DF-TEM	**D**ark **F**ield **T**ransmission **E**lectron **M**icroscopy
DLC	**D**iamond **L**ike **C**arbon
ED	**E**lectron **D**iffraction
EDP	**E**lectron **D**iffraction **P**attern
EDX	**E**nergy **D**ispersive **X**-ray
EELS	**E**lectron **E**nergy **L**oss **S**pectroscopy
EFTEM	**E**nergy **F**iltered **T**ransmission **E**lectron **M**icroscopy
EKLs	**E**xtended **KLs**
ELNES	**E**nergy **L**oss **N**ear **E**dge **S**tructure
EXELFS	**EX**tended **E**nergy **L**oss **F**ine **S**tructure
FFT	**F**ast **F**ourier **T**ransform
FWHM	**F**ull **W**idth **H**alf **M**aximum
GC	**G**lassy **C**arbon
GFET	**G**raphene **F**ield **E**ffect **T**ransistor
GRIP	**G**raphene **R**esist **I**nterlacing **P**rocess

HAADF	**H**igh **A**nnular **A**ngle **D**ark **F**ield
HOPG	**H**ighly **O**rdered **P**yrolytic **G**raphite
HRTEM	**H**igh **R**esolution **T**ransmission **E**lectron **M**icroscopy
HV	**H**igh **V**acuum
IR	**I**nfra **R**ed
KIE	**K**inetic **I**sotope **E**ffect
KLs	**KL**ein edges
KLDs	**KL**ein **D**oublets
MFC	**M**ass **F**low **C**ontroller
NC	**N**itro **C**ellulose
NP	**N**ano **P**article
PPF	**P**yrolysed **P**otoresist **F**ilm
PyC	**P**yrolytic **C**arbon
SAED	**S**elected **A**rea **E**lectron **D**iffraction
SE	**S**econdary **E**lectron
SEM	**S**canning **E**lectron **M**icroscope/y
STEM	**S**canning **T**ransmission **E**lectron **M**icroscope/y
TEM	**T**ransmission **E**lectron **M**icroscope/y
XPS	**X**-ray **P**hotoelectron **S**pectroscopy
ZLP	**Z**ero **L**oss **P**eak

List of Publications

[1] **E. Rezvani**, T. Hallam, N. McEvoy, N.C. Berner and G.S. Duesberg. Optimisation of copper catalyst by the addition of chromium for the chemical vapour deposition growth of monolayer graphene. *Carbon*, 95: 789-793, 2015. DOI: `http://dx.doi.org/10.1016/j.carbon.2015.08.114`.

[2] **E. Rezvani**, J.S. Kim, *et al.*. Aberration-corrected TEM study of isotope graphene. *in preparation*, 2015.

[3] J. Conroy, N.K. Verma, R.J. Smith, **E. Rezvani**, G.S. Duesberg, J.N. Coleman, Y. Volkov. *arXiv preprint arXiv:1406.2497*, 2014. URL: `http://arxiv.org/abs/1406.2497`.

[4] R. Gatensby, N. McEvoy, K. Lee, T. Hallam, N.C. Berner, **E. Rezvani**, S. Winters, M. O'Brien, G.S. Duesberg. Controlled synthesis of transition metal dichalcogenide thin films for electronic applications. *Applied Surface Science*, 297: 139-146, 2014. DOI: `http://dx.doi.org/10.1016/j.apsusc.2014.01.103`.

[5] C. Yim, N. McEvoy, H-Y. Kim, **E. Rezvani**, G.S. Duesberg. Investigation of the Interfaces in Schottky Diodes Using Equivalent Circuit Models. *ACS Applied Materials & Interfaces*, 5 (15): 6951-6958, 2013. DOI: `http://dx.doi.org/10.1021/am400963x`.

[6] A.K. Nanjundan, H. Nolan, N. McEvoy, **E. Rezvani**, *et al.*. Plasma-assisted simultaneous reduction and nitrogen doping of graphene oxide nanosheets. *Journal of Materials Chemistry A*, 1 (14): 4431-4435, 2013. DOI: `http://dx.doi.org/10.1039/c3ta10337d`.

[7] C. Yim, **E. Rezvani**, S. Kumar, N. McEvoy, G.S. Duesberg. Investigation of carbon–silicon Schottky barrier diodes. *physica status solidi (b)*, 249 (12): 2553-2557, 2012. DOI: `http://dx.doi.org/10.1002/pssb.201200106`.

[8] C. Yim, N. McEvoy, **E. Rezvani**, S. Kumar, G.S. Duesberg. Carbon–silicon schottky barrier diodes. *Small*, 8 (9): 1360-1364. DOI: `http://dx.doi.org/10.1002/smll.201101996`.

[9] S. Kumar, **E. Rezvani**, V. Nicolosi, G.S. Duesberg. Graphene resist interlacing process for versatile fabrication of free-standing graphene. *Nanotechnology*, 23 (14): 145302, 2012. DOI: `http://dx.doi.org/10.1088/0957-4484/23/14/145302`.

[10] N. McEvoy, N. Peltekis, S. Kumar, **E. Rezvani**, H. Nolan, G.P. Keeley, W.J. Blau, G.S. Duesberg. Synthesis and analysis of thin conducting pyrolytic carbon films. *Carbon*, 50 (3): 1216-1226, 2012. DOI: `http://dx.doi.org/10.1016/j.carbon.2011.10.036`.

[11] G.P. Keeley, N. McEvoy, H. Nolan, S. Kumar, **E. Rezvani**, M. Holzinger, S. Cosnier, G.S. Duesberg. Simultaneous electrochemical determination of dopamine and paracetamol based on thin pyrolytic carbon films. *Analytical Methods*, 4 (7): 2048-2053, 2012. DOI: `http://dx.doi.org/10.1039/C2AY25156F`.

[12] S. Kumar, N. McEvoy, H-Y. Kim, K. Lee, N. Peltekis, **E. Rezvani**, H. Nolan, A. Weidlich, R. Daly, G.S. Duesberg. CVD growth and processing of graphene for electronic applications. *physica status solidi (b)*, 248 (11): 2604-2608, 2011. DOI: `http://dx.doi.org/10.1002/pssb.201100179`.

Conference Presentations

Talks

[1] Title: Electron Microscopy and Spectroscopy of Plasma-Functionalised CVD graphene. E-MRS Spring Meeting, Lille, France - 2014

[2] Graphesp^{2014} Graphene Flagship Meeting, Lanzarote, Spain - 2014

Posters

[1] AMBER Centre Launch, Dublin-2013 (selected as top 8 posters)

[2] Graphene 2013 Conference - Bilbao, Spain

[3] Smart Surfaces, Dublin-2012

[4] Nanoweek Conference, Dublin-2011

Collaborative Posters

[1] Patterned single-layer graphene with metamaterial behavior in the THz range, IRMMW-THz, Arizona - 2014

[2] Detection of critical functional responses to grapheme-based thin films in primary human phagocytes, 14th International Conference on the Science and Application of Nanotubes, Finland - 2013

[3] Multimodal biocompatibility assessment of graphene-based thin films, Nanoweek conference, Dublin - 2012

[4] Comparative biosafety analysis of next generation flexible nanoimprinted thin films, IMM annual meeting, Dublin - 2012

Dedicated to my parents

Chapter 1

Introduction and Theoretical Background

Carbon is able to form strong covalent bonds with itself and other atoms. It can also adopt a number of allotropes, diamond and graphite being two of the most famous ones (see Figure 1.1 (a) & (b)). The discovery of the quasi zero-dimensional C_{60} molecule (Figure 1.1 (c)) by Curl, Kroto and Smalley in 1985 [1] (for which they were awarded a Nobel Prize) opened a new family of carbon allotropes, known as Fullerenes which includes C_{60}, C_{70}, C_{82}, etc. Following on from this, Iijima reported the discovery of a one-dimensional graphitic carbon structure, now known as a Carbon Nanotubes (CNT) (see Figure 1.1 (d), in 1991 [2]. The most recent discovery, which brought its discoverers the Nobel Prize in 2010, was a single isolated graphitic layer known as graphene [3] (see Figure 1.1 (e)).

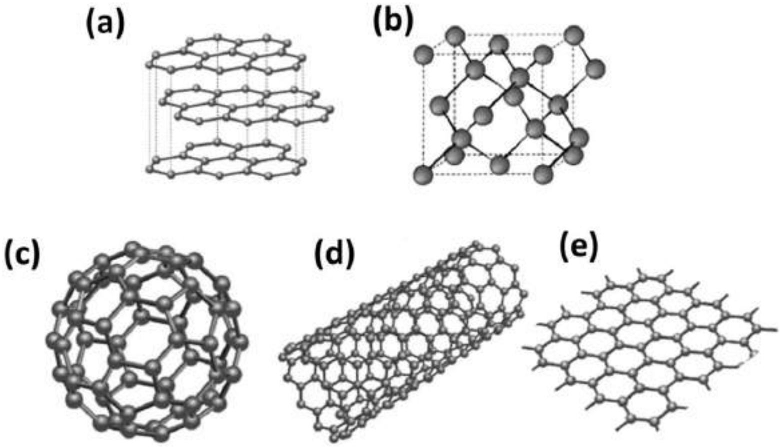

Figure 1.1 Schematic representation of various carbon allotropes. (a) Graphite, (b) diamond, (c) fullerene, (d) CNT and (e) graphene (adapted from [4]).

Other carbon forms include Diamond-Like Carbon (DLC), amorphous Carbon (a-C), Glassy Carbon (GC), Pyrolytic Carbon (PyC) and so forth. The carbon atoms in these various allotropes can bond in different hybridisation configurations which can be pure sp, sp^2, sp^3 or a mixture of them. Diamond has pure sp^3 bonds whereas graphite and graphene have pure sp^2 bonds (with the exception of atoms at the edges of such structures which are sp^3-hybridised). Amorphous carbon holds a mixture of sp^2-sp^3 bonds, with varying amounts. The ratio between the sp^2 and sp^3 bonds present in a material plays an important role in determining its (electrical and mechanical) properties. Therefore it is important to characterise the relative proportions of these bonds [5]. The disordered members of the nanocarbon family are typically produced by means of evaporation, sputtering, or pyrolysis of carbonaceous materials. For instance, pyrolysis of polymers produces what is known as GC, while Chemical Vapour Deposition (CVD) of hydrocarbons on appropriate materials yields Pyrolytic Carbon (PyC). The crystalline members, namely graphite, fullerenes, CNTs and graphene are typically formed at high temperatures and in the presence of catalysts, where conditions for the growth of larger crystals are met.

1.1 Graphene

Before the experimental realisation of graphene by Geim and Novoselv in 2004, scientists believed that such a 2D structure would be thermodynamically unstable [3]. Graphene was known to be an integral part of 3D Graphite but it was assumed that independent graphene sheets could not exist (in a free state). It was thought that the melting temperature of the films would rapidly decrease with decreasing thickness and they would become unstable (segregate into islands or decompose) at a thickness on the order of a few tens of atomic layers. Graphene was largely considered to be an “academic material” and that graphene was believed to have no relevance in real applications. The isolation of monolayer graphene put an end to all the previously accepted theories and showed that 2D materials can indeed exist. To account for this existence, it was initially suggested that that graphene forms ripples intrinsically [6], leading to sp^3 bonding where there will be roughly 6-8 nearest neighbours vs. 3 or 4 in a 2D configuration. However, later research found that in fact unrecognised adsorbates [7] on the graphene had led to the false impression of “intrinsic” rippled behaviour in graphene. The of most small-scale “corrugations” stems from the system trying to minimise the energy cost of the waves by maximising their wavelength. Moreover, small but strong bonds in graphene ensure that thermal fluctuations can not lead to the generation of dislocation or other crystal defects even at elevated temperatures [8].

1.1.1 Properties

The unique electronic properties of graphene (ballistic charge carriers and high mobility) have inspired a great deal of research and interest in this material. What makes graphene special is mainly its unique electronic properties. Carbon atoms have a total number of six electrons with electron configuration of $1s^2 2s^2 2p^2$; two in the inner shell and four in the outer shell. In a graphene sheet, there are four orbitals for bonding: three sp^2 and one p_z. Each carbon atom is bonded to its three closest neighbours via strong in-plane σ-bonds formed from sp^2-hybridised orbitals. The sp^2 orbitals yield a trigonal planar structure. The corresponding Bravais lattice to this planar hexagonal structure has two atoms per unit cell. The remaining unhybridised p_z orbitals that are extending out of the plane overlap to form π-bonds. The unit cell of graphene contains two π orbitals that disperse to form two π bands (analogous to valence and conduction band). The most important feature of these π bands is that, the gap between them closes at the corners of Brillouin zone, implying the charge carriers in graphene are massless. As a result, the electrons in graphene behave very much like photons and can travel without scattering as fast as approximately 1/300 of speed of light. That is why graphene is an extraordinary conductor of electricity, with an intrinsic charge carrier mobility at room temperature of 200,000 $cm^2/V.s$ [9], higher than any other known material.

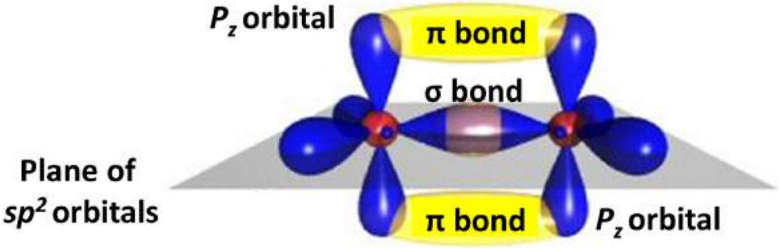

Figure 1.2 Schematic representation of σ and π bonds in graphene (adapted from [10]).

As well as its electronic properties, the mechanical properties of graphene have also attracted considerable attention. The outstanding mechanical properties of graphene are attributed to the strong network of σ-bonds in a graphene sheet. It has been reported that graphene has a Young's modulus of 1 TPa and an intrinsic strength of 130 GPa and large spring constant of 1-5 N/m [11–13].

The thermal properties of graphene are equally exceptional. Graphene has an extremely high thermal conductivity up to 5000 W/m.K [14], 20 times higher than that of copper. Moreover, graphene has a large negative thermal expansion coefficient of -6×10^{-6} [15], 5-10 times greater than that in graphite.

Linked with its superior electronic properties, optical properties of graphene has also amazed the scientific community. Despite being only one atom-thick, it is visible to the naked eye when placed on SiO_2/Si wafer; and absorbs 2.3 % of the light that passes through it [16]. Due to all these superior properties, graphene has been heralded as a revolutioniser in various research fields and sectors, e.g. energy, electronics, health and costruction. If graphene holds its promise, it can be the material of the century.

1.1.2 Synthesis of Graphene

There are four main approaches to produce graphene: (1) exfoliation (mechanical or chemical), (2) CVD on catalytic transition metal substrates, (3) epitaxial growth on substrates such as silicon carbide and (4) molecular assembly [17] (see Figure 1.3).

Mechanical exfoliation is the simplest production method which involves peeling off layers of Highly-Ordered Pyrolytic Graphite (HOPG) one by one, for instance by means of a cello-tape [3]. This method produces the highest quality graphene and therefore is most suitable for lab-scale production where investigation of fundamental physics of graphene is intended. However, this technique has a very low yield and the thickness, size and distribution of the obtained graphene flakes are not controllable; which make this method unsuitable for large-scale production.

Another technique to produce graphene at low cost is by chemical exfoliation. This technique uses a surfactant and sonication energy (or shear mixing) to separate layers of high quality graphite [18, 19]. This method can produce reasonably good quality graphene at commercial scale. Nonetheless, the resulting graphene flakes are typically multilayer and their size does not exceed few hundred micrometres at best. Since this method is a solution-based technique, it is mainly useful for making graphene composites, supercapacitors, printed electronics and chemical applications.

Transfer-free wafer-scale graphene growth is possible by the thermal decomposition of silicon carbide (SiC) [20–22]. Production of epitaxial graphene via this approach involves sublimation of silicon from a SiC substrate at very high temperature to obtain graphene layers. When the SiC is heated in vacuum or in an argon atmosphere, only the silicon atoms leave the surface due to the difference in the vapour pressures of silicon and carbon, and the remaining carbon atoms form epitaxial graphene spontaneously on the surface. This graphene produced by this method is of high quality but it is not really cost-effective due to the extremely high process temperature and the cost of SiC.

The molecular assembly or the bottom-up approach is another way to obtain graphene which consists of implementation of chemical synthesis methods to stitch the building blocks together which are typically molecules with structures similar to graphene such as benzene [23]. Although this technique has a low yield associated with it.

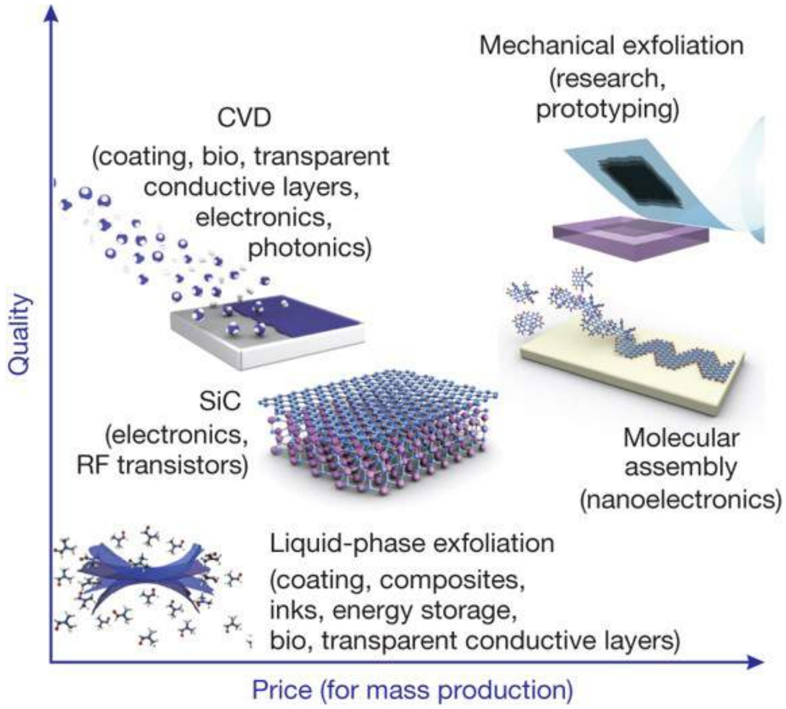

Figure 1.3 Diagrammatic comparison of production cost and the associated quality of various production methods of graphene (adapted from [17]).

Finally, the most promising larger-scale graphene growth technique is CVD on a metal substrate. Briefly, a carbon-containing gas such as methane, ethane or propane, decomposes at high-temperatures and turns into graphene (see section 1.3 in this Chapter for detailed description) on the catalytic metal surface [24]. The CVD technique can provide wafer-scale graphene at low cost, which is appropriate for industrial applications. Growing large-area single crystal graphene without grain boundaries, and removing defects and impurities due to the transfer process are the remaining bottlenecks for complete realisation of industrial application [25, 26].

Figure 1.3 compares (arbitrarily) graphene production methods and their associated cost and quality. Each of these techniques has its own cost and quality figure of merit and hence will be best suited for particular applications. The production method used throughout the current study was CVD technique. The CVD technique will be discussed in Chapter 2 in more details.

1.2 Crystal Structure

Graphene is referred to as the mother of all the other graphitic carbon-based nanostructures, including graphite. Graphite has a three-dimensional layered structure, consisting of graphene layers stacked on top of each other, and these layers are held to the layers above and below by relatively weak Van der Waals forces. These stacked 2D layers are graphene sheets. The atoms in graphene are laid out flat and each layer is made of hexagonal rings of carbon giving a honeycomb-like appearance. This honeycomb lattice is not a Bravais lattice because two neighbouring sites are inequivalent [27, 28]. Figure 1.4 illustrates the graphene's crystal lattice. A carbon atom located on the A sublattice, has three nearest neighbours in north-east, north-west and south directions; whereas a site on the B sub-lattice has nearest neighbours in north, south-west and south-east directions. The a_1 and a_2 denote the real space lattice vectors in graphene.

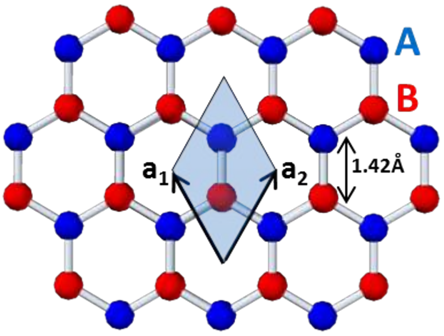

Figure 1.4 Schematic illustration of honeycomb lattice of graphene.

Both A and B sub-lattices however, are triangular Bravais lattices, and one may view the honeycomb lattice as a triangular Bravais lattice with a two-atom basis (A and B). The distance between nearest neighbour carbon atoms is 0.142 nm.

As mentioned above, graphite consists of stacked graphene layers. In the case of crystalline (ordered) graphite, graphene layers can take on various stacking sequence. To illustrate the ordering of graphene layers in crystalline graphite, we first consider only two graphene layers (bilayer graphene). The stacking is such that there are atoms in the upper layer placed at the hexagon centres of the lower layer. The layers are, thus, translated with respect to each other, and one can identify two different patterns: (I) If the sign of the translation vector alternates, i.e. δ, -δ, δ, etc. the more stable hexagonal stacking (also known as AB or Bernal stacking) is produced (see Figure 1.5 (b) & (c)). (II) If all the layers are translated with respect to their lower neighbour by the displacement vector of δ, the less stable rhombohedral (or ABC stacking) is obtained (see Figure 1.5 (d)). This type of stacking was first identified by observation of extra lines in the XRD pattern of natural graphite that had not seen before [29]. In both cases, the stacking distance between the graphene sheets is 0.3354 nm. In principle, it is possible to have some randomness in the stacking, i.e. ABC parts may randomly substitute AB parts. In nature, 80% is found to be in AB stacking, 16% in the ABC stacking order with the remaining 4% exhibiting a disordered or turbostratic stacking [30].

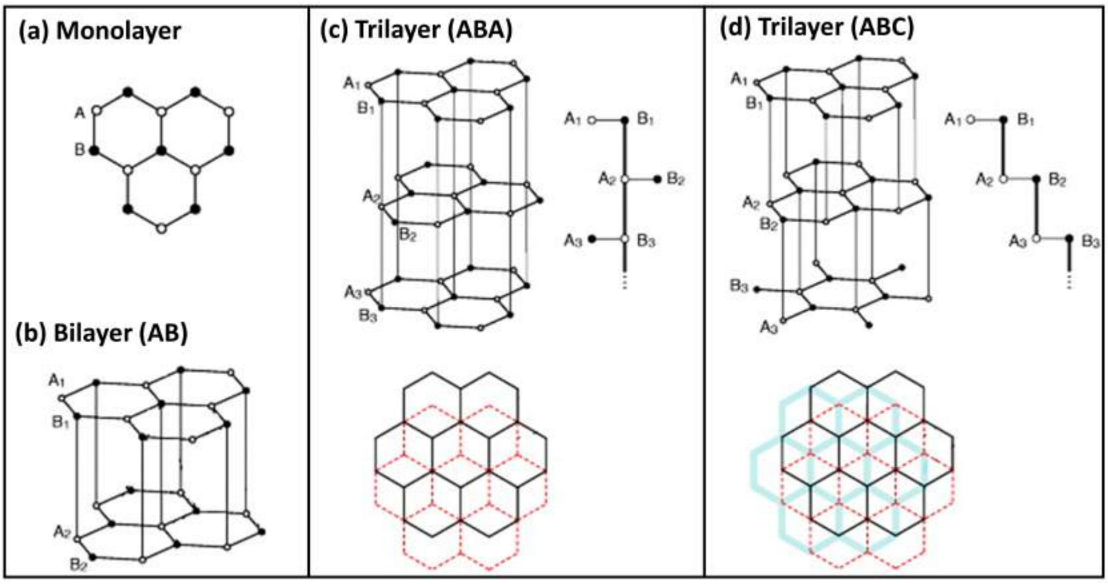

Figure 1.5 Lattice structures of (a) monolayer graphene, (b) AB-stacked bilayer graphene, (c) ABA-stacked multilayer graphene and (d) ABC-stacked multilayer graphene (adapted from [31]).

In the case of turbostratic graphite, one may distinguish translational disorder from rotational disorder in the stacking which is a crystallographic defect. Generally, the graphene layers in turbostratic graphite are loosely bonded together compared to crystalline graphite. The simplest case is twisted bilayer graphene, in which the two graphene layers are rotated in relation to one another with an angle of θ.

The stacking sequence plays an important role in tailoring the electronic and optical properties of graphene. For instance, AB-stacked bilayer graphene has a tunable bandgap [30], whereas twisted bilayer graphene shows a multitude of exciting new properties such as the emergence of different phonon branches and modulation of interlayer coupling and hence, a completely new electronic structure (e.g. generation of massless Dirac fermions) [32, 33]. Twisted bilayer graphene can be made via three methods: (1) From SiC, (2) CVD, (3) Folding and (4) Stacking graphene layers one atop the other [34]. However, only the last method seems to be suitable for controllable production of graphene but suffers from interlayer contamination. In our group a method for clean stacking of graphene layers has been developed [35] but is not discussed here. These examples highlight the importance of the identification of stacking type and order in multilayer graphene and crystalline graphite, to ensure the desired properties and ultimately reliable performance as a commercial product.

1.3 Growth

1.3.1 Theoretical Treatment

Nucleation is a crucial stage during the growth process; therefore, before discussing the case of graphite and graphene growth, a brief theoretical background treatment is presented. The most standard and simple theory that explains the nucleation process is called *classical nucleation theory*. This theory has been successfully applied to describe the graphene nucleation process on the surface of transition metals [36] as well as the growth process of other graphitic thin films [37]. This theory consists of two parts: the thermodynamics part, which deals with the energy evolution upon nucleation, and kinetics that describes the rate at which this nucleation occurs. The thermodynamic part of the classical theory was first developed by J.W. Gibbs in late 19th century, where he first outlined the concept of what is now known as *Gibbs energy*, and how his equation could predict the behaviour of systems. The Gibbs energy is the energy associated with a chemical reaction and the change in the Gibbs energy, ΔG, is used to predict the direction of the reaction at a given pressure and temperature. At constant pressure and temperature, if ΔG is positive, then the reaction is non-spontaneous (i.e., an external energy is necessary for the reaction to occur), and if it is negative, then it is spontaneous (occurs without external energy input).

In most nucleation processes including graphene, there is a substrate on which the reaction happens. To account for this, two types of nucleation processes are discussed within the classical nucleation theory; homogeneous nucleation, that occurs away from a surface and, heterogeneous nucleation which happens on a surface. Heterogeneous nucleation occurs much more often and at a faster rate than the homogeneous nucleation. Heterogeneous nucleation takes place at preferential sites such as phase boundaries, surfaces or impurities. This is due to the fact that in defect sites/surfaces, a less regular bonding present which leads to a higher energy state, making them reactive. This diminishes the nucleation energy barrier and facilitates nucleation. This holds true for the graphene nucleation on the surface of metal substrates; as has been shown experimentally by various group working on CVD graphene including our own group (see Chapter 5 for empirical examples).

1.3.2 CVD Process

Most of the practical applications conceived for graphene, such as microelectronics, optoelectronics, supercapacitors and so forth, require large-area high-quality graphene with minimal structural defects [25]. Among all the previously-discussed fabrication routes, CVD synthesis can be considered the best option to serve this purpose. The preparation of graphite from heterogeneous catalysis on transition metals has been known for years. The first successful CVD synthesis of large-area few-layer graphene was reported in 2008 [38]. Since then, the CVD synthesis has evolved to a scalable and reliable production method of large area graphene. Synthesis of large area and high quality monolayer graphene has been demonstrated by many groups worldwide. The CVD process of graphene on copper was used throughout this work which is elaborated below.

Hydrocarbon-based gas precursors, methane CH_4 being the most mentioned, are commonly used as carbon feedstock for graphene growth. Similar to catalytic graphitisation process, different transition metal catalysts are used to reduce the temperature of methane's decomposition. Among transition metals used for graphene growth, copper and nickel result in high quality graphene and hence, have been most widely studied [39–41]. Therefore, we can view the graphene growth process, as a heterogeneous catalytic chemical reaction, in which the metal acts as both the substrate and the catalyst itself. This means that, as graphene grows over the metal substrate, it reduces the catalytic activity of the metal as it hinders the *catalyst* surface exposure to the incoming carbon species. Essentially, if the progress of growth process depends on only surface activated phenomena (e.g. adsorption, decomposition and diffusion of active carbon species), as soon as the catalyst surface is completely blocked (monolayer graphene), the graphene growth process should stop. This is known a "self-limiting" effect and has been observed in copper-catalysed graphene growth, mainly due to the negligible solubility of carbon in copper [24, 39]. On the contrary, for metals that have higher carbon solubility such as nickel, it has been shown that the bulk processes also play a role [38, 42].

The overall processes of CH_4 decomposition on the copper surface during graphene growth are: (1) active CH_4 is broken down into carbon species such as CH_x (x=0–3) through dissociative chemisorption on the copper surface, and diffuse on the copper surface; (2) once the increasing dynamic concentration of carbon species reaches critical supersaturation level, the nucleation of graphene takes place; (3) part of the supersaturated carbon species with enough energy reach the graphene domain edge and attach to the graphene domain; (4) the CH_x species at the unstable graphene edge detach themselves from graphene, and form dissociative carbon species; (5) Dissociative carbon species combine with hydrogen and are desorbed from the copper surface. Figure 1.6 diagrammatically shows these steps.

Reaction Mechanism

The overall reaction formula of graphene growth on the copper from methane in the presence of H_2 is as follows:

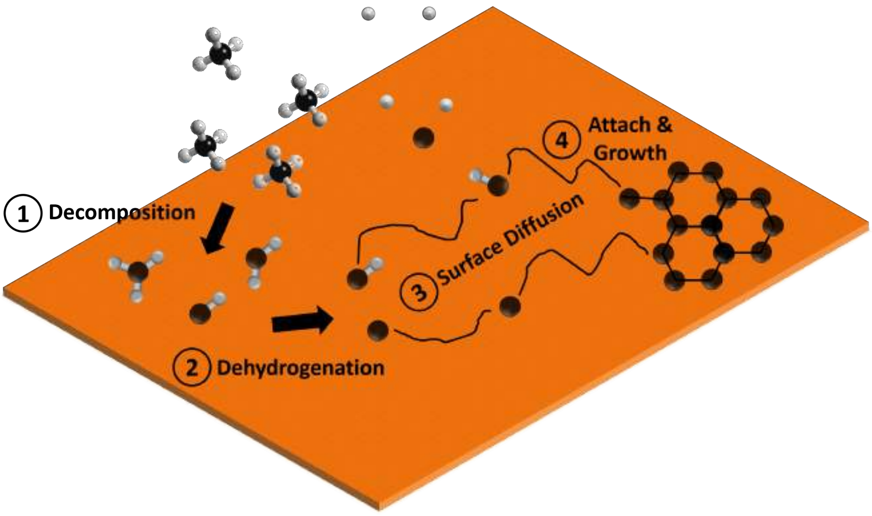

Figure 1.6 Reaction pathways and the active carbon species during CVD growth of graphene on copper from methane as carbon feedstock.

$$CH_4(g) \xrightleftharpoons{Cu} \underset{\text{Graphene}}{C(s)} + 2\,H_2(g) \tag{1.1}$$

However, this overall reaction can be split into more reversible reactions; for instance the following reactions have been proposed to occur [43]:

$$CH_4(g) \xrightleftharpoons{Cu} C(ads) + 4\,H^\bullet \tag{1.2}$$

$$4\,H^\bullet \xrightleftharpoons{Cu} 2\,H_2(g) \tag{1.3}$$

$$C(ads) \xrightleftharpoons{Cu} \underset{\text{Graphene}}{C(s)} \tag{1.4}$$

As can be seen, H_2 appears on the right side of the reversible equation (1.1), which indicates that the partial pressure of H_2 in the gas precursor mixture plays a crucial role in the dynamics of the CVD process of graphene. According to Le Chatelier's principle, reducing the partial pressure of H_2 cause the reaction to proceed towards the product or the formation of graphene. Conversely, an increase in the partial pressure of H_2 in the reactor will cause the reaction to proceeds to the left or etching of graphene. Furthermore, the dominant form of active carbon species on the copper surface during the growth is also greatly influenced by the partial pressure of H_2. Thus, the amount of H_2 available extensively affects the growth behaviour of graphene as evidenced in many experiments [44–46]. The detailed investigation of the effect of H_2 during CVD of graphene is beyond the scope of this chapter; nonetheless some aspects of this topic are outlined below.

During the ramping and annealing steps, the catalyst surface is reduced by molecular hydrogen, H_2. This also leads to the exposure of the pure metal surface to H_2 which in turn gives rise to the dissociative chemisorption of H_2 on the metal surface. Under typical graphene growth temperature, copper exhibits a significant hydrogen solubility [47, 48]. In this case, saturation would be necessary to desorb molecular hydrogen from copper surface. Therefore, before exposure of the catalyst to hydrocarbons, a surface and/or subsurface partially covered with atomic hydrogen could be the starting point [49]. After exposure to hydrocarbons (diluted in molecular hydrogen in most cases), the next step to discuss is the competitive process between the dissociative chemisorption of H_2 and the physical adsorption and dehydrogenation of CH_4 on available surface sites of the catalyst. During the next steps CH_4 catalytic decomposition takes place on the metal surface. The precise moment when the precursor dehydrogenation is completed remains an open question.

It has been shown theoretically that [50], under the conditions of most CVD experiments (including the experimental set-up used in this work), the $C^\bullet$ monomer and $CH^\bullet$ are two competitive species on the copper, Ir and Rh surfaces. They are more active than ${CH_2}^\bullet$ and ${CH_3}^\bullet$ and thus the growth of graphene should be mainly due to the attachment of $C^\bullet$ monomers and $CH^\bullet$ onto the edge of graphene domains. In particular for the copper surface, $CH^\bullet$ is a very active carbon species and the combination of two $CH^\bullet$ species may induce the formation of C_2H_2, namely, $CH^\bullet + CH^\bullet \longrightarrow C_2H_2$.

Understanding the CVD growth mechanism and the reaction pathways, is crucial for obtaining high quality large area graphene and ultimately, realisation of commercial products made of CVD-grown graphene [25]. There are still many open questions to be answered in this field, which by itself promises a great potential for future studies.

1.3.3 Importance of Layer Number

As mentioned previously in this Chapter, one of the factors that strongly affects the electronic properties of graphene, is the number of layers. [51–53]. Although monolayer graphene has several demonstrated applications (e.g. composites, analogue electronics and energy conversion and catalysis), for true realisation of its application in digital electronics, bandgap opening is one of the main goals [54]. A number of gap creation strategies have been proposed and are being explored; two of which can be defined as: (a) to tailor the production process itself, such that to achieve the graphene with desired layer number. These strategies have garnered more interest and have therefore been more studied. (b) Attempting to modify the properties of graphene through post-production treatments, such as functionalisation processes; or CVD method for instance, offers the opportunity to precisely control the layer number of graphene by tuning the parameters of the growth [55, 55, 56]. In line with the second strategy, in this work, a novel method for obtaining exclusively monolayer graphene is presented. This is done by modification of the metal catalyst used for CVD growth. The details of this work are presented in outlined in Chapter 4. With regards the second strategy, our group has developed a good knowledge and expertise in plasma functionalisation of graphene and related systems. In this thesis, TEM study of such systems is elaborated in Chapter 6.

1.4 Electron Microscopy

Electron optics is the core to most of the works carried out in this thesis. Within this framework, electron beam-specimen interactions form the basis for different characterisation techniques described in this Chapter. Thus, in this section, first a brief overview of electron optics and the reason why electrons are used as a "probe" is outlined. Then, various signals produced upon interaction of incident beam with the sample are described.

1.4.1 Electron Optics Background

Electron microscopy is a characterisation technique that uses a focused beam of energetic electrons produced by an electron microscope, to generate an image from the sample or, to analyse the crystal structure and composition of the sample. The resolution of electron microscope is significantly higher than light microscopes because the electron has a much smaller wavelength than light. Mathematically, the resolution in a perfect optical system can be described by Abbe's equation:

$$d = \frac{0.61\lambda}{\mu \sin\beta} \tag{1.5}$$

where λ is wavelength of imaging radiation, μ is the refractive index of the medium between source and lens (which is essentially equals 1 in TEM) and β is half aperture angle in radians. The product of $\mu \sin\beta$ is often called numerical aperture (NA). Some 50 years after Abbe, on the basis of classical and quantum physics, de Broglie proposed an equation reflecting the wave-particle duality of matter. He proposed that the wavelength of moving particles can be calculated based on their mass and energy levels. The general form of de Broglie formula is as follows:

$$\lambda = \frac{h}{m\nu} \tag{1.6}$$

where h is Planck's constant, m is mass of the particle and ν is velocity of the particle (the product is momentum p). When an electron is accelerated in TEM through a potential difference, momentum is transferred to it giving it a kinetic energy eV, which should be in turn equal to the potential energy. With an accelerating voltage V, this kinetic energy can be expressed as follows:

$$eV = 1/2\, m\nu^2 \tag{1.7}$$

Now if we restate the equation 1.6 and substitute for ν in the equation above, then we will have:

$$p = m\nu = (2\, meV)^{1/2} \tag{1.8}$$

Replacing this value in de Broglie equation, we can obtain the relationship between electron wavelength and the accelerating voltage of the microscope. In TEM, the electron velocity is close to the speed of light, c, so that the theory of relativity has to be considered therefore the λ can be expressed by the following equation:

$$\lambda = \frac{h}{\left[2meV\left(1+\frac{eV}{2mc^2}\right)\right]^{1/2}} \tag{1.9}$$

This formula for electron wavelength can be taken into account in the Abbe's equation. This means that if we increase the energy of the detecting source (eV term), its wavelength will decrease, and we can get higher resolution [57–59].

1.4.2 Electron-beam Sample Interactions

Many physical techniques including electron microscopy, rely on the interaction between high energy electrons and the atoms in a solid. There are many possible interactions and some of them are more useful in that they give rise to measurable effects. Essentially, once an accelerated electron beam interacts with a sample, different elastic and inelastic phenomena occur and both electrons and photons are emitted. Depending on their nature, they would carry compositional, topographical and morphological information. Figure 1.7 shows different signals produced upon electron-matter interaction. Each type of electron microscopic technique discussed here, takes advantage of certain kind of interaction. When the incident electrons interact elastically with a sample, they lose a negligible amount of energy in the process. Although the direction of the electrons may be altered, their energy remains essentially the same. For instance, *Backscattered electrons (BSEs)* are generated through elastic interaction with the atoms of the specimen. In this interaction, the trajectory of the beam electrons change but the energy loss will be very small (less than 1 eV). In this case, the larger the atoms, the higher

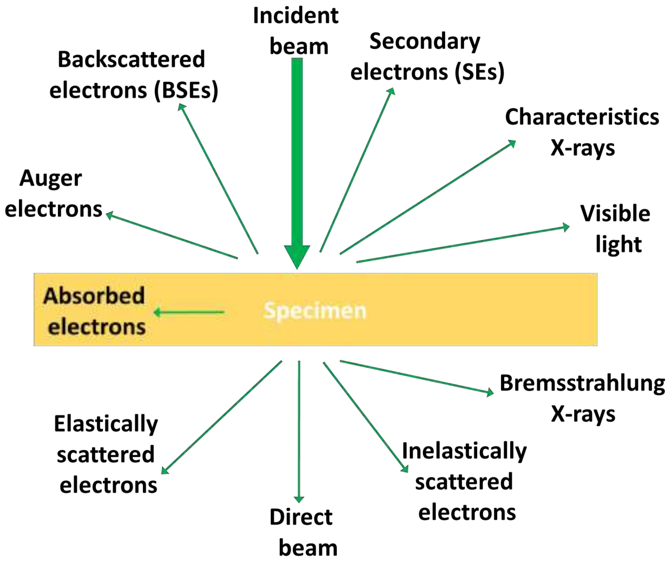

Figure 1.7 Various signals produced upon electron-matter interaction.

the chance of incident electrons to be scattered back out of the sample. By way of analogy, one could imagine the atoms represented as a cluster of snooker balls, and the electron as a smaller ball which is incident on the cluster. From conservation of momentum and the fact the size of an incident electron is fixed, the probability of the smaller ball bouncing backwards is greater the bigger the snooker balls are; which in the case of atoms means higher atomic number. Owing to this specific characteristic, images produced using BSEs show atomic number contrast and, therefore, the features containing higher atomic number elements will appear brighter than those with lower. BSE images are very helpful as they can be used for relatively fast acquisition of high resolution qualitative compositional maps to locate the region of interest in the sample for further quantitative composition analyses.

On the other hand, the inelastic interaction refers to a process by which the incident beam loses energy to an atom. Among these processes are: (a) The excitation of a plasmon. This signal is used in a technique called Electron Energy Loss Spectroscopy (EELS) which is detailed in section 1.5 of this Chapter. (b) The excitation of one or more phonons and thus generation of heat. (c) The excitation of an inner-shell electron. This signal is used in EELS and Auger and X-ray based compositional analyses. (c) The ejection of an electron in the valence band. This signal can be used for imaging as well. The remainder of this section describes different types of electron microscopy and the signals that they use to produce the intended information.

1.4.2.1 Scanning Electron Microscopy

Scanning Electron Microscopy (SEM) is a type of electron microscopy in which a focused beam of electron is scanned over the sample to form an image. When the electron beam hits the sample, both electrons and photons are emitted (heat is also produced). Depending on the depth from which they escape and also their nature, they would carry compositional, topographical and morphological information. Figure 1.8 shows the different signals produced upon electron-matter interaction known as *interaction volume.*

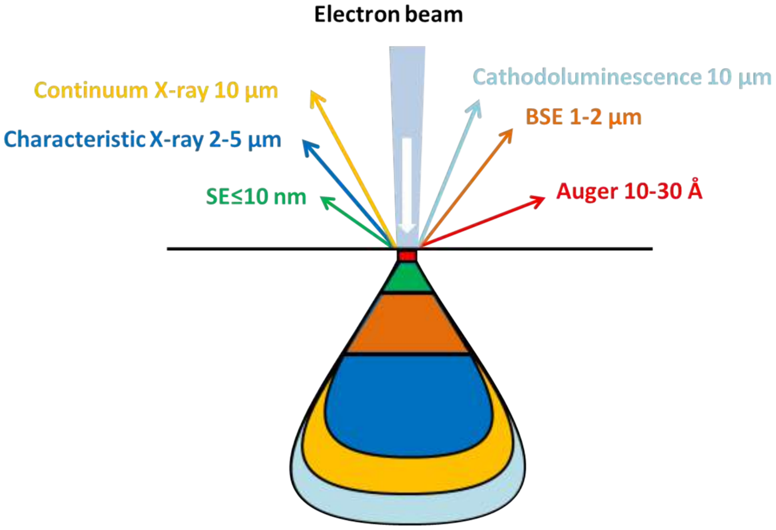

Figure 1.8 Electron beam-sample interaction volume.

The size and shape of the interaction volume depends mainly on three factors: (1) Atomic number: higher atomic number will result in more interaction of electrons with the atoms of the sample or even stop electrons (lower volume). (2) Accelerating voltage: higher voltages will cause electrons to penetrate further in the specimen which generally results in larger volume. (3) Angle of incidence: greater the angle of incidence, the smaller the interaction volume.

Secondary electrons(SEs). These are produced by inelastic interactions of incident electron beam with the specimen. As the electrons strike the sample, they knock out electrons from the valence band of the atoms in the sample. Due to the inelastic nature of this interaction, the trajectory of the incident electrons change slightly and they will lose some of their kinetic energy through this process. These ejected valence electrons have typically energies less than 50 eV and are not composition dependent. Each incident electron can generate several SEs. Due to their low energies, SEs can only escape from below the surface ranging between 2-5 nm and this makes the SEs useful for building morphological and topographical images.

As mentioned above, photons are also generated upon electron-matter interaction and they include **characteristic and continuum X-rays**. Characteristics X-rays are generated when inner shell electrons interact inelastically with the high energy incident electrons and are excited to outer shell orbitals, creating vacancies in the inner shells. Relaxation of electrons from outer shells to fill these inner shell vacancies, causes X-rays to be produced; which are a function of the elements present in the sample. Not all of the energy created via excitation leaves the sample but some of it is absorbed internally or knocks out an outer shell electron (termed Auger electrons). Characteristic X-rays and Auger electrons carry compositional information where the former technique is more of a bulk technique and the latter is surface sensitive. The technique and/or the instrument to carry out X-ray analysis is termed Energy-Dispersive X-ray Spectroscopy (EDS/EDX). Continuous X-rays or bremsstrahlung on the other hand, are produced when a moving incident charge particle (electrons in SEM) is decelerated by another charged particle which in this case is the electrons of atomic nuclei. The strong electromagnetic field of nuclei slows the electrons, generating X-ray with an energy equal to the difference in kinetic energy of the electrons before and after the interaction with the nuclei. This property makes these X-rays not useful for characterisation as they are not specific to the material.

1.4.2.2 Transmission Electron Microscopy

TEM is another type of electron microscope which operates on the same basic principles as a light microscope and slide projector. The major difference, of course, is the wavelength of the illumination used: 450–600nm for visible light but only 3.7×10^{-3} nm for electrons accelerated through 100 kV. This difference not only controls the ultimate resolution of the microscope but also its size and shape. This is described later in this section.

TEM vs. STEM

A TEM can be operated in two modes namely, conventional TEM (CTEM) and scanning TEM (STEM). These two techniques differ primarily in the way they interact with the specimen. The CTEM is a wide-beam technique, which uses a fixed, broad and parallel beam of electrons, that floods the whole area of interest. The image in this technique is formed by an imaging (objective) lens after the thin specimen, and is collected in *parallel* (see Figure 1.9, the scheme on the left)). The STEM was initially developed at about the same time as the TEM, but its evolution was much slower until the work of Crewe in 1970s [60, 61] demonstrated its potential. The STEM operates in a very similar way to an SEM, deploying a very finely focused beam of electrons, formed by a

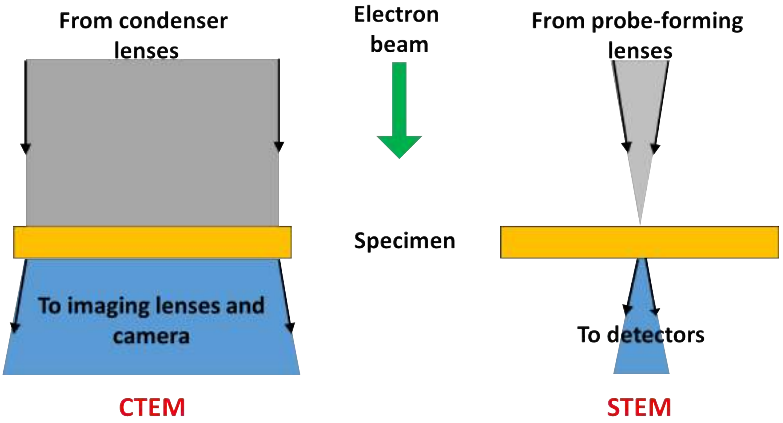

Figure 1.9 Schematic comparison between CTEM and STEM.

probe forming lens before the thin specimen. The beam scans across the sample in a raster pattern (see Figure 1.9, the scheme on the right). Interactions between the beam electrons and sample atoms generate a *serial* signal stream. For each probe position (x, y), the signal intensity , *I(x, y)*, and/or spectrum is recorded. Then the image(s) of *I(x, y)*, or else the integrated signal from the spectral data sets is displayed/recorded [62].

The main advantage of STEM over TEM is that with STEM, there is a better scope for collecting many more signals in a highly spatially-resolved way than we can with TEM. Some of these signals include: secondary electrons, scattered beam electrons, characteristic X-rays, and electron energy loss. Furthermore, we can record different signals in parallel, enabling an improved ultimate resolution and more easily interpretable atomic resolution images. Also, employing a technique called High-angle Annular Dark-field (HAADF) allows recording analytical information at single atom level. This technique is based on detection of electrons that have gone through elastic scattering at high angles. Fortunately, most modern TEM instruments include some sort of STEM capabilities as a standard part.

Lens Aberrations

The aberrations in the electron optics, present in both SEM & TEM, is due to the fact that the electrons are focused by several electrostatic and electromagnetic lenses. Thus, the image resolution is also limited by aberrations in these lenses. The main lens imperfections include: spherical aberration, chromatic aberration and astigmatism. Spherical aberration in the lens causes wave fronts from a point object to be spherically distorted by bending the rays at the outside of the lens more than those close to the axis. Chromatic aberration results in electrons with a range of energies being focused in different planes. Astigmatism occurs when a lens does not have perfect cylindrical symmetry. Among these imperfections, spherical aberration influences the TEM performance the most. These aberrations are illustrated diagrammatically in Figure 1.10. The theory of

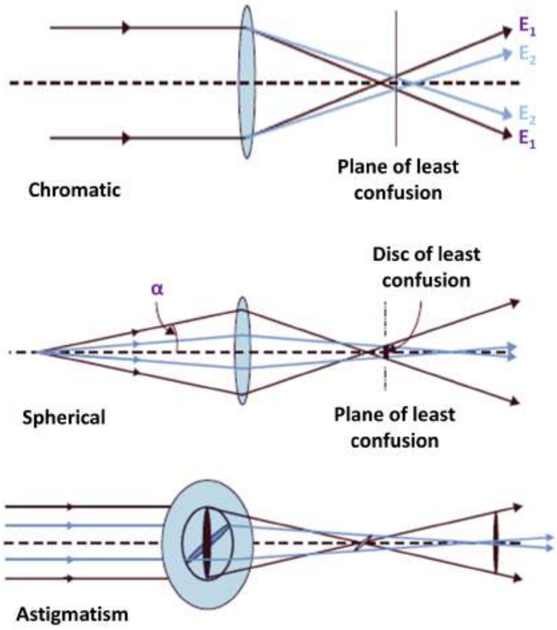

Figure 1.10 Schematic illustration of lens defects in a TEM (adapted from [63]).

aberrations in electron optics was proposed only a few years after the invention of TEM by Ruska. Nonetheless, the main barrier ahead of developing correctors, was the lack of engineering knowledge needed to build such correctors. It took some 65 years after the invention of TEM, to realise a spherical aberration corrector with which the resolution of TEM could be improved [64]. About 5 years later, the first commercially available systems for high-resolution TEM came on the market [65]. These advancements have introduced an exciting new area of 21^{st} Century analytical science; which can now allow true imaging and chemical analysis at the scale of single atoms [66]. Up to now, tens of corrected TEM machines have been installed worldwide, and hardware aberration correction has become an almost routinely used technique.

1.4.3 TEM on Graphene

Understanding of graphene has enjoyed an exponential increase since its discovery and electron microscopy has been a key element in this phenomenon. But the advances in the physics of graphene that have been achieved by electron microscopic studies, should be set in the broader context of electron microscopic studies of sp^2 bonded nanocarbons as a special class of materials.

The discovery of C_{60} was first confirmed by mass spectroscopy rather than TEM. This was due to the fact that TEM was not sufficiently advanced at the time. Moreover, this new form of carbon C_{60} had a closed cage structure and it constituent atoms were conveniently, all of the same mass, making it particularly suitable for mass spectroscopy [1]. Since CNTs may possess a variety of lengths and diameters, mass spectroscopy was not suitable to confirming their presence. It was HRTEM however, that could first confirm CNTs and provide clear image evidence of their existence [2].

It was however, the experimental isolation of graphene [3], and subsequently, the preparation of free-standing graphene membranes [6, 67], that paved the way to a whole range of new possibilities to study the sp^2 bonded carbon in the most direct way. Beneficially, the projected image of a monolayer membrane can be easily interpreted in terms of individual atomic positions (rather than atomic columns), allowing study of the fundamental properties of sp^2 bonded carbon atoms. Hence, the graphene membrane and investigation of its quality, are of particular interest for the science and applications of this promising new material. The power of direct images becomes more apparent in revealing the atomic configurations of lattice imperfections, such as point defects, grain boundaries, functional groups or edges. Sub-nanometre imaging of this sort has only become possible in recent years, and is still beset with a range of difficulties including preparation of clean large-area TEM samples. Prior to availability of low-voltage HRTEM, structural characterisation of graphene was primarily carried out using Raman, Atomic Force Microscopy (AFM) and optical microscopy (typically graphene was transferred onto SiO_2/Si wafers for these analyses [68–71]). However, in order to investigate graphene's atomic structure, HRTEM is invaluable.

The optics of TEM can be used to make images of the electron intensity emerging from the sample. For example, variations in the intensity of electron diffraction across a thin specimen, called *diffraction contrast*, is useful for making images of defects such as dislocations, interfaces, and second phase particles. Beyond diffraction contrast microscopy, which measures the intensity of diffracted waves, is HRTEM in which the phase of the diffracted electron wave is preserved and interferes constructively or destructively with the phase of the transmitted wave. This technique of *phase-contrast imaging* is used to form images of columns of atoms.

Understanding the TEM images and EDP of graphene, CNTs and related materials is relatively simple. With a thickness of only one or a few carbon atoms, the interaction between the beam and the sample can be approximated as a weak perturbation in the phase of the electron wave given by the electrostatic potential of the sample.

1.4.3.1 Electron Diffraction

Diffraction is an interference effect which leads to the scattering of high energy beams of radiation in specific directions. Diffraction from crystals is described by the Bragg's Law:

$$n\lambda = 2d\sin\theta \tag{1.10}$$

where n is an integer (the order of scattering), λ is the wavelength of the radiation, d is the spacing between the scattering entities (e.g. planes of atoms in the crystal) and θ is the angle of scattering.

When a beam of high energy electrons is used as the radiation source, the technique is called *Electron Diffractometry (ED)* and the resulting regular array of bright spots created by this interaction is termed *Electron Diffraction Pattern (EDP)*. ED refers to a collective scattering phenomenon with electrons being (nearly elastically) scattered by periodic arrays of atoms as found in a crystal. The incoming plane electron wave interacts with the atoms, generating secondary waves which interfere with each other. This occurs either constructively (reinforcement at certain scattering angles generating diffracted beams), or destructively (vanishing of beams). Similar to X-Ray Diffraction (XRD), these scattering events at crystal lattice planes can be described by equation 1.10. In this interaction, the atoms of the crystal act as a filter for the incident electrons, causing them to scatter in certain angles predicted by Bragg's Law. Each set of parallel lattice planes, generates a pair of spots in the EDP with the direct beam in their center. Since the wavelength λ of the electrons is known, interplanar distances can then be calculated from EDPs. Moreover, it is possible to deduce the symmetry of the crystal using ED-based analysis. These potential applications, make electron crystallography a powerful technique for "solving" crystal structures, both in physical and life sciences [72, 73].

EDP studies are usually performed with high energy electrons in a TEM instrument. ED has some specific features which offer a number of advantages over other diffraction techniques such X-ray diffraction [57, 59, 74] (a) The extent of sampling is much larger using electrons than by X-ray. Therefore, the EDP contains several spots when compared to other techniques, providing more reflections for crystallographic analysis. (b) Electron optics in TEM are able to vary the geometry of the EDP by focusing and changing the camera length. This enables acquiring ED from very small crystals in the sample. This is carried out by using the *parallel* beam in standard TEM mode and inserting an aperture in the image plane of the objective lens, confining the diffraction pattern to a selected area of the specimen. Thus, this technique is called Selected Area Electron Diffraction (SAED). The SAED pattern that appears on the viewing screen originates from the area selected in the image mode. SAED can be performed on the regions in the order of <0.5 µm diameter, but spherical aberration of the objective lens limits the technique to regions not much smaller than this. Providentially, it is possible to focus the electron beam to a small diameter and perform ED work at nanometre range. This method is termed Convergent Beam Electron Diffraction (CBED). *(c)* Since ED studies are typically performed in a TEM, the imaging capability of the microscope can be employed while the EDP is recorded. This is particularly important in the field of low-dimensional materials science when only very small features within a sample are of interest. One can calculate the interplanar spacing in the crystal being studied using the separation of spots in the DP. For this purpose, we need to first revisit the Bragg's equation. Since the ED angles are very small ($0° < \theta < 2°$), therefore we have:

$$\sin(\theta) \approx \tan(\theta) \approx \frac{1}{2}\tan(2\theta) \tag{1.11}$$

We can depict the geometry of electron diffraction as shown in Figure 1.11:

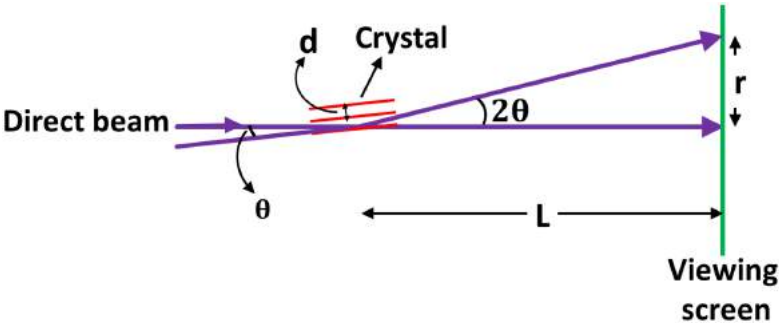

Figure 1.11 Schematic illustration of geometry of electron diffraction and the concept of camera length L.

From the geometry of Figure 1.11 we can write:

$$\tan(2\theta) = \frac{r}{L} \tag{1.12}$$

which we can then substitute this into equations (1.10) and (1.11) to obtain:

$$rd = \lambda L \tag{1.13}$$

where r is the distance from the central spot, d is interplanar spacing and the product λL is called *camera constant*, whose unit is usually Å.cm and can be found in the manual of any TEM instrument.

Electron Diffraction Study of Graphene

ED is a reliable and relatively straightforward way to assign the number of layers in graphene; but one might ask when we are to analyse a single atomic layer material such as graphene, how diffraction could occur? For any diffraction condition the Bragg's law should be satisfied which contains the parameter d, the inter-planar spacing, whereas graphene is only one layer. The answer lies in the fact that in case of a 2D crystal, the reciprocal lattice is formed by rods (see Figure 1.12 (a)) instead of discrete points as in case of a 3D crystal. In other words, the condition that the scattering wavevector has to intersect the reciprocal lattice, only applies to the components parallel to the lattice which means in the graphene plane in our case.

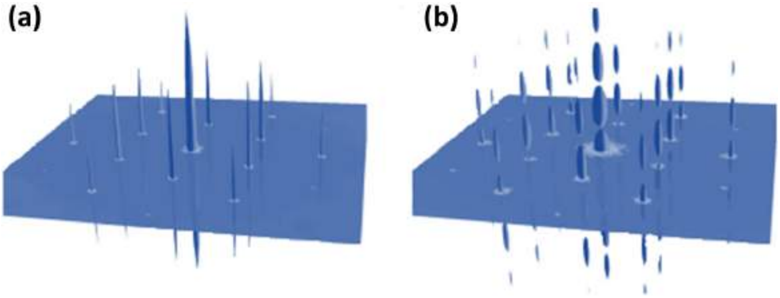

Figure 1.12 Schematic representation of reciprocal space of (a) Monolayer and (b) Multilayer graphene.

As can be seen in Figure 1.12 (b), the rods are discontinuous due to the additional layers on top of perfect 2D monolayer graphene. To label equivalent Bragg reflections, Miller-Bravais indices [hkil] for graphite is used so that the innermost hexagon of diffraction spots corresponds to $[1\bar{1}00]$ and the next one to $[11\bar{2}0]$ indices. Figure 1.13 depicts the above-mentioned directions and planes in the graphite lattice.

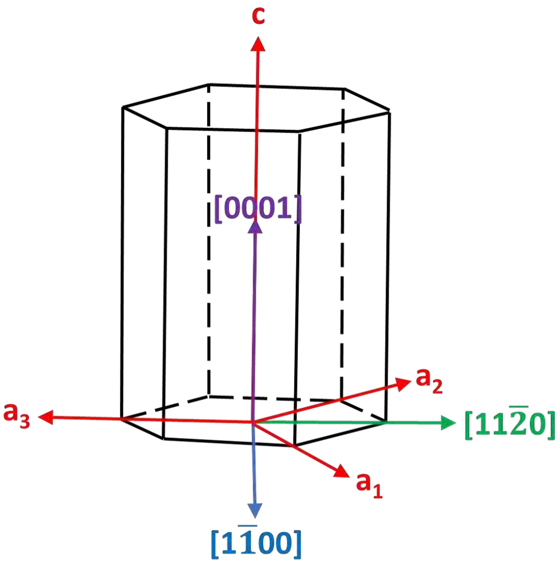

Figure 1.13 Crystal directions analysed in diffraction pattern study of graphene and graphene layers.

The intensity ratio of diffraction spots from $[11\bar{2}0]$ to those from $[1\bar{1}00]$, varies with the number of layers in graphene [75]. When there is only one layer, the $I_{[11\bar{2}0]}/I_{[1\bar{1}00]}$

is nearly equal to one (see Figure 1.14 (a) & (c)). For an AB-stacked bilayer sample, Figure 1.14 (b) & (d), the $[11\bar{2}0]$ intensity is ≈ 4× higher than the $[1\bar{1}00]$ intensity. in general, for crystalline Bernal- or ABC-stacked multilayer samples the $[11\bar{2}0]$ intensity is stronger than the $[1\bar{1}00]$ intensity.

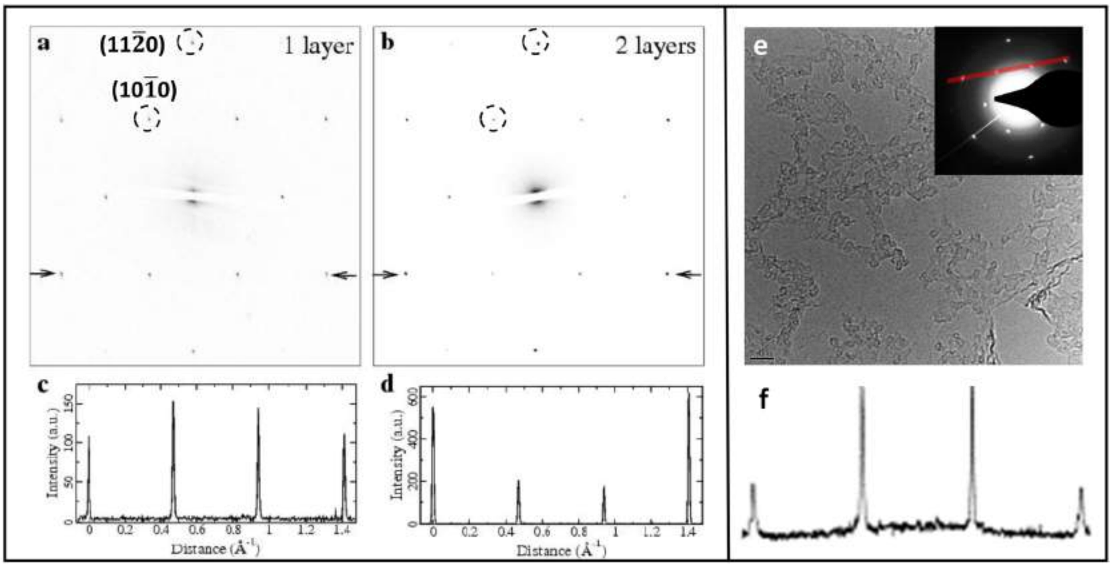

Figure 1.14 (a) EDP of a monolayer graphene membrane, and (b) a bilayer membrane. A profile plot along the line between the arrows is shown in (c,d) (adapted from [75]).(e) TEM image of a CVD graphene suspended on a TEM grid. The inset is the corresponding DP. (f) The intensity profile along the red line in DP.

The EDPs can also provide a first indication of defect density. The mean deviation from a regular lattice, reduces the intensities of the higher order reflections [76]. Therefore, potentially a highly- defective few-layer graphene sheet, where the $[11\bar{2}0]$ intensity would be reduced, might be mistakenly identified as a monolayer. Furthermore, as mentioned above, an AA stacked multilayer graphene would produce the same pattern as monolayer graphene (however, reports of AA-stacked graphite are quite rare). For an unambiguous identification of monolayer graphene from electron diffraction data, one needs to obtain a series of diffraction patterns with the sample tilted to different orientations; or use other supplementary techniques such as Raman spectroscopy.

1.4.3.2 Imaging and Interpretation

When an image is formed in TEM, it is either by using the central spot (see Figure 1.15 (a)), or some or all of the scattered electrons (see Figure 1.15 (b)). The way that the user chooses which electrons form the image, is implemented by insertion of an aperture into the back focal plane of the objective lens, to block out selectively part of the diffracted electrons. In other words, by means of special mechanism inside the TEM, the user can drive the desired aperture so that either the direct electrons or some scattered electrons go through it. If the direct beam is selected, the resulting image is called a bright-field (BF) image (Figure 1.15 (b)); and if the scattered electrons of any form is selected, it is called a dark-field (DF) image (Figure 1.15 (b)). For each imaging mode shown in Figure 1.15, an actual TEM image is depicted at the bottom of the diagram, for further clarity. The most notable difference between these two mode is that the image contrast is inverted in relation to one another. This is due to the mechanism of image formation in each case. Since BF images are formed by weakening of direct beam upon interaction with the sample, a mass-thickness contrast is in effect. Thus, the areas in the sample that contain heavier elements, appear darker. Whereas for an DF image, the diffracted beams are the main contributor to the image formation; thus DF images contain information about the crystal lattice such as imperfections and a more reliable composition contrast comparing to the BF image.

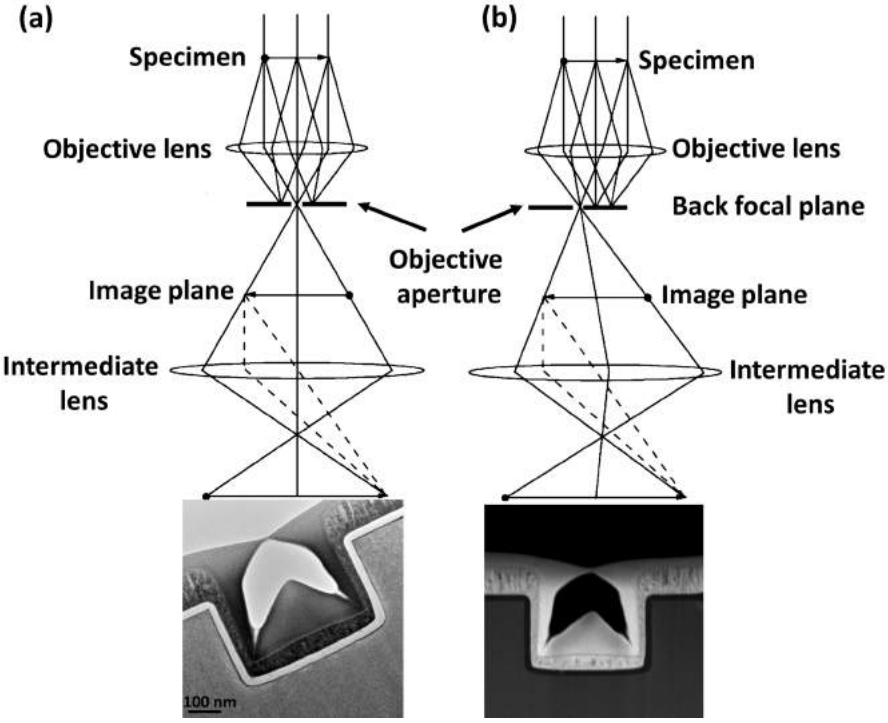

Figure 1.15 Schematic illustration of (a) Bright Field (BF) imaging mode. (b) Dark Field (DF) imaging mode. The diagram is adapted from [74], images are owned.

1.4.3.3 Feature Types on Graphene

Despite all the remarkable capabilities of TEM as a characterisation tool, offering atomic-scale resolving power, perhaps its most notable disadvantage is the need for an electron transparent specimen, so that the electrons may be transmitted through to the detectors. This normally necessitates extensive sample preparation, with etching and milling procedures to thin the sample sufficiently to be imaged. However, graphene's inherent atomic thickness negates many of the conventional sample preparation issues, and thus is a perfect specimen for study by low-voltage AC-TEM, allowing the probing of atomic scale defects in the graphene structure at high spatial and temporal resolution. Below, some of the most important TEM feature types of graphene are presented.

Graphene lattice at atomic resolution

HRTEM images are formed by interference of diffracted and transmitted electron beam with the sample and the modulation of the phase of electron wavefunction after the sample. Thus, HRTEM images are inherently more difficult to interpret compared to the traditional optical and electron microscopy techniques where the change in the amplitude of the incident beam wavefunction is used for image formation. Therefore, the HRTEM image obtained on the detector is not necessarily a direct image of the atomic positions [57].

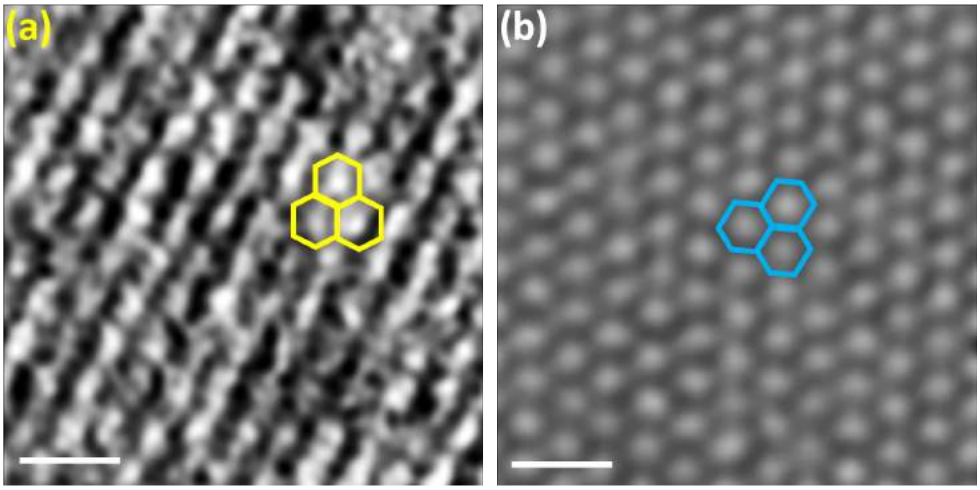

Figure 1.16 HRTEM images of graphene honeycomb lattice. (a) Image taken by a non-AC TEM machine. (b) Image recorded in a AC-TEM machine. The overlaid hexagons are guides to the eye. The scale bars are 0.5 nm.

There are two factors that should be taken into account when HRTEM analysis is performed, the modification of the incoming electron wave by the sample, and a further modification of the exit wave after the sample by the electron optics of the microscope. Fortunately, the effect of the sample can be considered negligible for one-atom thick, light-element samples such as graphene. A consequence of this approximation is that, we can simply interpret regions of dark contrast as regions of high electron density, making image interpretation markedly more straightforward.

The effect of the microscope can be described by a complex function, which depends on the defocus and lens aberrations in the microscope, and spherical C_s in particular [77].

Hence, correcting for the lens aberrations is essential when precise HRTEM analysis of atomic positions is intended. This is the basis of the work presented in Chapter 6. Perhaps the most familiar and simplest TEM feature of graphene is HRTEM image of honeycomb lattice of graphene. Figure 1.16 shows a non AC-TEM image together with a HRTEM taken by AC-TEM for the comparison. While one can clearly distinguish the hexagonal network of graphene lattice in the right-hand side image, the one at the left only contains a hint of graphene lattice.

Defects in Graphene

In a defect-free graphene lattice, each carbon atom is bonded to three neighbouring carbon atoms, with identical 120° in-plane bonding angles. The presence of structural defects breaks this perfect symmetry and opens a whole research area for studying the effect of structural defects on the mechanical, electrical, chemical, and optical properties of graphene. Nonetheless, sometimes their effect is beneficial. For instance, defects are essential in chemical and electrochemical studies, where they create preferential bonding sites for attachment of desired functionalities [78, 79]. On the other hand, defects pose a problem for electronics applications such as field-effect transistors because they can significantly lower the charge carrier mobility and thus increase the resistivity of graphene sheet [80, 81]. Given their crucial impact on graphene properties, it is important to control defect formation and, if possible, find ways to repair existing defects. The superior resolving power of modern AC-TEM systems permits the imaging of atomic defects in the graphene lattice.

As a two-dimensional crystal, one can identify three main types of defects in the graphene lattice: point defects (e.g. vacancies and Stone-Wales (SW) rotation, adatoms, substitutions and interstitials), line defects (e.g. dislocations and grain boundaries) and edge imperfections. In the second type of defect, one carbon atom is replaced by another atom of a different element or, an adatom is incorporated into the lattice without replacing any carbon atom. Below, these defects are discussed except for line defects. However, grain boundaries in graphene is discussed as one of the most important TEM studies of graphene.

Point Defects

Stone-Wales Defect

The regular graphene hexagonal lattice may be disrupted by an in-plane 90° rotation of a bond, yielding a transformation of four adjacent 6-membered carbon rings to two 5-

and two 7-membered rings, as illustrated in Figure 1.17 (a, b) [82]. This defects requires 9-10 eV energy to be created which means further creation of such defects is very unlikely at room temperature (T=298 K therefore kT=0.0257 ev). However, under the effect of electron beam irradiation inside the TEM, this energy can be supplied. For instance, at 80 kV TEM analysis, a kinetic energy of ≈ 80 eV is imparted to the specimen which is sufficient to create a SW rotation.

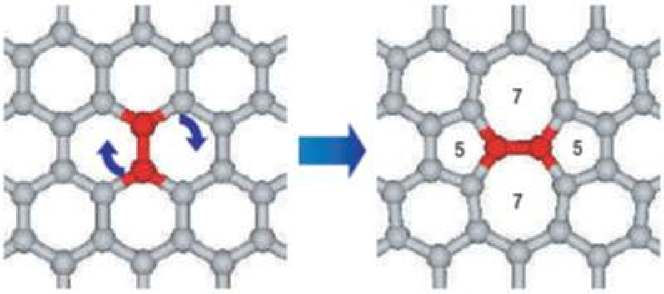

Figure 1.17 Schematic model of Stone-Wales defect (adapted from [83]).

Vacancies

In a vacancy defect, one or more atoms are removed from the lattice and the resulting perturbation to the lattice is relaxed by one or more SW rotations. Vacancy defects in graphene are not easily formed. The energy required to sputter a single atom out of the lattice is in the range of 10-22 eV [84], depending on the type of vacancy. Such energy can not be achieved unless the lattice is irradiated with high energy ions or by electrons in a TEM environment (>80 kV for graphene). These kinds of defects act as strong scattering centres for the charge carriers in graphene [85]. Vacancies can also act as occupancy sites for substitutional impurities, and can also exhibit complex structures when combined with multiple SW bond rotations defects.

Monovacancy

The ejection of a single carbon from the graphene lattice yields a monovacancy (see Figure 1.18 (a)), which leaves the graphene lattice with three under-coordinated edge carbon atoms (Figure 1.18 (b)), each of which possesses a single dangling bond. To minimise the energy the defect can undergo a geometric distortion, with a bond reconstruction between two of the under-coordinated carbon atoms, resulting in a 5-membered and a 9-membered ring (Figure 1.18 (c)). This structure is rather unstable as it contains under-coordinated carbon atoms. Thus, its observation in TEM is infrequent [84].

Divacancy

These vacancies form upon ejection of two carbon atoms from graphene rind and subsequent reconstruction of the perturbed rings. These vacancies are more stable under

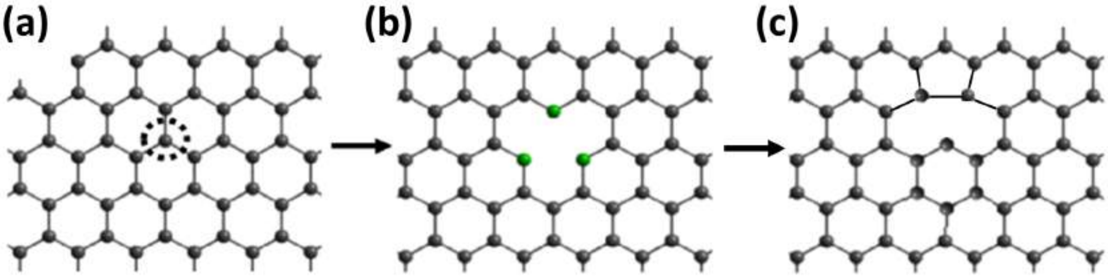

Figure 1.18 Schematic model of monovacancy point defect (reproduced from [86]).

electron exposure as all the carbon atoms involved are sp^2 bonded [87, 88]. The most

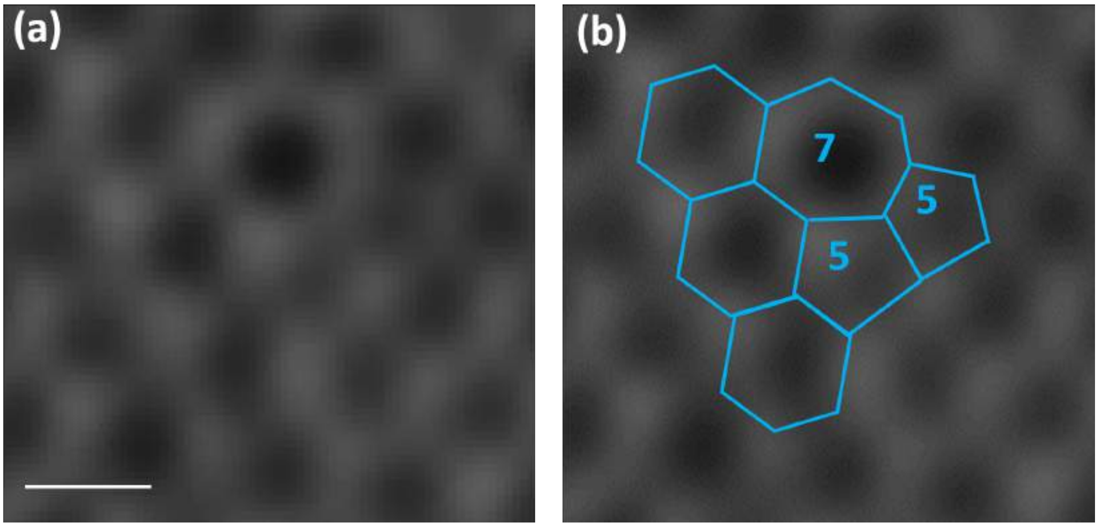

Figure 1.19 (a) Smoothed AC-TEM image of a reconstructed divacancy in graphene. (b) The annotated version of the (a). The numbers denote the the number of carbon atoms in the ring. Scale bar is 0.25 nm.

basic transient configuration is 5-8-8 ring patter. This structure is fairly unstable and under the effect of electron beam in TEM, can transform to other ring patterns [87, 88]. For instance, structures such as 555-777, 5555-6-7777 have been reported (the numbers denote the carbon count in a ring) [84]. Other ring patterns may also form by a SW rotation of a bond in the produced structure. Figure 1.19 shows an example of such reconstructed divacancy in graphene lattice.

Multivacancies

Higher number of vacancies are also probable in the graphene lattice to be formed. However, they require highly-focused beam bombardment and/or prolonged exposure to the beam. Figure 1.20 shows a schematic model of possible multivacancies in graphene lattice.

Adatoms and Impurities

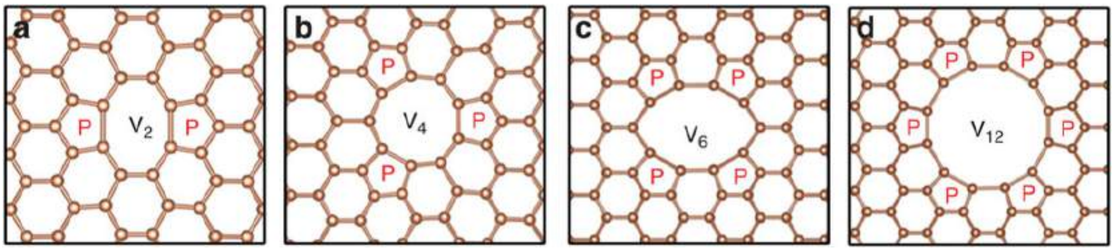

Figure 1.20 (a–d) The relaxed atomic models of multivacancies in graphene (double, tetra, hexa and dodeca, respectively). ‘P’ indicates the five-atom rings and V_n denotes the number of vacancies (adapted from [89]).

Introduction of dopants and foreign atoms into the graphene lattice is necessary for many applications such as functionalisation, sensing and bandgap engineering. Adatoms typically occupy one of three high symmetry sites on the graphene lattice known as bridge (B), hollow (H) and top (T) sites [90]. These sites are shown schematically in Figure 1.21. Figure 1.21 (b) shows a filtered AC-TEM image of a graphene edge, containing many larger foreign atoms (marked by yellow dashed circles and arrows). Given the size of these atoms, it is postulated that they have incorporated in H positions. However, precise assignment of the incorporation site, requires further localised compositional data.

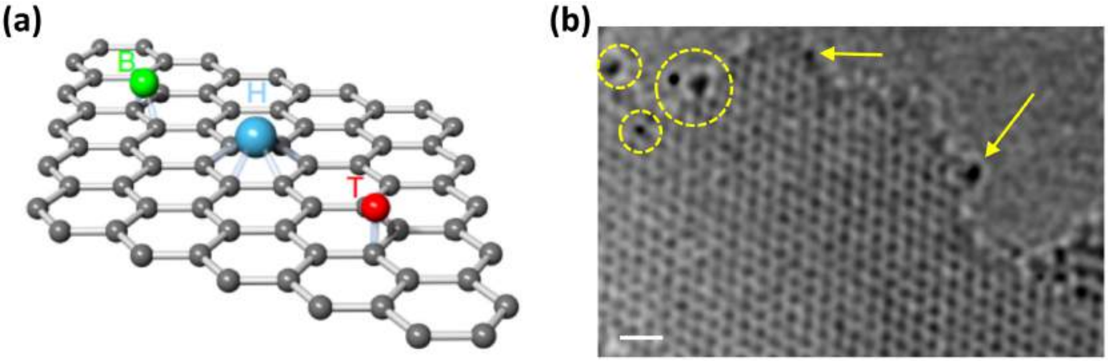

Figure 1.21 Adatoms in graphene. (a) Depending on the element, adatoms favour either the high-symmetry bridge (B), hollow (H), or top (T) position in the graphene sheet (adapted from [91]). (b) Filtered AC-TEM image of a graphene edge, containing a number of large foreign atoms. Scale bar is 0.5 nm.

Alternatively, adatoms may incorporate themselves directly into the graphene structure by a direct replacement with a carbon atom in a substitution. Interstitials in graphene are limited to multilayer graphene, where the foreign atom lies in between crystal planes. This is due to the fact that, it is impossible for the monolayer graphene to accommodate for otherwise [90].

Edges

A great deal of interest has been vested in the study of graphene edges, in particular their effect on graphene nanoribbons; structures that exhibit modified electronic properties to that of bulk graphene [92, 93]. The edges of graphene can terminate in four main ways, namely zigzag, armchair, reconstructed edges and Klein edges and their variations [94, 95]. Figure 1.22 shows smoothed and inverted AC-TEM images of the zigzag, armchair, reconstructed zigzag structure and Klein edges and corresponding annotated images for more clarity. The armchair and zigzag configurations result from terminating

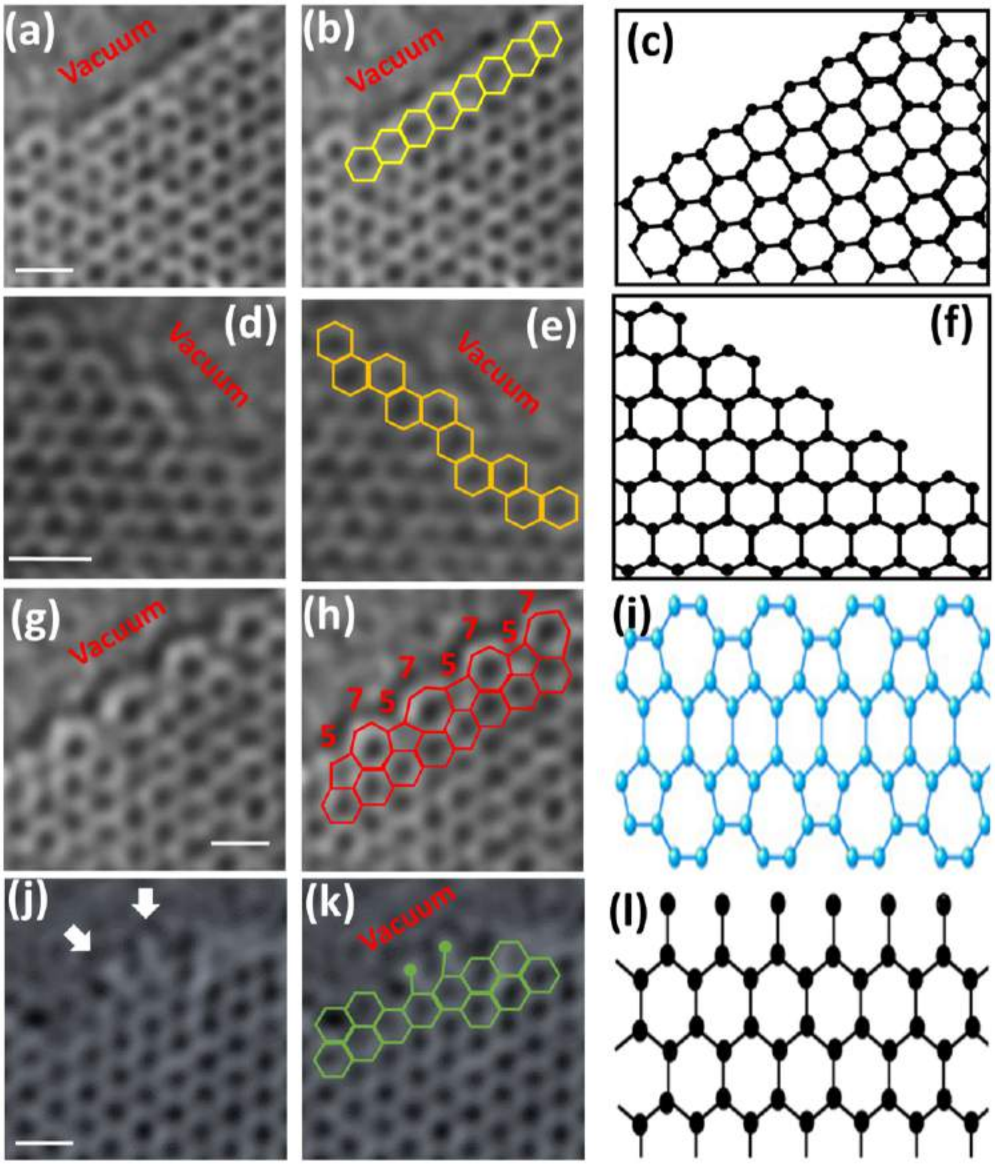

Figure 1.22 Four edge structures in graphene: (a-c) zigzag (d-e) armchair (g-i) reconstructed zigzag edge and (j-l) Klein edge. In each case a filtered AC-TEM, its corresponding annotated image and a schematic model shown. The numbers in (h) denote the carbon count in the edge rings. White arrows in (j), mark the position of two dangling Klein edges.

graphene along the lattice line without any reconstruction [92]. AC-TEM imaging and supporting calculations [96, 97], have demonstrated that the formation of a reconstructed zigzag state is of lower energy than the metastable zigzag configuration. It is possible to capture the formation of dangling, single bonded carbon atoms projecting from the graphene zigzag edge; these are known as Klein edges [98] and two of them are show in Figure 1.22 (d) (white arrows). The relative stability of these edges, as well as various observed Klein edges, are elaborated in Chapter 5.

Identifying the number of layers

As mentioned previously in this Chapter, There are several non-destructive techniques for determining the layer count of a graphene sample, some of which do not require the high resolution of an AC-TEM and yet sensitive enough (e.g. Raman spectroscopy). Nonetheless, by employing focussed electron beam sputtering of the graphene sheet at a high current density (80 kV) it is possible to open up holes in the graphene sheet. Figure 1.23 shows a bilayer graphene example, with the region irradiated until vacuum was visible. The number of layers are colour coded for more clarity.

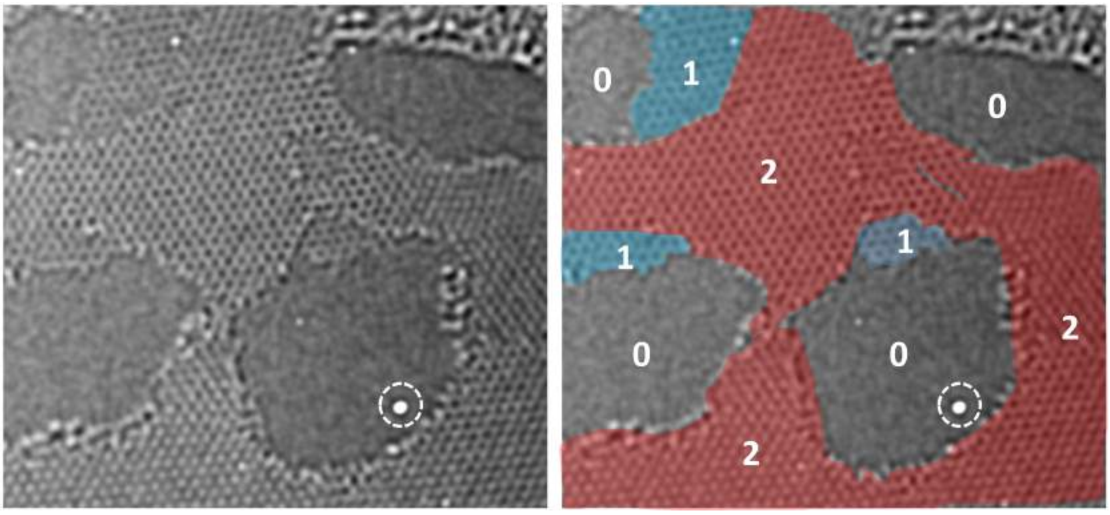

Figure 1.23 Identification of layer count in a bilayer graphene sheet. The numbers denote the layers count in different parts of the image. The white spot encircled with dashed white is a debris on CCD camera of the microscope.

The rest of this section, outlines some of the two of the most important examples of advances made possible via TEM studies; but does not necessarily review all studies in the field or deal with them in a chronological order.

Ripples in Graphene

First and foremost, the presence of ripples in graphene sheets which accounts for the stability of two-dimensional graphene, was first confirmed via electron diffraction (ED) studies carried out using TEM [99]. This complementary technique, is generally the most accurate approach for studying ordered (crystalline) configurations and, to some extent, the spatially averaged deviations from the regular lattice. The clue that led to the realisation of ripples of suspended graphene was broadening of the diffraction spots, caused by tilting of surface normals, caused by tendency of carbon atoms to form the more stable *sp*3 structure (see Figure 1.24).

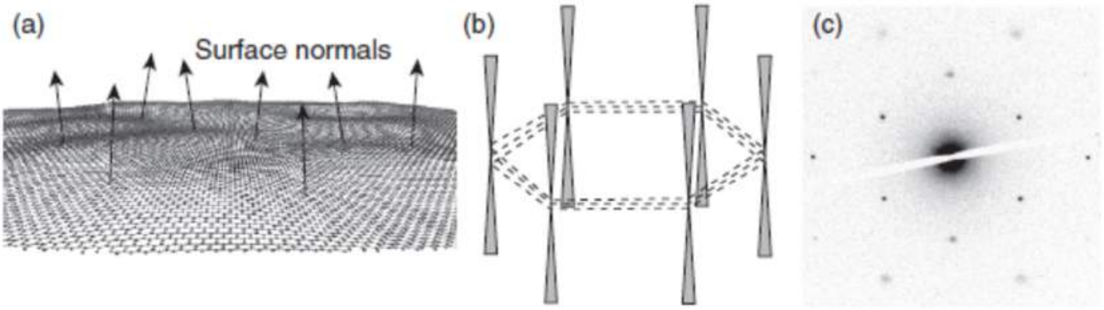

Figure 1.24 The corrugation of suspended graphene sheets. (b) The variation in surface normals leads to non-zero intensities on cones instead of rods in reciprocal space. (c) As a result, ED patterns obtained with a tilted sample (here 15° with horizontal tilt axis) show a broadening of the diffraction spots (adapted from [6]).

Grain Boundaries

The next example is observation of the grain boundaries in CVD-grown graphene using TEM. The CVD synthesis of graphene on transition metal surfaces (e.g. nickel and copper), yields large-area graphene sheets. Nevertheless, the graphene sheets produced by this method are polycrystalline with grain boundaries between domains of different orientation [24, 38, 42]. Grain boundaries in general, had been predicted to contain non-hexagonal configurations as a periodic array of dislocations [100, 101] although the precise arrangement was not clear. The resulting grain boundaries between monolayer graphene areas were imaged for the first time by Huang *et al.* [102] and Kim *et al.* [103]. Figure 1.25 shows an annular dark field (ADF)-STEM image (atoms appear white) of a grain boundary in a large-area polycrystalline graphene sheet synthesized on copper and subsequently transferred to a microstructured TEM grid [102]. In Figure 1.25 (c)–(d), one can clearly see the grain boundary structure: carbon pentagons and heptagons are found at the grain boundary, oriented in such a way that all carbon atoms are in a sp^2 configuration. To study the grain boundaries in graphene, a combination of high-resolution and dark-field imaging where the former offers precise assignment of atomic configurations on a nanometre scale and the latter is sensitive to crystal orientations on a micrometre scale.

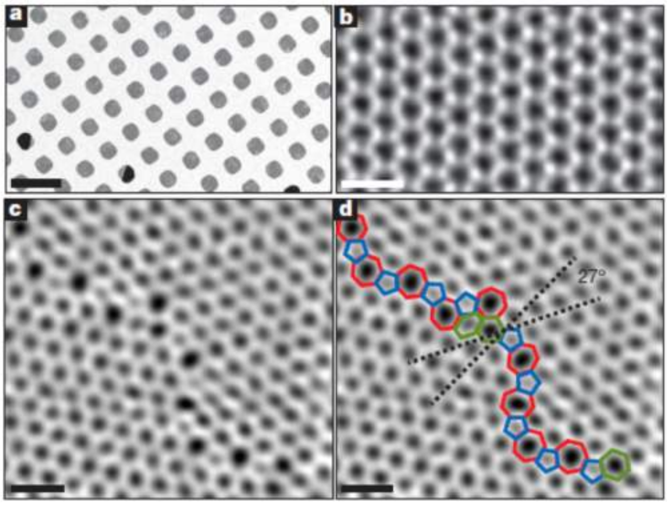

Figure 1.25 Annular dark field STEM images of graphene and grain boundaries in graphene (a) low-magnification image of CVD graphene membranes on a support grid. (b) High-resolution image of the graphene lattice. (c) Image of a representative grain boundary, and (d) the same image with pentagons, heptagons, and a few hexagons outlined. Scale bars are (a) $5\,\mu\mathrm{m}$, (b)–(d) $5\,\text{Å}$ (adapted from [102]).

1.5 Electron Energy Loss Spectroscopy

As previously mentioned, in TEM, incident electrons interact with the specimen atoms in three possible ways: elastic scattering, transmission through the specimen or inelastic scattering. Upon the first two types of interactions, the energy of incident electrons remains more or less unchanged; whereas in the latter case, the electrons lose some of their energy during this interaction. The energy loss of such electrons is directly related to the specimen atoms and the electron shells from which the inelastic scattering has occurred. The amount of the energy loss can be measured by means of a spectrometer, located in or after the TEM column, and be displayed as a plot. This plot shows a count of how many electrons have lost what extent of energy and is termed Electron Energy Loss Spectrum (EELS); the y-axis in an EEL spectrum corresponds to the number of electrons or count and the x-axis represents the energy loss. The probability of the scattering events is proportional to $\frac{\sqrt{Z}}{V}$; where Z is the atomic number and V is accelerating voltage of the incident electron beam and $\frac{\lambda_\mathrm{e}}{\lambda_\mathrm{i}} \sim \frac{10}{Z}$; where λ_e and λ_i are the mean free path for elastic and inelastic scatterings, respectively.

1.5.1 Specimen Thickness

There are many types of inelastic processes including single scattering and plural scattering. The specimen thickness, which is of great importance in analytical TEM, influences the probability of these scattering events. These two types of scattering are shown schematically in Figure 1.26.

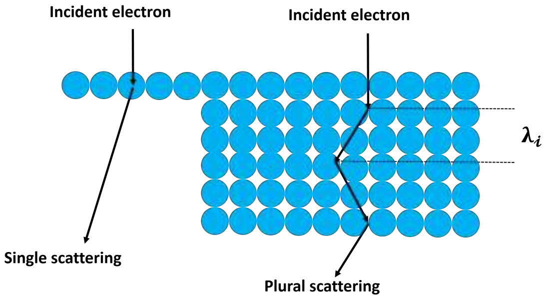

Figure 1.26 Schematic illustration of single and plural scattering and the mean free path of inelastic scattering equation.

The plural scattering is detrimental to the edge visibility as it increases the background noise. The probability for n times scattering is described mathematically by Poisson distribution:

$$P_n = (\frac{t}{\lambda_i})^n . \exp(\frac{-t}{\lambda_i})/n! \tag{1.14}$$

Where t is specimen thickness. In order to get reliable results from EELS, the sample thickness should be less than mean free path value which is normally satisfied by a maximum 50 nm-thick sample.

1.5.2 Feature Types

Three main regions can be identified in a typical EEL spectrum: zero-loss, low-loss region and high-loss region (see Figure 1.27) ; Each of these features has its own origin and carries specific information. The characteristics and relevant analytical applications of each of these regions are outlined below.

Zero-loss Peak. Most electrons on their way through the specimen will not experience inelastic scattering hence will lose no energy (except for small losses due to phonon scattering). These electrons, therefore, contribute the most to the spectrum and generate a peak in the spectrum called Zero-Loss Peak (ZLP); which is the prominent and the most intense feature observed in thin samples. The width of the zero-loss peak is indicative of the energy spread of the electron source and becomes broader as the energy resolution

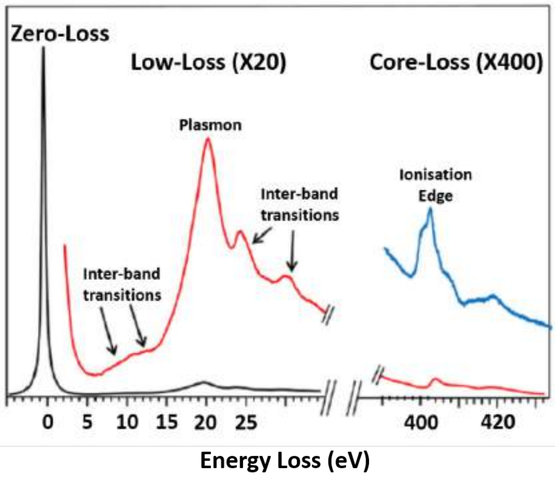

Figure 1.27 A typical EEL spectrum (adapted from [104]).

decreases. The ZLP is not that informative and may even cause damage to the CCD camera if enough care is not taken during acquisition of the spectrum simply because it is very intense.

Low-Loss Region. This regions normally expands to about 50 eV energy loss and originates from the interaction of the beam with the weakly-bound outer shell electrons in the sample. This interaction causes longitudinal wavelike oscillations of (quasi)free electrons in the valence or conduction band and generates a characteristic loss termed *Plasmon Loss*. Energy loss due to plasmon excitation ($\mathcal{E}_{\mathcal{P}}$) depends on the local density of free electrons (n) which is affected by the sample chemistry; therefore plasmons can be used for microanalysis. The lifetime of plasmons is too short (about 10^{-15}s) and they decay either in the form of photons or phonons. Plasmons are localised to <10 nm, carry contrast information and can limit image resolution by chromatic aberration. The low-loss part of spectrum can also be used to accurately measure the relative thickness (t/λ) of the thin films:

$$t = \lambda \ln(\frac{I_{tot}}{I_0}) \tag{1.15}$$

Where I_0 is the intensity of zero-loss peak and $\mathrm{I_{tot}} = \mathrm{I_0} + \mathrm{I_{inelast}}$. Absolute thickness value can be determined by some mathematical treatment such as Kramers-Kronig sum rule [105]. Low-loss region also contains energy losses related to *Inter- or intra-band Transitions* which are generated by excitation of core electrons to the orbitals of higher quantum number. These losses appear on the rise of the plasmon peak and can be used for fingerprinting identification of chemical changes in the specimen. However, a reference spectrum is a must for interpretation of the results and the process is not very well-understood. Some other advanced applications of low-loss EELS include: band gap measurements using monochromated electron source [106–108], chemical analysis and probing the optical properties [109].

High-Loss Region. This region includes energy losses >50 eV and originates from interaction of electron beam with inner shell electrons leading to excitation to an unoccupied orbital above the Fermi level. This ionisation loss process results in generation of characteristic elemental energy loss edges (e.g. K, L and M) which is unique for each and every element. Typically the K-edge has a sharp onset whereas in other edges while the sub-shell transitions can be resolved individually, the energy dispersion of the edges are broader. These are high energy processes and there is a minimum threshold value, E_C, that must be transferred from the incident electron to the inner-shell electrons for them to be able to escape from their orbitals (this energy is the binding energy of the inner-shell electron to the nucleus of atom). At the same time, however, ionisation also occurs with larger energy losses $E>E_C$. The ionisation edge intensity is smaller than those of plasmons; and the closer a primary electron gets to the nucleus of an atom, the larger the energy loss becomes.

Energy-Loss Near Edge Structure (ELNES)

Features whose energy loss lie between $\mathrm{E_C} < \mathrm{E} < \mathrm{E_C}$+50 eV are called Energy Loss Near Edge Structures (ELNES) and essentially reflect the density of unoccupied states [110]. Some of the applications of ELNES are as follows: (a) Identification of transition metals. If the d shell is empty, $\mathrm{L_2}$ and $\mathrm{L_3}$ will split. By measuring the ratio of the L edges, the type of the transition metal can be identified. (b) Orientation. In anisotropic crystals, ELNES changes with the alignment of the momentum transfer along different crystallographic directions. (c) Chemical shifts. This effect is due to charge transfer in the valence band which eventually leads to a shift in the edge threshold. An example is distinguishing different oxidation states of titanium from the appearance of edges. (d) Fingerprinting information for differentiating specific phases. An example of the carbon K-edge ELNES of a number of carbon-based compounds and some carbon allotropes are shown in Figure 1.28. In this example, one can see the clear evolution of π^* an σ^* peaks. At the bottom, the spectrum of graphite, as a pure graphitic carbon, shows intense π^* peak together with the well-defined shoulders within σ^* peak. As we go upwards, the fraction of sp^2 bonds decreases, so does the intensity of π^* peak associated with it. Finally, the topmost spectrum from diamond, a pure sp^3-bonded carbon, shows no π^* peak at all. In the case of nitrogen-containing samples, one can distinguish the emergence of the nitrogen K-edge at $\approx$ 401 eV. Performed in STEM mode in a standard microscope, a probe size of $\leq$ 0.9 nm can be achieved, making this technique a suitable tool for characterisation of nanomaterials and, in particular, nanocarbons.

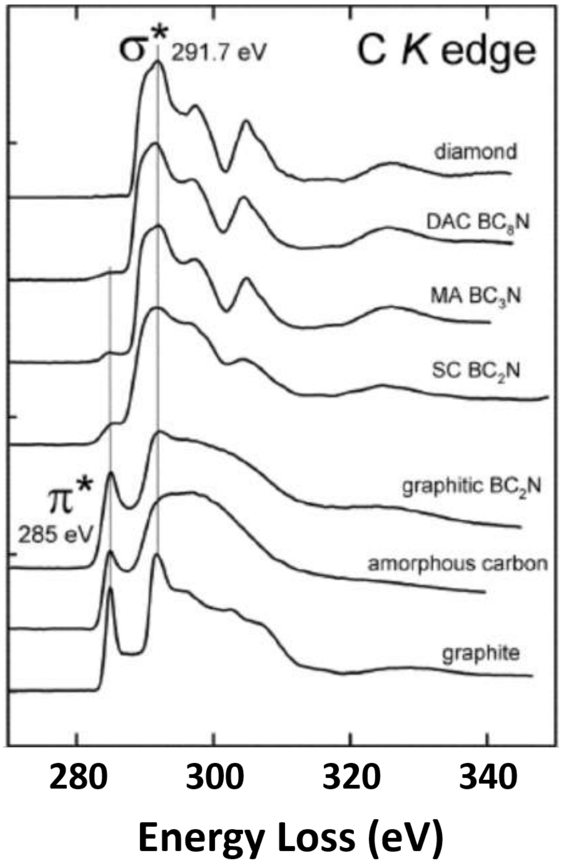

Figure 1.28 Carbon K-edge ELNES of different C-related compounds highlighting the fingerprinting ability of ELNES technique (adapted from [111]).

1.5.3 Graphene Spectrum

Graphene has low-loss and core-loss spectra as shown in Figure 1.29. When the thickness of a graphite specimen is reduced, the bulk plasmon (7 and 27 eV) peaks eventually become red-shifted, to about 5 and 14.5 eV in the case of a single graphene layer. These shifts are in substantial agreement with calculations made using local density functional code [114]. The out-of-plane mode approaches zero in single-layer graphene, whose π-plasmon exhibits a linear dispersion, from 5.1 eV at $q = 1\,\mathrm{nm}^{-1}$ to 6.7 eV at $q = 4\,\mathrm{nm}^{-1}$ [115]. Linear dispersion is also observed for bilayer graphene but is closer to quadratic for trilayers. Monolayer graphene can be distinguished from the fact that its EDP varies little with specimen orientation [116].

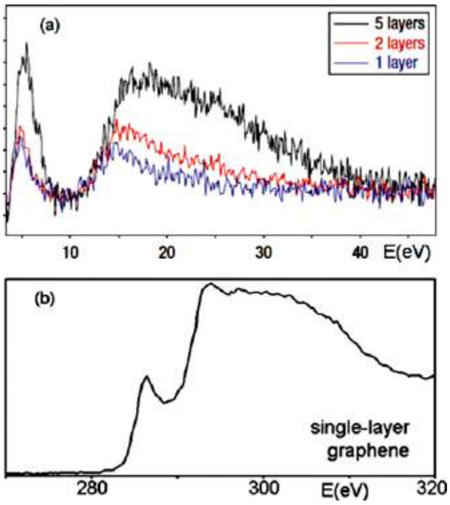

Figure 1.29 (a) Low-loss spectra of single-, double-, and five-layer suspended graphene, recorded using 100 keV electrons [112]. (b) Carbon K-edge recorded using 200-keV electrons from single-layer free-standing graphene. The K-edge of a double layer appeared similar [113].

1.6 Raman Spectroscopy

1.6.1 Raman Scattering Theory

Raman spectroscopy has become a versatile and powerful tool in the field of nanoscience and technology as it is a non-destructive technique with minimal or no sample preparation, it can be carried out at room temperature and ambient conditions, the operation of modern Raman systems is fairly straightforward and the measurements can be reasonably quick while lots of information can be extracted from the acquired spectra. Raman spectroscopy involves shining a sample with a monochromatic light source (typically a laser) and detecting the scattered light. Most of the incident light will interact elastically with the specimen so the scattered light will be at the same frequency as the incident light which is known as Rayleigh scattering. However, a small fraction of the light will be inelastically scattered at frequencies different from the incident photons. This shift in energy from the laser frequency is known as the Raman Effect. Plotting the intensity of this scattered light versus the energy difference between the incident laser and scattered light forms the Raman spectrum of the specimen. Since the vibrational energy levels are unique to each material, the Raman spectrum provides a fingerprint identification of the specimen being examined. Figure 1.30 schematically illustrates the energy transition involved in the Raman scattering process. In Figure 1.30 one can note two types of shifts: if the final vibrational state is more energetic than the initial state, the inelastically scattered photon will lose energy to accommodate the total energy balance of the system. This decrease in the frequency of the scattered photon (by creating a

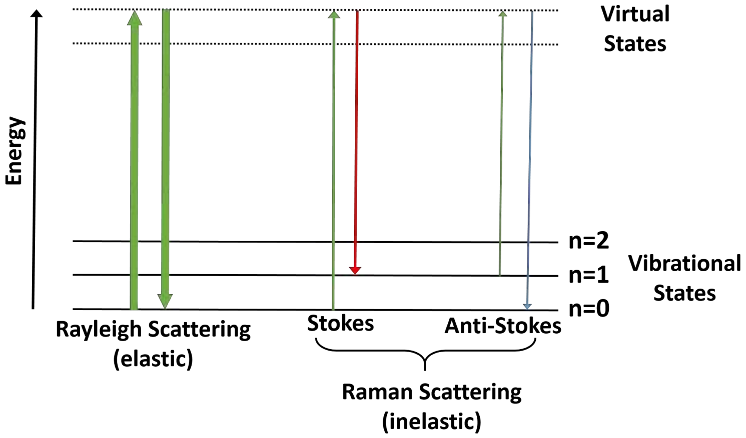

Figure 1.30 Energy diagram of elastic and inelastic scatterings. The thickness of the arrows represents the intensity of each type of scattering.

phonon excitation) is called *Stokes shift*. However, if the opposite process happens and the scattered photon gains energy during the process, this energy difference is termed *Anti-Stokes shift*; in other words the scattered photon shifts to a higher frequency than the incident light. This additional energy comes from dissipation of thermal phonons in the crystal, cooling it down during the process. If we express the energy and momentum of the incident photon with E_L and k_L respectively, those of scattered photon with E_{Sc} and k_{Sc}, and E_q and q for those of phonons, then for energy and momentum conservation we must have:

$$E_{\mathrm{Sc}} = E_{\mathrm{L}} \pm E_{\mathrm{q}} \qquad \text{and} \qquad k_{\mathrm{Sc}} = k_{\mathrm{L}} \pm q \tag{1.16}$$

In the Stokes process, a phonon is created thus the (+) sign in the equations 1.16, whereas in anti-Stokes a phonon is annihilated so the (-) sign. The $\pm E_{\mathrm{q}}$ are in fact the Raman peaks that appear in the spectrum. Conventionally, the positive energies are assigned to Stokes shifts and negative energies to anti-Stokes. Given the spectrometer divides the scattered light into two different directions, the anti-Stokes signal appears in the opposite position in relation to the Stokes signal. The probability of these processes depends upon the excitation energy E_i and the temperature.

All the discussion above refers to the most usual and fundamental scattering processes witch are called first-order. In these processes the energy exchange between the incident light and the specimen excites only one phonon in the crystal with a very small momentum (q≈0 to satisfying the fundamental Raman selection rule). However it is probable that two or more phonons get excited during the Raman process; which in this case they are termed *second-order or higher-order* processes. The wavelength selection rule in this case is that the two phonons must have equal wavevectors but must be travelling in opposite directions (q+(-q)=0). The second order processes are normally weaker than the first-order events but they are enhanced by some means, they carry precious information about the overtones and combination modes especially for thin films on a substrate [117, 118].

1.6.2 Raman Spectroscopy of Graphene

Figure 1.31 shows a typical Raman spectrum of monolayer graphene transferred onto SiO_2/Si substrate. As mentioned briefly in the introduction, the linear gapless electronic dispersion of graphene entails resonance for any excitation frequency. Being the simplest and the building unit of all the graphitic carbons, the graphene Raman spectrum is also the simplest; consisting of few prominent peaks in the range of 1000–3500 cm^{-1}. The point group symmetry of ideal single layer graphene is D_{6h}. There are two equivalent atoms per unit cell in graphene, giving six normal modes for the Brillouin zone centre. The irreducible representations for the zone centre modes of a single layer are given by: $\Gamma = A_{2u} + B_{2g} + E_{1u} + E_{2g}$ (see Figure 1.32).

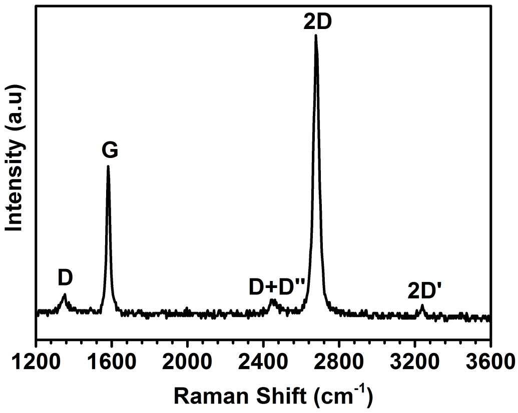

Figure 1.31 Typical Raman spectrum of monolayer graphene.

The A_{2u} represents translation perpendicular to the graphene plane and E_{1u} represents the translation in the graphene plane. These two modes are acoustic modes in graphene. The B_{2g} mode is an inactive optical phonon where the carbon atoms move perpendicularly to the graphene plane. The E_{2g} mode is a doubly degenerate Raman active optical vibration, where the carbon atoms move in the graphene plane. In the first-order Raman spectrum of monolayer graphene we expect only one Raman active E_{2g} mode at $\approx$ 1580 cm^{-1} known as G peak (Figure 1.33 (a)). However, for bilayer/multilayer graphene (same as graphite) there is an additional first-order optical phonon which is due to the relative motion of the graphene layers. This mode has been called C mode as it is sensitive to the interlayer coupling [119]. Another Raman-allowed feature in graphene Raman spectrum is the 2D band (seen in all kinds of sp^2 materials) which appears at

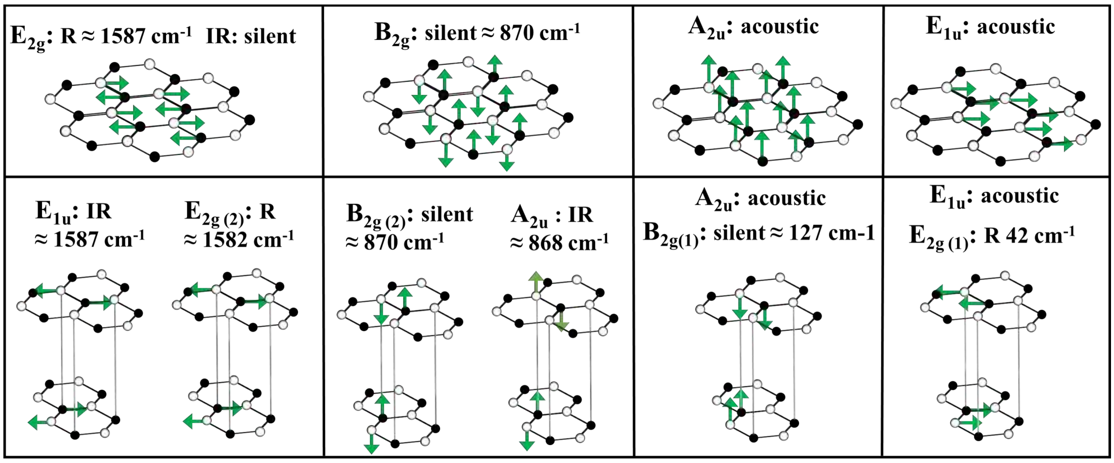

Figure 1.32 Phonon displacement vectors at the centre of the Brillouin zone in graphene (top) and graphite (bottom). The fiiled and empty circles represent unequal carbon atoms and the green arrows mark the displacement pattern. R stands for Raman-active and IR label shows infra-red active modes.

$\approx 2700\,\mathrm{cm}^{-1}$. The 2D peak originates from a second order scattering process of two in-plane transverse optical phonons (see Figure 1.33 (b)) which accounts for the dispersive nature of this peak; meaning the frequency of the peak changes linearly with the excitation laser energy ($\omega_{2D} = \omega_{2D}(E_{laser})$. Another second-order scattering process can occur in defective graphene giving rise to the so-called D peak is also present at $\approx 1360\,\mathrm{cm}^{-1}$ activated by one in-plane transverse optical phonon plus a defect acting as a scattering centre (see Figure 1.33 (c)).

There are other peaks in the graphene Raman spectrum which are less important in terms of information they can provide. Below the effect of various external factors on the shape and position of the main bands in graphene will be discussed.

1.6.2.1 Number of Layers and Stacking Order

Number of Layers

The 2D band in the graphene Raman spectrum is one of the most sensitive gauges for graphene layer number determination. This strong sensitivity lies in the nature of 2D band being promoted by double resonance scattering processes. Any disruption in the electronic and/or phonon dispersion of graphene will directly influence the 2D band. This effect manifests itself in as a change in the number of possible fit components to 2D peak as well as the full width at half maximum (FWHM) of the peak. While in monolayer graphene the 2D band can be fitted by one single very intense Lorentzian curve and is roughly four time more intense than the G peak [68], upon adding more graphene layers, the 2D peak can be fitted with more than one Lorentzian curve which is an indication

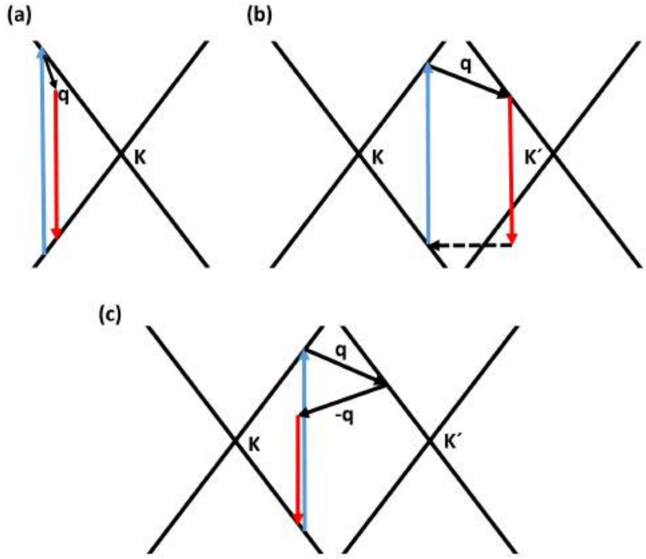

Figure 1.33 Diagramatic illustration of the order of Raman processes. The blue solid arrows show photon absorption, the red solid arrows show photon emission, the black solid lines show phonon emission and black dashed lines show an elastic scattering event. (a) First-order one-phonon Raman process. (b) Second-order one-phonon process and (c) second-order two-phonon process.

of the higher number of possible double resonance scattering processes. For instance, the 2D peak in bilayer graphene can be de-convoluted into four peaks, reflecting the changes in the electronic band structure brought about by coupling between graphene layers. These four components include: $2D_{1B}$, $2D_{1A}$, $2D_{2A}$ and $2D_{2B}$; two of which, $2D_{1A}$ and $2D_{2A}$, have higher relative intensities than the other two [68]. A further increase in the number of layers leads to a significant decrease of the relative intensity of the lower frequency 2D peaks and for more than 5 layers, the Raman spectrum becomes hardly distinguishable from that of graphite. As mentioned, the FWHM of the 2D peak changes as well upon the addition of layers to graphene. For example, the FWHM of turbostratic graphite is 50 cm^{-1} almost twice as high as the 2D peak of graphene (30 cm^{-1} and up-shifted by 20 cm^{-1} [68].

Stacking Order

2D peak assessment can also be used to study the stacking order in multilayer graphene. The lineshape of the 2D band changes remarkably by any change in the interlayer stacking sequence namely Bernal-stacking or non-Bernal. This stems from the modification of electronic band structure of graphene upon stacking order alteration. For instance, in AB-stacked bilayer graphene, the 2D peak shows a lineshape common to the four peak spectrum (see the green spectrum in Figure 1.34 (d)). However, in a non-AB stacked twisted bilayer graphene (incommensurate BLG), a single 2D peak typical for monolayer graphene is observed (sse the blue spectrum in Figure 1.34 (d)).

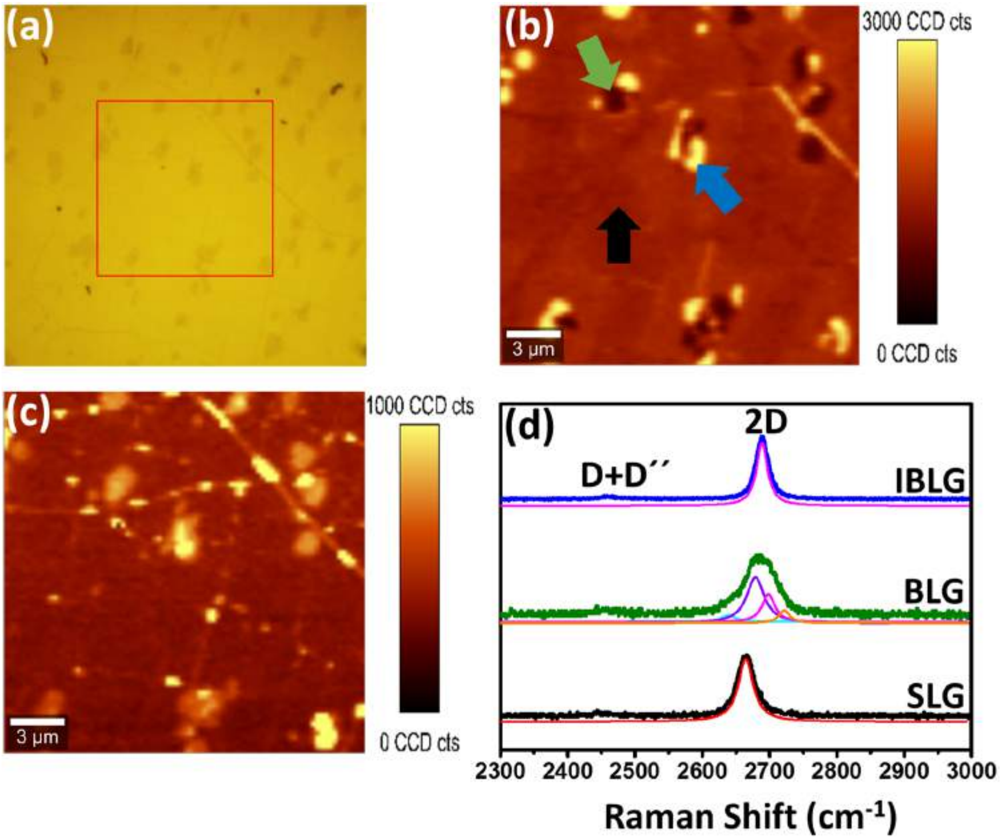

Figure 1.34 Effect of layer number and stacking order on the linewidth and the position of 2D peak. (a) 2D band sum map; (b) corresponding G band sum map in the same area;(c) Stacked Raman spectra taken from single-layer (SLG) area, bilayer graphene (BLG) point and the incommensurate bilayer graphene (IBLG) marked with black, green and blue arrows, respectively.

In this case, only one double resonance process takes place along the conduction bands of the graphene layers resembling the presence of Dirac electrons. Nonetheless, the 2D peak is normally up-shifted in the case of twisted bilayer graphene. One important point that should be sought when assigning the stacking order and layer number in CVD samples in particular, is to bear in mind that fitting the 2D peak with one Lorentzian does not necessarily mean that the sample is monolayer as this could be the case for turbostratic or twisted few-layer graphene.

1.6.2.2 Defects and Disorders

The presence of disorder in sp^2-hybridised carbons which are known as high symmetry materials, leads to the an effect called defect-induced symmetry breaking which gives rise to emergence of additional double resonance peaks in the Raman spectra;

making Raman spectroscopy a very sensitive tool to study the defects and disorder in graphitic materials. Essentially, the symmetry requirement of selection rules originates from momentum conservation. Introduction of defects into the crystal lattice effectively results in the momentum conservation breakdown and, thus, allows the activation of the symmetry-forbidden modes. Qualitatively, introduction of defects is accompanied with the broadening of Raman-allowed bands (such as G and 2D band) as well as the appearance of the new peaks in the spectrum which are symmetry-forbidden (e.g. D and D').

Figure 1.35 shows CVD graphene patterned lithographically into rings and squares where the transfer-mediated contamination has given rise to modulation of the Raman spectrum of monolayer graphene. Panel (a) and (d) show the optical images of the graphene ring and square patterns, respectively. Panel (b) and (e) are the corresponding 2D band intensity maps of panel (a) and (d), respectively; the inset in (e) is the D peak intensity map of the square pattern edge, highlighting that main contribution to the D peak is from the edges. Panel (c) and (f) are the average spectra taken from the area in panel (a) and (d), containing an intense D peak and other defect-induced peaks namely $D+D''$, $D+D'$ and $2D'$.

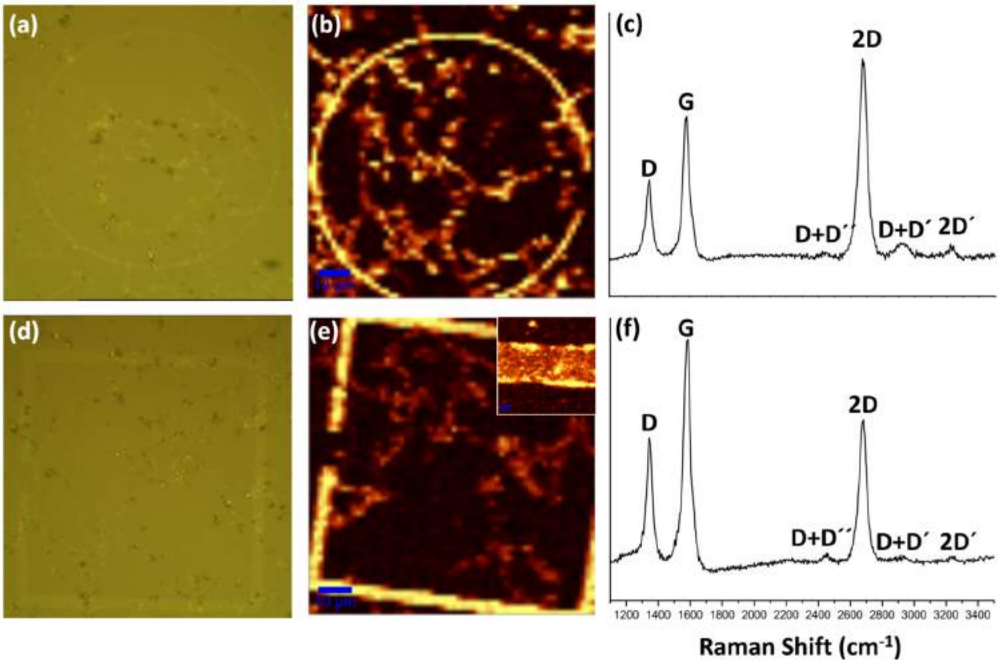

Figure 1.35 Raman spectroscopic analysis of graphene ring and square patterned via photolithography. (a, d) Optical images of the patterns. (b, e) 2D band intensity maps of panel (a) & (d), respectively. (c, f) Average spectra of the ring and square patterns in (a) & (d), respectively.

1.6.2.3 Effect of Doping

The effect of doping on the Raman spectrum of graphene originates from the refinement of the contribution of electron-electron scattering to the inelastic scattering process; which itself is a result of the modulation of charge carriers concentration (Fermi energy) upon doping. Since 2D peak is very sensitive to any perturbation in the band structure in graphene, it will experience minor to major changes depending on the doping level [120]. Furthermore, doping results in Fermi energy-dependent blueshift and narrowing of the G peak as it changes the occupation of electronic states. This can make the transition from an empty state or to a filled state impossible, hindering the Raman scattering.

1.6.2.4 Effect of Isotopic Composition

Isotope carbon exists in a natural abundance of 1.1% [121]. Isotope-labelling has been used in the field of graphitic materials research to study the growth mechanisms as well as phonon properties; for instance for structural characterisation of ^{13}C-labelled graphite oxide [122], Raman spectroscopy of ^{13}C isotope-enriched single wall carbon nanotubes [123] and study of CVD growth mechanism of graphene [124]. The main principle employed in such studies is the atomic mass difference between ^{12}C and ^{13}C which manifests itself as modulation of Raman spectrum of graphene. The effect of mass on the vibrational energy levels can be described by incorporating the Hook's law to the harmonic oscillator in a diatomic model consisting of two atoms with m_1 and m_2 atomic weights. The dependency of vibrational frequencies on the atomic mass is expressed by the following equation:

$$\omega = \frac{1}{2\pi}\sqrt{\frac{k}{\mu}} \tag{1.17}$$

where k is the force constant and μ is called reduced mass and is defined as $\mu = \dfrac{m_1 m_2}{m_1 + m_2}$. Therefore, when an atom is replaced by an isotope of larger mass, μ increases, leading to a down-shift of the peaks in the spectrum. It is also possible to estimate the band frequencies, ω, upon isotope enrichment by the following relation [125]:

$$\frac{\omega_0 - \omega}{\omega_0} = 1 - \sqrt{\frac{12 + c_0}{12 + c}} \tag{1.18}$$

where ω_0 is the frequency of a given band in the ^{12}C sample, c is the purity of the isotope gas precursor and c_0=0.0107 is the natural abundance of ^{13}C. According to this equation, higher frequency peaks undergo a larger frequency shift. For instance in a 99% ^{13}C sample measured by a 514 nm laser, the 2D peak will down-shift by 104 cm^{-1}

whereas D and G peak shift by $52\,\mathrm{cm}^{-1}$ and $61\,\mathrm{cm}^{-1}$, respectively. Apart from frequency shifts, broadening of G peak has also been observed as a function of ^{13}C concentration. It is pointed out here that the spectral band width is inversely proportional to the phonon's lifetime. It has been theoretically shown that for the G band [126], the phonon lifetime increases gradually and reaches a maximum at 50% ^{13}C isotopic concentration where the FWHM equals $\approx 16.4\,\mathrm{cm}^{-1}$. After this maximum, for higher isotope concentrations the spectral width decreases and reaches to $\approx 12\,\mathrm{cm}^{-1}$ at 100% ^{13}C concentration. Another factor that contributes to the linewidth of the Raman bands is the phonon mean free path which itself is related to the localisation length of phonon wave function. It has been calculated that the typical localisation length is in the order of 3 nm for high ^{13}C concentrations.

Chapter 2

Experimental Methods

2.1 Chemical Vapour Deposition

CVD is a widely-used technique for the production of thin films of different materials for both industrial and research applications. This method involves the reaction of gaseous precursors introduced into a reactor followed by a series of chemical reactions on a suitable substrate, these can be activated thermally or via a plasma-source energy; which then leads to the deposition of a thin film on the substrate surface. A typical CVD process consists of the following steps: (I) Transport of precursors by means of convection into the reactor (chamber). (II) Reactions of precursors in the active zone and production of reactive radicals and gaseous by-products. (III) Gas diffusion of reactive species to the substrate surface. (IV) Adsorption of the reactive species on the substrate surface. (V) Thermally-assisted reaction processes, diffusion and nucleation and formation of a thin film. (VI) Desorption and out-diffusion of the remaining by-products. In the next section, various types of CVD reactors are introduced briefly.

2.1.1 CVD Reactors

CVD as a technique has gone through many years of development and modification, as such there are many different styles of CVD reactors available in the market; nonetheless they all share some common features and components regardless of their manufacturer: (a) Precursor sources. (b) A gas-handling mechanism to regulate the input of precursor gases into the reaction zone. (c) The active zone, which is heated by a surrounding heating element and can hold the substrate steadily and safely. (d) An exhaust mechanism, which may well comprise of a vacuum pump to remove the discarded by-products and for low-pressure processes. There are two main categories of reactors in terms of thermal budget: **Tube reactors.** (or hot wall reactors) represent a major category of CVD reactors. Commonly in tube reactors, the chamber containing the substrates is surrounded by a furnace that heats the system. The substrates are loaded into the system, heated to the desired temperature, and then the reactive gases are introduced. The research-scale reactors are often run at elevated temperatures so they are fabricated from Pyrex glass or quartz tubes; and the tubes are cylindrical for flow symmetry and the requirements for structural integrity under vacuum. Generally, hot wall reactors have the advantage of providing a relatively uniform substrate temperature and thus film thickness. **Cold wall reactors.** These reactors are another major category of CVD reactors. In these reactors, the substrate is at higher temperature than chamber walls and irradiation or heating coil is used to generate heat. The benefit of these reactors is that the reaction just happens on the substrate. Deposition on the reactor walls and control over temperature gradient are main disadvantages of these reactors.

2.1.2 Preparation of CVD Graphene

CVD technique as the method of choice, for synthesis of large-area (up to millimetre size) monolayer graphene on metal films has been explored widely in various respects. On this basis, CVD technique was employed throughout this work for production of graphene.

The choice of catalytic metal substrate is crucial to the CVD growth. Today, it is well-established that graphene growth on nickel does not yield uniform monolayer graphene and typically, a mixture of monolayer and few layers is obtained. This is due to the formation very strong bonds to carbon compared to copper. For this reason, unlike copper, nickel supports formation of C−C bonds as seen in CNTs growth. On the other hand, it has been shown that copper is an excellent candidate for making large area, uniform thickness (95%) single layer graphene films due to the low solubility of carbon in copper [39]. Therefore, copper was chosen as the catalytic substrate for graphene CVD process. Methane was used as the carbon feedstock; due to its more controllable decomposition at CVD conditions for graphene growth.

2.1.2.1 Process Steps

From a practical point of view, there are some important steps to be implemented prior to the exposure of the catalyst surface to the gas precursors. Firstly, a rinsing step with acetone followed by washing off in DI water is usually beneficial to remove the organic residues on the copper foil surface. The CVD process of graphene typically consists of the following steps:

Ramping. This step involves controlled heating of the catalyst substrate and gases (in hot wall reactors), normally in an inert/reducing atmosphere, up to the desired process temperature. During this step, any possible oxide species on the catalyst surface is removed.

Annealing. Includes maintaining the temperature of the reactor chamber at a set-point. This step mainly serves to increase the grain size of the metal catalyst up to ≈ 100 µm. Nonetheless, excessive temperatures should be avoided to minimise the metal substrate sublimation (e.g. copper melts at 1085 °C).

Growth. This step entails introduction of the carbon precursor together with an adjusted flow of the inert/reducing gas used in the previous steps. The growth of graphene over the catalyst substrate is achieved by running this step for a set duration of time. It should be noted that depending upon the nature of the catalyst (solubility, catalytic action, etc), the graphene may grow during this step or in the next one.

Cooling step. After the growth step, the next step is cooling the reactor in an inert/reducing atmosphere. The atmosphere commonly used is similar to that of the annealing or growing step, until the reactor temperature is under 200 °C to prevent oxidation of the catalytic surface not covered or functionalisation with oxygen moieties. When working with substrates that have high carbon solubility (for example Ni), cooling step dynamics are critical to control the growth due to the established contribution of carbon segregation to graphene growth.

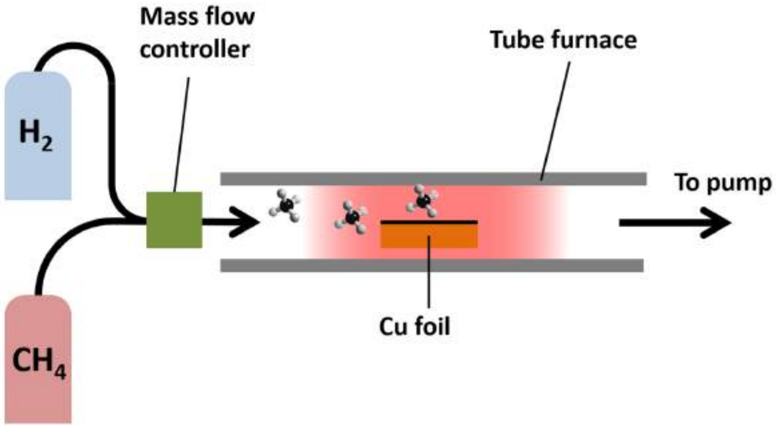

Figure 2.1 Schematic representation of the CVD process for graphene growth.

2.1.2.2 Experimental Set-up

As mentioned above, Prior to loading the copper substrate into the furnace, a substrate preparation procedure is completed. In a typical growth in this work, the as-purchased copper foil (Gould GmbH, 25 µm) was immersed in 10 % HCl solution (Sigma-Aldrich) for 30 seconds to remove the backside chromate and then rinsed in Millipore water thoroughly. Subsequently, the copper foils were sonicated in HPLC grade acetone for 5 minutes.

The graphene was grown by CVD in a hot-wall quartz tube furnace. Copper substrates were loaded into the furnace and ramped up to 1035 °C under 50 sccm flow of hydrogen. Then the furnace was maintained at this temperature for 10 minutes so as to modify grain size of the copper substrate. Graphene was grown by passing a mixture of 10 sccm methane and 5 sccm hydrogen (H_2). Then a dribble flow of H_2 (2.5 sccm) was set and the furnace was force-cooled to room temperature via compressed air.

2.2 Graphene Transfer to Si/SiO$_2$ wafer

For realising many practical applications of CVD-grown graphene (e.g. electronics, optoelectronics and photovoltaics) the graphene sheet has to be transferred from the copper substrate onto an appropriate substrate, normally a dielectric material [127]. In the standard chemical transfer procedure, graphene is transferred to the target substrate using Poly(methyl methacrylate) (PMMA) [128]. The PMMA is dissolved using acetone, leaving the graphene sheet on the desired substrate.

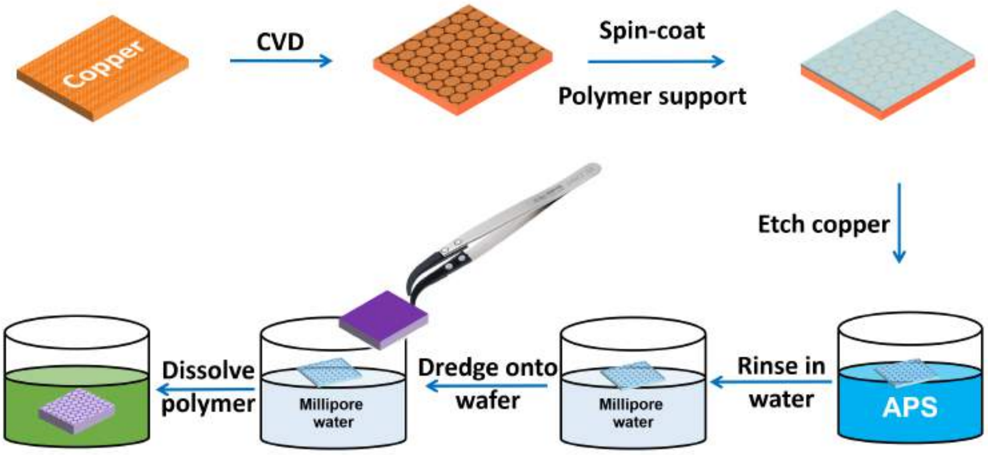

Figure 2.2 Schematic representation of the graphene transfer process onto wafer.

While this is a straightforward procedure, the acetone treatment frequently fails to fully remove the PMMA, leaving residues on the graphene surface which are detrimental to the physical and electrical properties of graphene [129, 130]. Commonly Iron Chloride (III) $FeCl_3$ and Ammonium Persulfate (APS) are used as copper etchant in the graphene transfer process. These chemicals are the reason for contamination of problem; $FeCl_3$ leaves an electrically active residue of metal ions on the graphene and APS is a crosslinking agent for PMMA. In our group, an efficient and feasible transfer method has been developed which is based on the application of cellulose polymers [131]. This method results in minimal polymer residues and associated strain. In this work, initially the PMMA-based transfer method was used and more recently, the cellulose polymers (Nitrocellulose (NC) & Cellulose Acetate Butyrate (CAB)) were adapted for this purpose.

In practice, the polymer solution was spin-coated onto the as-grown graphene on copper and after etching away the copper using Ammonium Persulfate (APS), the polymer-graphene stack was dredged onto the wafer. After an initial air-drying, samples were annealed in a vacuum oven to improve the adhesion of graphene to the substrate. Finally, the polymer layer was dissolved in acetone at room temperature. Figure 2.2 shows schematically the graphene transfer process flow.

2.3 Remote Plasma Functionalisation

As mentioned before, graphene is an ideal candidate for electrochemical applications. However, pristine graphene is rather inert. In order to realise practical applications in electrochemistry and sensing, one of the efficient methods is introduction of functionalities on the surface of graphene. In this work, a remote plasma functionalisation of graphene was employed for this purpose [79].

This process involves an oxygen plasma exposure followed by a H_2+NH_3 plasma. The first step of treatment creates oxygenated species (e.g. carbonyle and carboxylic acid) and the second step leads to reduction of oxygenated species and N-doping of graphene from NH_3. This procedure is discussed further in Chapter 6.

The plasma unit is ”chemical” plasma by a remote source (R3T TWR 2000-GEN, 400 V,1000 W). A schematic and a picture of the set up used in this experiment are shown in Figure 2.3. There are three main parts in this set-up, plasma control module (shown in red in Figure 2.3 (a) & (b)), mass flow controllers (see Figure 2.3 (a)) and the heating furnace. The plasma unit is a programmable unit enabling accurate setting of plasma mode and power. The Mass Flow Controllers (MFCs)-enabled controlled adjusting of flow and the gas used for striking the plasma in the furnace. The furnace accommodates the sample.

2.4 Raman Spectroscopy

A Raman system typically consists of four major components: (1) Excitation source (Laser). (2) Sample illumination system and light collection optics. (3) Wavelength

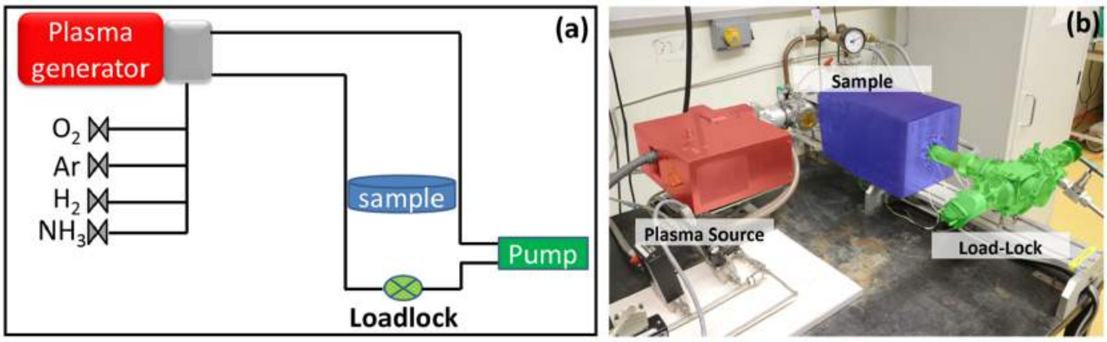

Figure 2.3 (a) Schematic representation of plasma treatment furnace set-up. (b) Picture of the furnace with its sections highlighted.

selector (Filter or Spectrophotometer). (4) Detector (Photodiode array or CCD). The sample is normally illuminated with a laser beam in the ultraviolet (UV), visible (Vis) or near infrared (NIR) range. Scattered light is collected with a lens and is sent through the filter or spectrophotometer to obtain Raman spectrum of the sample. Since spontaneous Raman scattering is very weak the main difficulty of Raman spectroscopy is separating it from the intense Rayleigh scattering. More precisely, the major problem here is not the Rayleigh scattering itself, but the fact that the intensity of the Rayleigh scattering may greatly exceed the intensity of the useful Raman signal in the close proximity to the laser wavelength. In many cases the problem is resolved by simply cutting off the spectral range close to the laser line.

Figure 2.4 shows schematically various components of a Raman system. The first part is the laser which produces the probe in the Raman spectroscopy, a monochromated light. The incident light is scattered at the surface of the sample. Then the filter is used to block out the incident light. Raman scattered light is then transmitted through the filter and directed to the detection system.

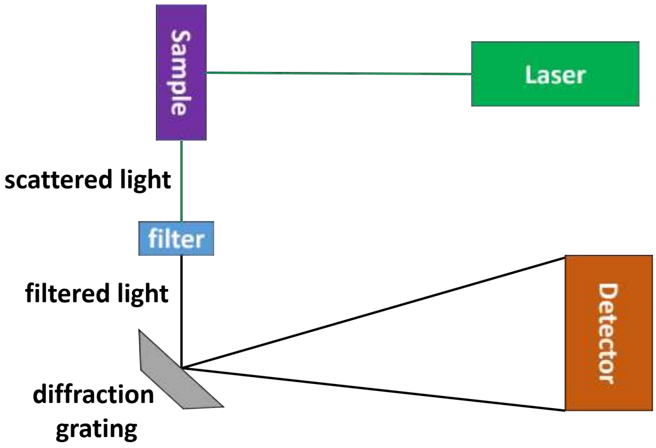

Figure 2.4 Simplified schematic illustration of a Raman system.

2.5 Scanning Electron Microscopy

All SEMs regardless of their manufacturers share the following parts: Electron source (gun), electromagnetic lenses, sample stage, detectors, vacuum parts and power supply units and output displays. The schematic below shows general layout of an SEM instrument. The electron gun is responsible for providing a stable intense beam of electrons.

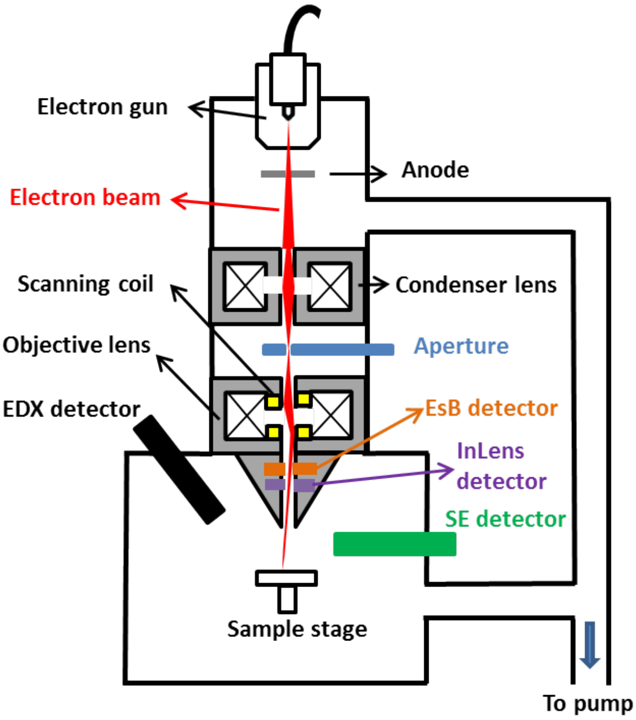

Figure 2.5 Schematic of an advanced SEM equipped with different detectors.

There are two main types of electron source namely thermionic and Field Emission Gun (FEG). In order to convey the electron beam to where it is needed and manipulate the final beam size striking the specimen, a number of electron lenses are present in the microscope column. They are made of a set of copper coils and once current passes through them, a strong magnetic field is created which is used to control the electron beam. The signals generated upon electron beam-sample interaction, are detected by various detectors such as SE, BSE, InLens, STEM and X-ray, and then converted to digital images or spectra to be displayed on the screen.

Graphene is an ideal sample for SEM studies as it is very conductive and does not require any particular sample preparation. All the SEM work in this study was carried out without any additional sample preparation unless otherwise stated. SEM measurements were carried out using a Zeiss Ultra Plus microscope equipped with a FEG and EDX spectrometer (Oxford Instrument INCA system) with a Gemini column with which imaging resolution of 1 nm using InLens/SE2 detector and 0.8 nm with STEM detector could be achieved. Low accelerating voltages in the range 1-5 kV were used to minimise beam-induced damage in carbon materials. The microscope was equipped with a charge 12 neutralisation system enabling imaging of non-coated insulating materials.

2.6 Transmission Electron Microscopy

Modern microscopes can be equipped with a number of detectors for special imaging modes and compositional analysis (see Figure 2.6).

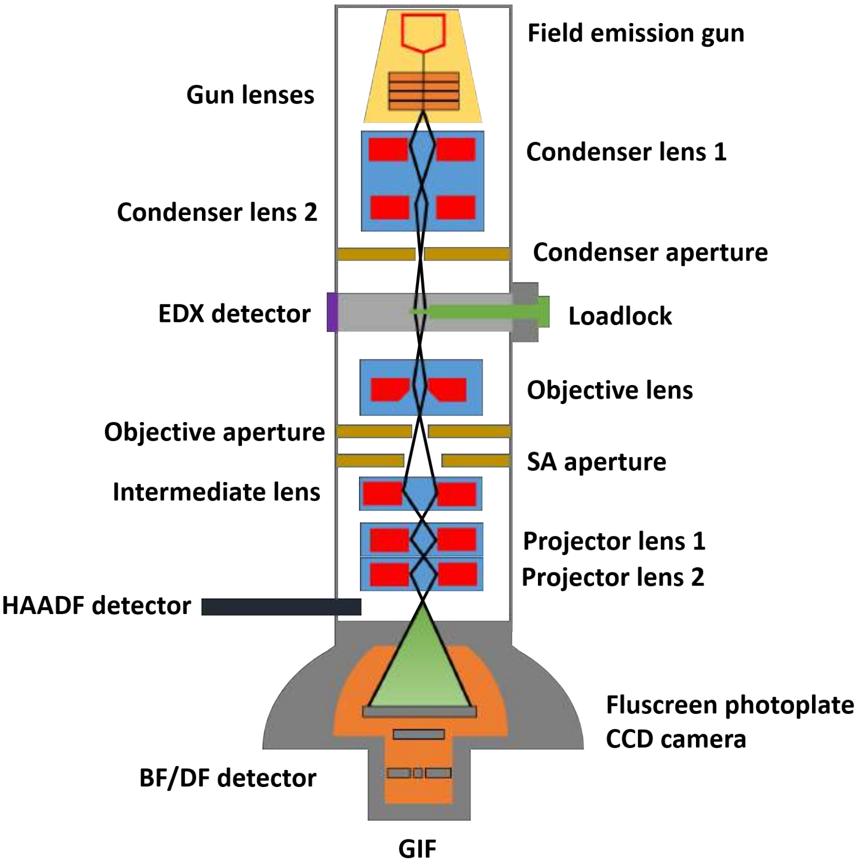

Figure 2.6 Schematic cross-section of FEI 80-300 (S)TEM column, used in this work.

This includes EDX detector for localised X-ray analysis, BF and DF detectors, High Annular Angle Dark Field (HAADF) detector for STEM mode. Additionally, as mentioned in the previous chapter, aberration correctors are becoming a more standard part of TEM instruments.

Another useful feature found in all most modern TEM machines, is energy-filtered imaging (EFI) carried out using a magnetic prism acting as an energy filter for transmitted electrons. Furthermore, EELS can also be performed using the energy filter.

In this work, routine TEM studies were performed using an FEI Titan 80-300 (S)TEM equipped with a S-TWIN objective lens and a high brightness (X-FEG) Schottky field emission gun. The nominal point resolution was 0.1 nm, lattice resolution <0.102 nm, information limit 0.1 nm, energy resolution <0.4 eV and HAADF-STEM resolution was equal to 0.136 nm. Spherical aberration was less than 5 nm and chromatic aberration was equal to 1.6 nm. The specimen holder was a double-tilt low-background CompuStage holder. The X-ray analyser was an EDX energy dispersive X-ray detector with SUTW window, with 30 mm^2 active area and 10 mm specimen in which the detector distance was enabling a solid collection angle of 0.13 steradians and the resolution of the detector was 135 eV at Mn k-edge at 100 eV. A Fischione HAADF detector in STEM mode enabled Z-contrast imaging. The charge-coupled device (CCD) was a Gatan US1000 CCD system located above the image filter for HRTEM work. Apertures were fully computer-controlled and motorised. The microscope had an embedded energy filter (tridiem 863) equipped with 2K×2K CCD for EFTEM imaging and elemental mapping and also electron energy loss spectroscopy (EELS).

2.7 TEM sample preparation

The first step in carrying out a TEM analysis, is to transfer the specimen effectively onto a TEM support. Furthermore, as the name of the technique implies, TEM requires a thin enough specimen, which allows the electrons to transmit through. For thin, light element samples such as graphene, any support film would produce a stronger contrast than the material itself. Hence, the sample has to be free-standing. As mentioned previously, CVD has found its place as the method of choice to produce large-area high-quality graphene. With the widespread availability of large-area, CVD synthesised graphene on metal surfaces, the transfer of CVD grown samples to standard TEM grids [67] currently appears to be the most efficient route to obtain free-standing membranes in a TEM-compatible geometry.

Nevertheless, cleanliness has remained a challenge for the preparation of TEM samples from CVD graphene primarily due to the presence of polymer residue arising from transfer processes [132]. For clean transfer of CVD graphene to TEM grids, an optimised version of a polymer-free transfer technique, called the direct transfer method [133], was employed. In this method, graphene is transferred to lacey carbon TEM grids without a polymer support and then baked in High Vacuum (HV). This method is shown schematically in Figure 2.7.

To implement this method, one should first take into account that graphene coats both sides of the copper foil when synthesised via CVD process (see Figure 2.7 (a)). Thus, in

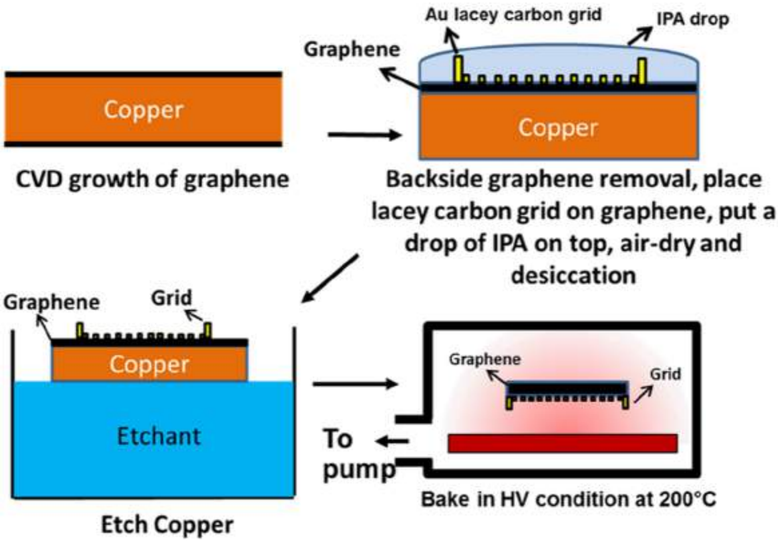

Figure 2.7 Schematic illustration of TEM sample preparation.

order to minimise the formation of defects during transfer process, the backside graphene should be removed. This is done by first chemically etching the backside of the copper foil for a few minutes and then submerging it in DI water. The surface tension from the dipping step pulls away the loose graphene on the backside of the foil. The edges of the copper foil are then trimmed and cut to the desired size. Subsequently, a gold lacey carbon grid is placed on top of graphene and then a drop of Isopropyl Alcohol (IPA) is dropped on top of the TEM grid. IPA was chosen as it is a low boiling point solvent and also safe to work with. The IPA wets the gap between the amorphous carbon coating on the TEM grid and the graphene (see Figure 2.7 (b)). As the IPA evaporates, the lacey carbon of the TEM grid comes into intimate contact with the graphene underneath. After air-drying, sample is heated on a hotplate at 150 °C to improve the adhesion. Sample is then floated on APS etchant for 40 minutes to completely etch away the copper substrate (see Figure 2.7 (c)). Finally, the TEM grid/graphene is scooped out from the etchant and rinsed off in two subsequent DI water baths, air-dried and kept in a desiccator for 2 hours to improve the adhesion. Sample is then placed in an HV chamber (10^{-3} Pa base pressure) and baked at 200 °C to improve the cleanliness. The sample is then loaded into the TEM column with minimum handling, and further cleaned once inserted in the TEM column using the so-called beam showering method. This transfer method was used for most of the TEM studies in this work, unless otherwise stated.

Figure 2.8 shows SEM images of graphene membranes suspended on TEM grid using this method. Figure 2.8 (a) highlights the large-area coverage on several squares where graphene is suspended on TEM support. Figure 2.8 (b) is the zoomed-in image of the square marked with red circle in image (a), indicating presence of suspended graphene

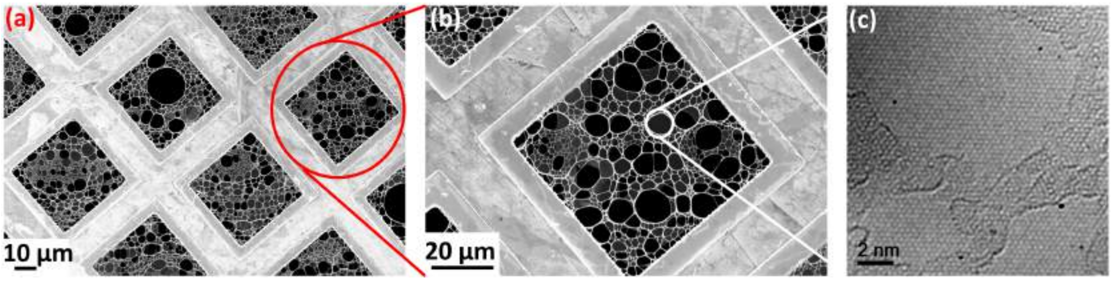

Figure 2.8 (a) Low-mag SEM image of graphene transferred onto lacey carbon TEM grid. (b) Zoomed-in image of the area marked with red circle in (a). (c) AC-HRTEM image of the graphene film shown with white circle in image (b).

over tens of micrometres. Figure 2.8 (c) is the HRTEM image of monolayer graphene transferred using this approach, showing the atomically-resolved lattice of graphene.

2.8 Electron Energy Loss Spectroscopy

2.8.1 Spectrometer

The spectrometer essentially works on a similar concept, a prism in light optics; meaning the incoming electrons are divided based on their wavelength which in turn is related to their (lost) energy, using a magnetic field. Similar to spectra generated by X-ray based techniques, different edges can be observed in an EEL spectrum such as K,L,M and so forth. However unlike X-ray, electrons crossing through a thin sample may lose any amount of energy which provides higher resolution down to 1 eV or less for analytical purposes. Advances in the electron optics and aberration corrections especially chromatic aberration, have enabled researchers to carry out spectroscopy down to single atom level and with resolutions in the order of 0.1 eV [134, 135]. Additionally, this versatile analytical capability can be incorporated with imaging in S/TEM to facilitate site-specific analysis [136, 137] which is not achieved by other sensitive spectroscopic techniques such as X-ray Photoelectron Spectroscopy (XPS). Figure 2.9 shows a schematic illustration of energy-filtered imaging and spectroscopy using a post-column type of filter. Briefly described, electrons are collected after specimen and dispersed using a magnetic prism. An EELS spectrum is a trace across the dispersion plane. The desired energy window can then be selected using a slit and the image is re-formed by a combination of lens arrays. Finally, the image is then recorded by a CCD camera and displayed in the screen for the user.

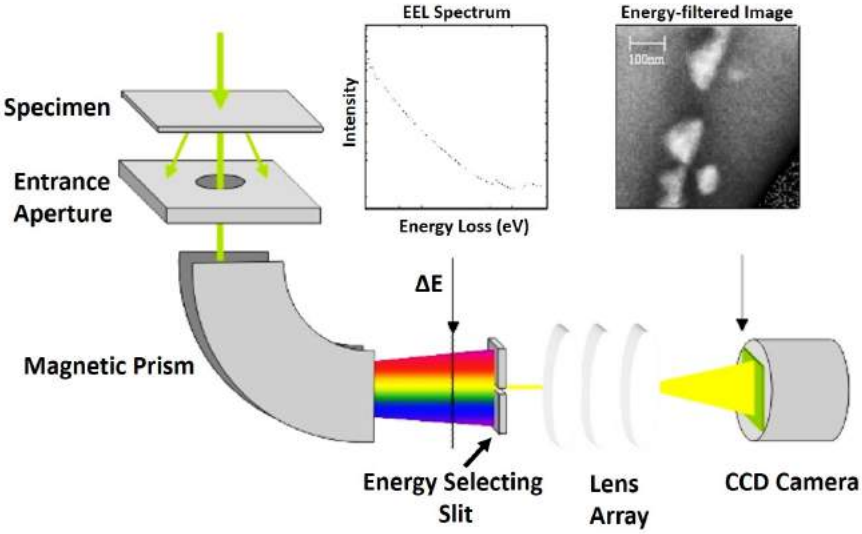

Figure 2.9 Schematic illustration of energy-filtered imaging and spectroscopy (adapted from [138]).

2.8.2 Energy-Filtered Imaging

The inelastically scattered electrons can additionally be employed to form an energy-filtered image; which is commonly termed Energy-Filtered TEM (EFTEM). By means of this technique, high spatial chemical mapping of the sample within a short acquisition time is possible.

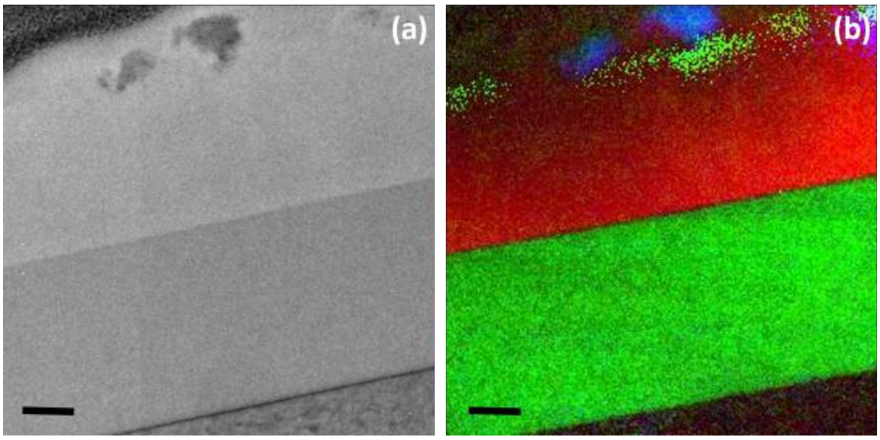

Figure 2.10 (a) Cross-sectional TEM image of a PyC thin film on a SiO_2/Si wafer, and (b)corresponding EFTEM elemental map showing the distribution of present elements. Red is carbon, green is oxygen and blue is nickel. Scale bars are 100 nm.

In practice, first the ionisation edge of the element of interest is set to be passed through energy selecting slit. Then, by sequential recording of energy-filtered images from the area of interest, a spatial distribution of element(s) of interest is generated as an image. It is also possible to carry out the measurement using a STEM beam and sequentially record

EEL spectra. This technique is called Electron Spectrum Imaging (ESI). Figure 2.10 shows a cross-section TEM image of a PyC sample (shown in (a)) and the corresponding EFTEM elemental map (see (b)), showing the distribution of oxygen (green), carbon (red) and nickel (blue).

Cross section samples were prepared using a dual beam Zeiss Auriga Focused Ion Beam (FIB) microscope equipped with both field emission electron and Ga^+ ion columns. The system was fundamentally designed for nanofabrication via controlled localized ion milling or ion assisted deposition which could be simultaneously monitored with the SEM column. The microscope had a state of the art Orsay Physics Cobra ion column with a unique 2.5 nm resolution. Ion and electron imaging resolution were 2.4 nm and 1 nm, respectively. Additionally, a micro-manipulator was dedicated for TEM lamella preparation. A reactive gas injection system was used for reactive deposition of a platinum capping layer. The welding of micro-manipulator and subsequent lift out were carried out at 54° tilt angle. Consequently, the attached lamella was carried away and now welded to a specific holder (Omniprobe) designed for cross-section work. Finally, the further thinning of the lamella was performed at lower ion energies and voltages down to 5kV, 50 pA to achieve minimal ion implantation and desired thickness for electron transparency ($<$100 nm for HRTEM work and $\leq$ for EELS analysis).

Chapter 3

TEM of Carbon-based Nanomaterials

This chapter is adapted from the papers [5], [7], [8] and [10] mentioned on the page xi. One of the key factors that strongly affects the success rate of any TEM analysis of graphene, is the sample preparation step. If one does not have a large-area reasonably clean graphene sample mounted on a TEM support then even access to the most advanced state-of-the-art TEM machine will not yield quality images. Therefore, to ensure that a graphene sample has met the minimum requirements before TEM analysis, establishing a reproducible CVD growth protocol that produces high-quality large-area graphene sheets, is the first essential step. The next step is a transfer method that can provide a relatively clean graphene mounted on a TEM grid.

To this end, first, the scanning Raman spectroscopy and SEM analyses of graphene sheets (produced by the method described in Chapter 2 under section 2.1.2) confirming the above-mentioned qualities, are presented. Then, a modified transfer process to TEM is discussed and finally, some empirical results on TEM of graphene and nanocarbons are outlined.

3.1 Large-area High-quality Graphene

As mentioned in Chapter 1, among all the metal substrates, copper has shown to be the most reliable choice of catalyst for reproducible growth of monolayer graphene over a large area. A number of parameters govern CVD growth of graphene on copper foil namely, growth temperature, methane concentration (given as a ratio of methane-to-hydrogen flow rates), total pressure and the growth time. Based on an extensive literature survey and a comprehensive range of experiments, the optimum conditions for graphene CVD growth in our experimental set-up were attained (as mentioned in Chapter 2, under 2.1.2.2). Extensive characterization of the graphene layers after growth and also transfer of graphene was performed using field emission scanning electron microscopy (FE-SEM), optical microscopy, conventional Raman spectroscopy whose results are summarised below.

In order to assess the quality of as-grown graphene, SEM analysis was performed directly on as-grown graphene. A low 1-2 kV acceleration voltage was used for all the SEM measurements, ensuring the minimum beam-induced damage to graphene. Figure 3.1 shows typical SEM images of as-grown CVD graphene on copper foil. In Figure 3.1 (a), for the sake of easier differentiation of graphene domains from the copper substrate, the growth was halted just before the domain coalesced. In this image the white areas are the copper substrate and the dark areas are graphene domains. The hollow red arrows mark the multilayer islands, observed commonly in CVD growth of graphene on copper. Image (b) depicts graphene with full coverage over large areas. Again, the empty red arrows highlight the position of multilayer islands.

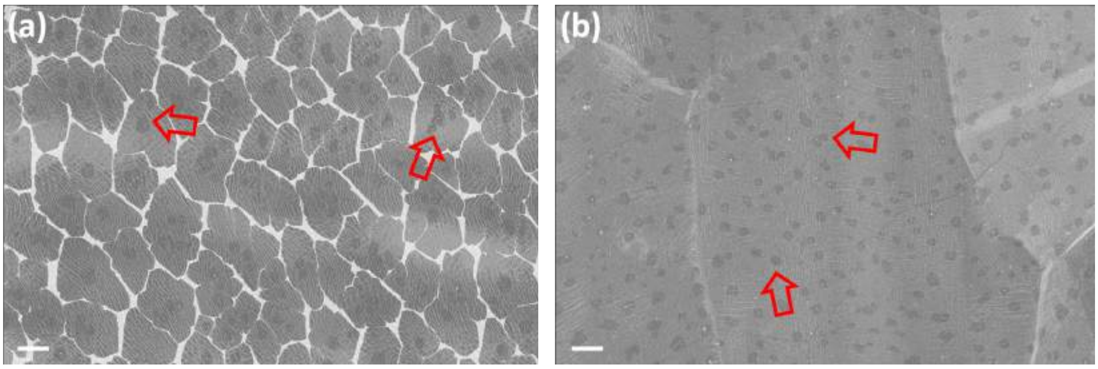

Figure 3.1 SEM images of as-grown graphene on copper. (a) In order to highlight the graphene domains and substrate, the growth was stopped just before the layer closing of graphene. (b) Complete coverage of graphene over the entire copper surface. Scale bars are 3 µm. The empty red arrows mark the multilayer islands.

Figure 3.2 shows typical optical images and the Raman maps of CVD-grown graphene transferred to SiO_2/Si wafer as outlined in Chapter 2 under section 2.2. As mentioned in Chapter 1, monolayer graphene absorbs 2.3% across the visible spectrum. This makes the absorbance-based optical microscope observation very difficult. Nevertheless, under reflective illumination, high-contrast optical imaging of graphene has been demonstrated by interference-based techniques [70, 139], but only on dielectric-coated silicon wafers, where the thickness of the dielectrics (e.g., 300 nm SiO_2) and the illuminating wavelength need to be optimised [71]. In fact, it was on such substrates that graphene was first observed in 2004 using an optical microscope under reflective illumination.

Based on this fact, the first characterisation step is typically optical microscope imaging to determine whether single layers are present, their positions on the substrate and sizes. Optical microscopy is an indispensable quality control tool for manufacturing graphene since it can provide immediate feedback to improve synthesis and processing strategies.

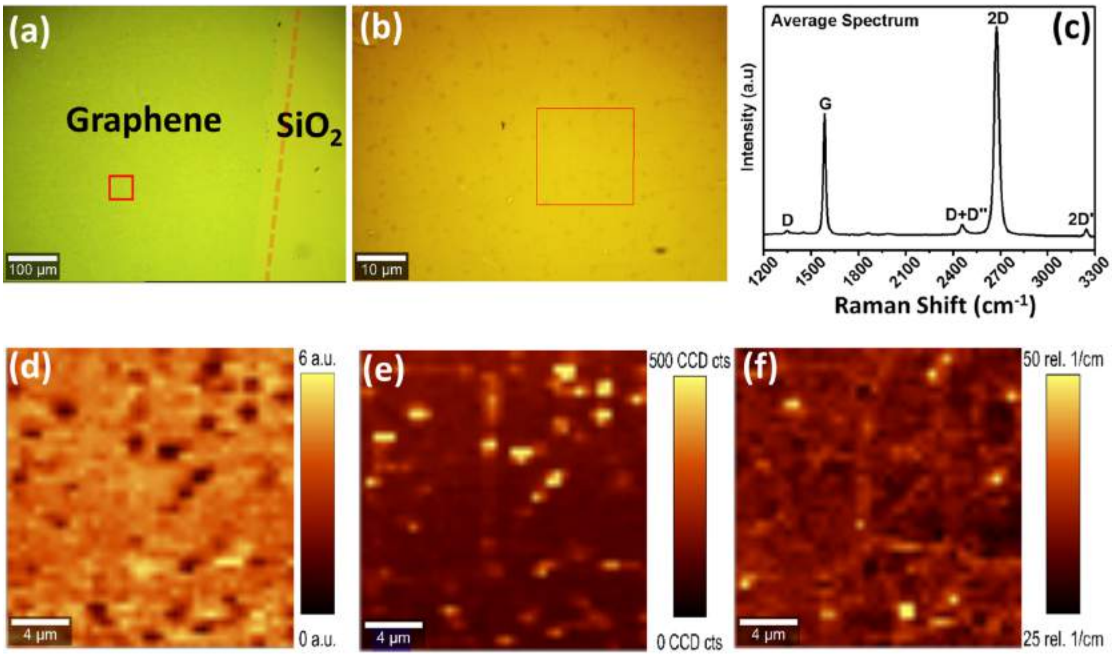

Figure 3.2 High-quality large-area monolayer graphene confirmed by scanning Raman spectroscoppy. (a) Low-magnification optical image. The dashed red line is a guide to the eye, distinguishing the graphene/substrate interface. The red box shows where the measurement was done. (b) High-magnification optical image, highlighting the high quality of graphene sheet. The red box marks the scanned area. (c) Average spectrum of the scanned area in (b). (d) 2D:G ratio map, indicating presence of a continuous monolayer graphene. (d) 2D band FWHM map, further confirming of monolayer graphene. (e) D:G ratio map, highlighting the low density of defects in the graphene film. The bright yellow spots correspond to multilayer graphene islands.

Availing from this property of graphene, optical imaging was first performed on the samples transferred 300 nm SiO_2/Si wafer (Figure 3.2 (a) & (b)). One can clearly see in Figure 3.2 (a), a continuous and clean graphene coverage, over hundreds of micrometres. Image (b) further shows that even at micrometre range, graphene is of high quality, with excellent cleanliness.

Raman spectroscopy reveals a wealth of information about graphene as discussed in Chapter 1. Figure 3.2 (c) represents the average Raman spectrum, generated by averaging 10000 spectra taken over the area shown by red box in image (b). The spectrum perfectly matches with that of monolayer graphene. Figure 3.2 (d) shows the 2D:G ratio map of the scanned area (marked with red solid box in (b)). As mentioned in Chapter 1 under section 1.6.2.1, the intensity of 2D peak in monolayer graphene is roughly four times than that of the G peak. Considering the colour scale bar of the map, it is clear that the graphene sheets is mainly monolayer. The scattered dark spots, correspond to multilayer islands, commonly seen in CVD-grown graphene on copper. Image (e) shows the sum of G band map, indicating presence of a continuous graphene sheet.

The bright spots in this map, correspond to the multilayer islands that appeared dark in the 2D:G ratio map (see Chapter 1, section 1.6.2.1). Finally, Figure 3.2 (f) shows the 2D band FWHM map, with bright spot being related to multilayer islands. In Chapter 5, the origin of these multilayer islands is discussed, and an effective method is presented to suppress their formation.

3.2 Graphene as TEM Support

So far we have described the impact of TEM on the graphene research; here we are going to look at it the opposite way. Being the thinnest material, made from a light element, crystalline and highly conducting, graphene may also become the ideal sample support for electron microscopic studies of other objects. The mono-atomic membrane made of low atomic number carbon ensures a very low background for TEM imaging, while at the same time providing firm support to large particles due to its extraordinary strength. Additionally, its ability to withstand harsh chemical and physical environments can enable a variety of experiments using electron beams [140–143].

In line with this application theme, a process called Graphene Resist Interlacing Process (GRIP) [132] was developed in our group to produce carbon-graphene cloth-like mesh, which consists of large area suspended graphene sandwiched between fortified polymers. This all-carbon mesh, allows flexible and easy handling of suspended monolayer graphene. Briefly described, first an array of parallel lines is patterned on a nickel sacrificial substrate using photolitography. Then CVD-grown graphene sheet is transferred onto this structure and a second array of parallel lines is patterned now perpendicular to the first set of lines. The sample was then annealed for 3 hours at 300 °C for 3 hours to improve crosslinking of the patterned photoresist. Finally, the nickel sacrificial layer is etched off and the floating stack is transferred to standard 300 mesh lacey carbon grid for further analysis. These steps are shown shematically in Figure 3.3.

Imaging of nanocrystals smaller than 5 nm in diameter is very challenging. This is due to the fact that in this size range, crystals typically composed of ten or less number of lattice planes, providing very small contrast. In practice, the contrast from the amorphous carbon support film is often of the same order of magnitude (or even greater) than that derived from the nanocrystal. Therefore, to demonstrate the utility of the mesh as

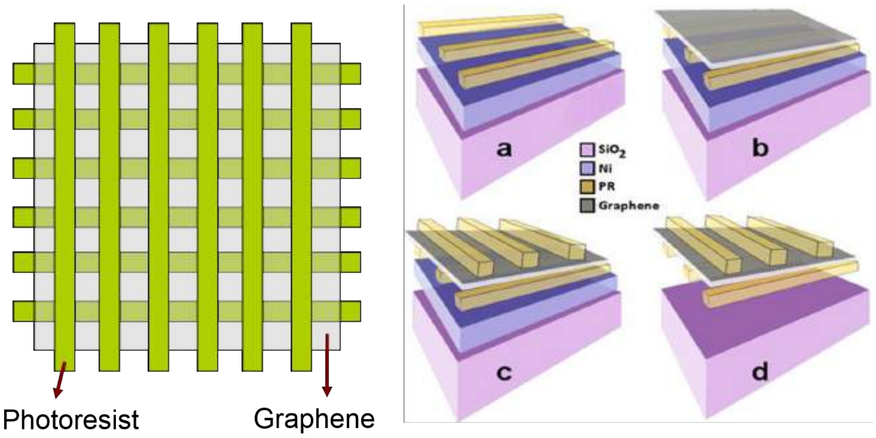

Figure 3.3 Schematic representation of the process steps involved in the GRIP.

a TEM support, TEM analysis was performed on CdSe and gold nanoparticles (NPs) deposited on standard commercially-available TEM supports and CVD-grown graphene.

Figure 3.4 shows the comparative TEM analysis of gold NPs on top of graphene and on lacey carbon TEM support.

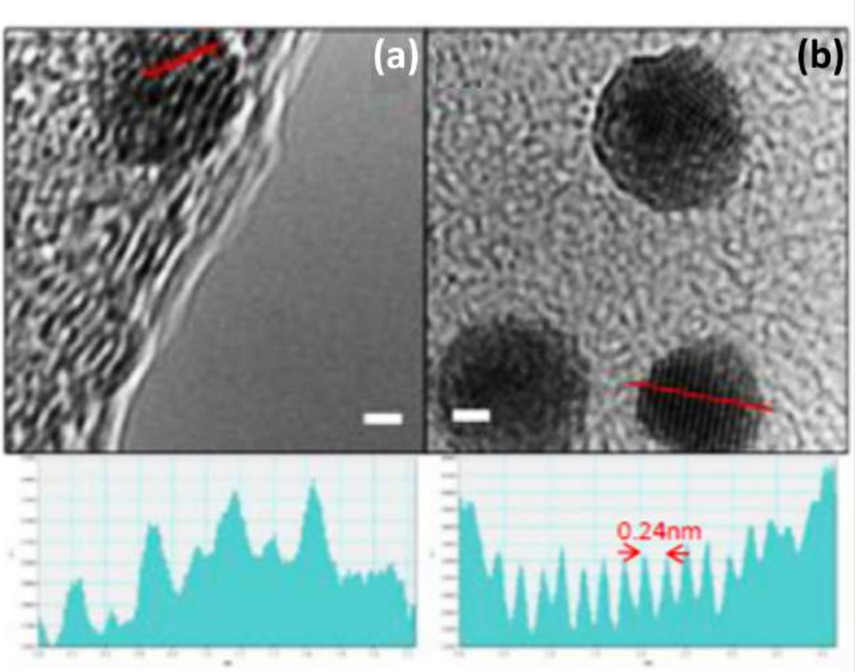

Figure 3.4 TEM images of gold NPs supported on lacey carbon (a) and graphene (b). The scale bars are 1 nm. The intensity profiles below are along the red lines in respective images. While the intensity profile in (a) shows only few merged peaks corresponding to atomic columns, the image on graphene in panel (b) contains several well-resolved peak with peak-to-peak distance of 0.24 nm, related to the gold (111) plane.

The gold NPs were deposited on the mesh by drop-casting a dispersion of NPs in methanol on top of the mesh. The contrast on lacey carbon support is very dim; with only a blurred outline visible (Figure 3.4 (a)). It should be noted that the images were taken on the very edge of the film. The graphene support on the other hand shows produces a clearly defined image (Figure 3.4 (b)). Lattice spacing is visible on both supports, although the contrast on graphene is much better, the peak to valley ratio on it being 3-4 times compared to that on lacey carbon as the intensity profiles show. The measured 0.24 nm inter-planar spacing correspond to the (111) plane of face-centred cubic gold [144].

To further demonstrate the utility of the mesh as a TEM support, CdSe NPs were imaged on conventional commercial lacey carbon grids (20–30 nm thick) and CVD-grown graphene support (<1 nm thick). CdSe NPs were chosen as they are somewhat harder to image than Au NPs. This is due to the fact that they are smaller and composed of atoms with lower atomic number than that of gold. As a result, one of the major limitations is the very high background from the amorphous carbon support.

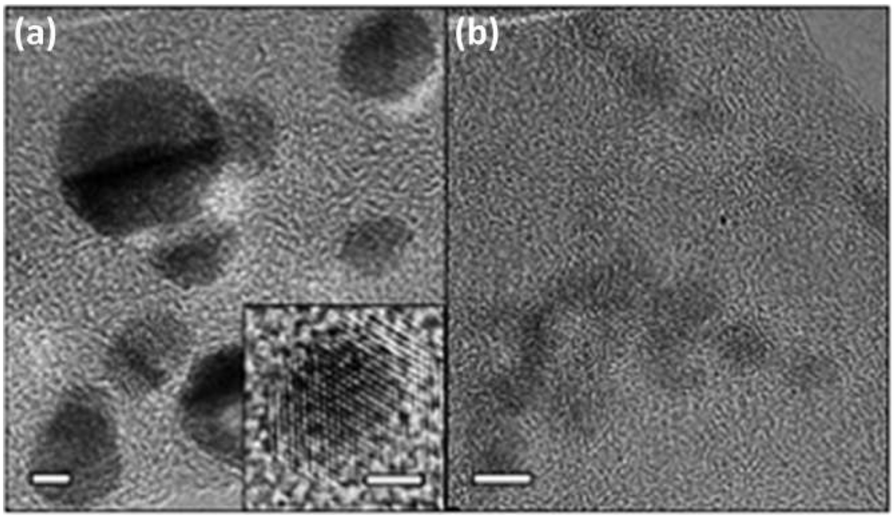

Figure 3.5 TEM images of CdSe NPs supported on (a) graphene and (b) lacey carbon. The inset in (a) shows a detail of one NPs. Scale bars are (a) 2 nm (both) and (b) 5 nm.

Figure 3.5 shows a comparison of typical HRTEM images of CdSe NPs <5 nm in diameter, acquired in comparable imaging conditions on lacey (a) and CVD-grown graphene (b). Particles imaged on graphene show a clear contrast improvement in comparison to the ones deposited on a much thicker lacey support. The inset of Figure 3.5 (a) shows a higher resolution image, revealing the fringes and individual atoms of nanocrystals. The measured interplanar spacing (0.43 nm) is consistent with (220) plane of CdSe crystal (Wurtzite lattice) which indicates we were able to resolve the atomic structure of the sample reasonably well.

3.3 Carbon-Silicon Interfaces

Pyrolytic carbon (PyC), is a disordered nanocrystalline graphitic material which can be formed through gas phase dehydrogenation (or pyrolysis) of hydrocarbons. This material exhibits good thermal and electrical conductivity as well as high durability. Moreover, PyC thin films are promising candidates for electrochemical and sensing applications. In our group, an adjustable process has been developed for CVD growth of thin films of PyC using acetylene as carbon feedstock [145]. The microstructure and crystallinity of the obtained CVD films are crucial to their physical and electrical properties. HRTEM imaging and FFT/SAED analyses are powerful tools in characterisation of CVD-grown PyC film. From the FFT/Diffraction Pattern, a parameter termed Orientation Angle (OA) can be extracted which is an indication of the microstructure of the film. The relationship between OA and the structure of the PyC is shown schematically in Figure 3.6.

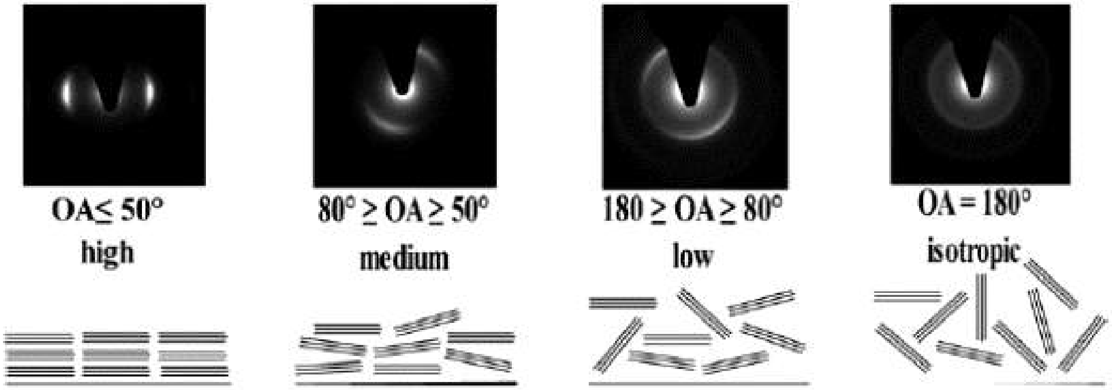

Figure 3.6 Schematic representation showing the relationship between the preferred orientation of pyrolytic carbon domains (texture) and the orientation angle (OA) obtained from SAED patterns. Adapted from [146].

On this basis, in order to gain insight into the CVD-grown film's microstructure, cross-sectional TEM sample was prepared using Focused Ion Beam (FIB) based technique (see [145] for more details). Electron microscopy allowed for both short and long range investigation of the PyC/SiO_2 interface and also gave information on the crystallinity of the PyC grown. An HRTEM image of the cross-sectional interface between PyC and the SiO_2 substrate is shown in Figure 3.7 (a). From this a laminar like deposition is observed. Further information is garnered from a higher magnification image as shown in Figure 3.7 (b). This allows for the crystallites to be directly viewed and suggests that domains are ≈ 2 nm in size. It appears that there is preferential stretching of crystallites perpendicular to the <001 >direction. The produced FFT of the HRTEM image in this region was produced and an OA of $\approx 46°$ was observed implying that the

PyC is highly textured. These observation confirmed that the designed CVD process, produces high-quality films.

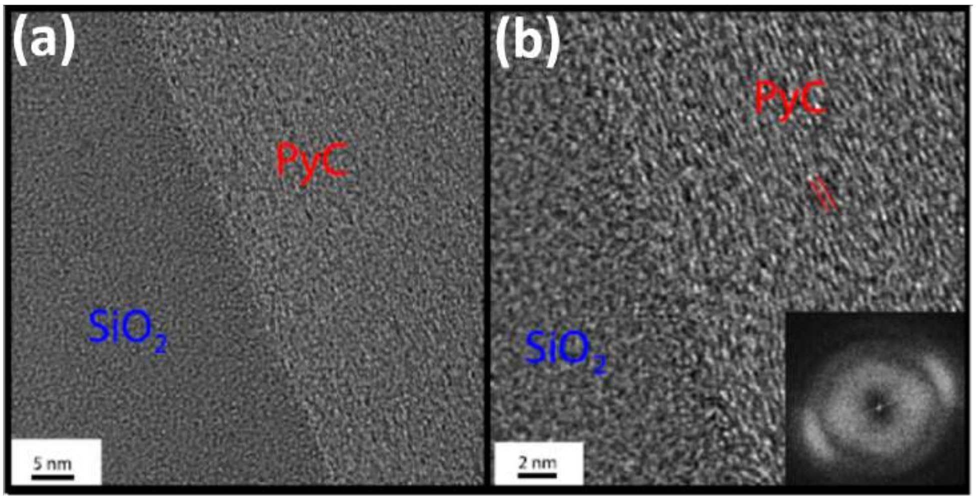

Figure 3.7 (a) Low mag HRTEM image of the interface between PyC and the SiO_2 substrate. (b) HRTEM image of the interface between PyC and the SiO_2 substrate. The nanoscale texture of the PyC domains is evident. Inset: FFT of HRTEM image, an orientation angle of 46° is observed.

Our group has also successfully demonstrated another novel application of nanocrystalline/amorphous graphitic films termed as carbon-silicon Schottky Barrier Diodes (SBDs) [147]. There are many factors that have a significant effect on the electrical properties of the diode such as the barrier height, the insulating layer between metal-semiconductor and the interface states. In addition, the stability of the interface between metal-semiconductor structures is one of the most critical conditions in diode performance. There were two types of carbon film, PyC and Pyrolysed Photoresist Film (PPF) which is made be annealing a photoresist at elevated temperatures ($\approx 1000\,^\circ C$). To this end, cross-sectional HRTEM technique was employed to investigate the interface between the silicon substrate and the carbon film.

Figure 3.8 shows HRTEM and corresponding FFT analyses of three layers present across the PyC-Si SBD sample. The gas phase deposited PyC film shows a slight laminar structure parallel to the underlying substrate. The OA was measured to be $\approx 57°$, corresponding to a medium-textured structure which is in agreement with HRTEM image. Moreover, the FFT of the interface layer suggests that it is amorphous. This could be attributed to the incomplete graphitisation at the interface or a remaining oxide layer on top of the substrate.

Figure 3.9 shows TEM analysis of the PPF-Si SBD. Corresponding FFT of different areas in HRTEM images have been produced which clearly show different type of structure present across the sample. From FFT of the topmost layer no discrete diffraction spots

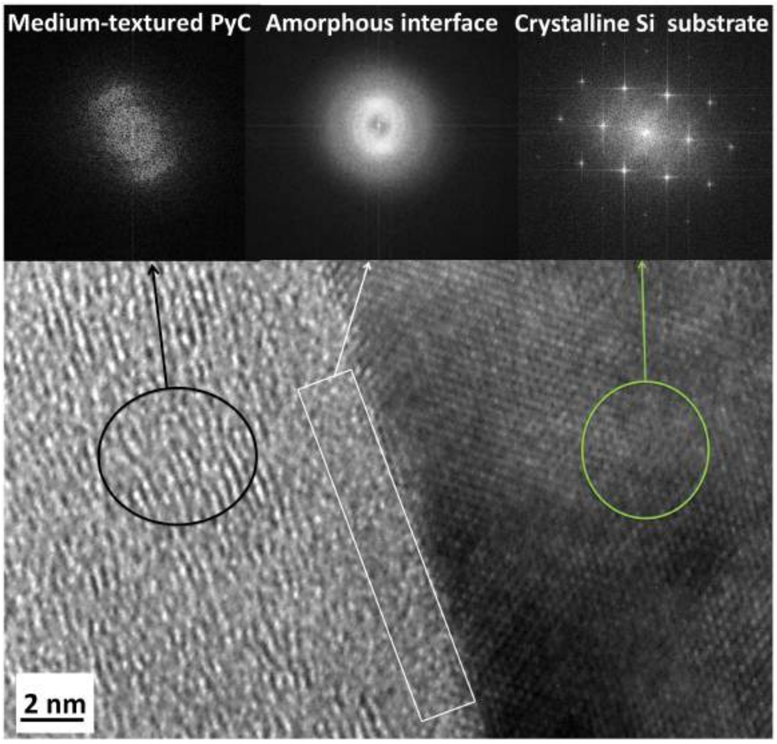

Figure 3.8 HRTEM images and their corresponding FFT across the interface, indicating presence of a thin amorphous interface between Si substrate and the medium-textured PyC film.

can be resolved and it consists of diffused concentrating rings, typical for a randomly arranged structure with very small structural units with short range ordering. Moreover, no recognizable interface different from the PPF itself is detected with typical FFT of an amorphous material. The spots in the FFT are from single crystal silicon substrate which is more evident by looking at the FFT of substrate typical for a sample exhibiting an undisturbed periodic structure over the whole area observed.

These results further indicates the invaluable role of TEM analysis in nanocarbon research.

3.4 Conclusions

The successful growth of large-area high-quality graphene has been demonstrated in this section. Furthermore, a modified reliable method for clean large-area transfer of CVD-grown graphene onto TEM support has been outlined. The capabilities of graphene as a perfect TEM support was shown. GRIP process has been described for making a carbon-graphene cloth-like mesh. It allows for flexible and easy handling of monolayer suspended graphene. The utility of the mesh has been shown as a superior TEM support for imaging NPs. The carbon-graphene composite structures might also be useful in more

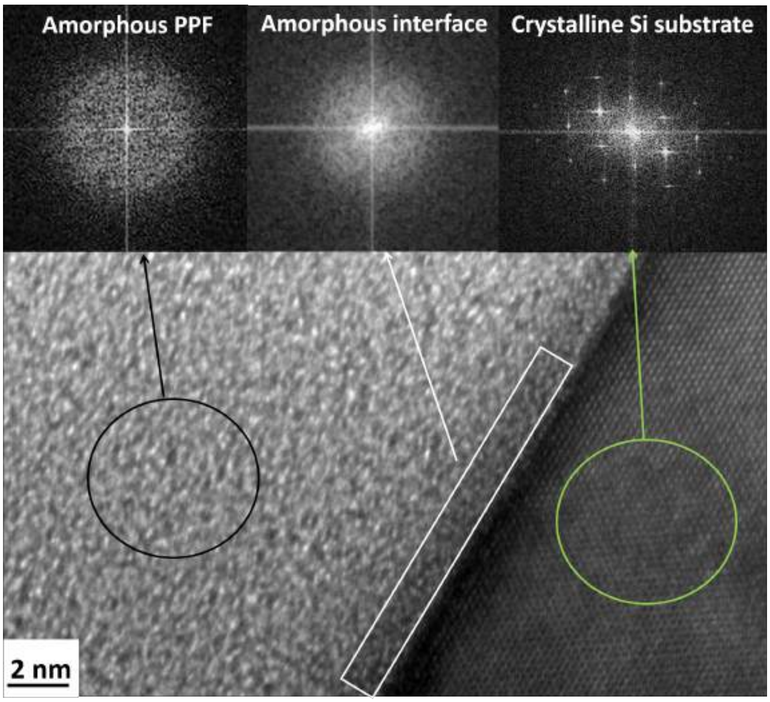

Figure 3.9 HRTEM and the corresponding FFT analyses of PPf/Si substrate, showing the presence of a very thin amorphous interface.

general applications, as GRIP provides a flexible platform to handle graphene with patternable carbon support. This may allow for fabrication of suspended graphene devices such as membranes or electrodes and multi-layered stacking of graphene. Furthermore, the importance of HRTEM/DP analyses in the characterisation of thin graphitic film interfaces were demonstrated by two practical examples.

Chapter 4

Modification of CVD of Graphene via Catalyst Optimisation

This chapter is adapted from the paper published in the journal *Carbon* [148]. CVD is a well-established method for growing high-quality large-area graphene, of great interest for applications such as electronics [24, 39, 55, 149]. The graphene, prepared by this technique is of high quality and can be further processed directly on the catalytic substrate (as-grown) or after transferring to a desired substrate. CVD growth of large-area monolayer graphene on transition metal substrates has been widely explored. However, despite the significant progress made in this field, there are still some bottlenecks to be overcome. One of the drawbacks of this technique is that the obtained graphene typically contains some bilayer/multilayer areas [150]. This can deteriorate the electronic and optical properties of graphene due to the lack of uniformity introduced by the multilayer islands [151, 152].

4.1 Suppression of Multilayer Graphene

To avoid the detrimental effects caused by the above-mentioned multilayer islands, one option is fine-tuning the parameters of the CVD process such that the bilayer/multilayer islands are suppressed. A reliable and efficient way is modification of the catalyst's surface which is outlined in this Chapter. Other approaches include implementing a post-growth H_2 etching step [152], pulsed-CVD as opposed to continuous dosing of carbon feedstock [151] and very recently via a tungsten foil placed inside a copper enclosure [153]. Using this approach, without needing to functionalise or carry out additional treatments, the electronic properties of as-grown graphene can be improved. During an inkjet-printing study for making Graphene Field Effect Transistors (GFETs) [154], we discovered that chromium affects the graphene growth process. In that work it was found that for high concentrations of the chromium-containing ink, the growth had been completely suppressed but interestingly, high quality graphene had been grown in the vicinity of that region. The approach of modifying the catalyst, has previously been reported by the a group in Cambridge, where they used of a Ni-Au alloy catalyst for low-temperature graphene growth [155]. In that work, they suggest that gold lowers the stability of surface carbon and thereby lowers the graphene nucleation density significantly. However, the resulting graphene grown by the aforementioned alloy catalyst was a combination of monolayer and bilayer/multilayer in contrast to copper that assures monolayer graphene with sparse secondary graphene islands on top. As discussed before, this is due the negligible solubility of carbon in copper, making the process as what is known as "self-limited" growth mechanism on copper. This means once the whole surface of copper catalyst is covered by fisr layer of graphene, the incoming carbon species have no longer access to catalyst surface and as a result, the growth stops. Chromium has been used in steel-making industry for many years in the mass production of high-strength and corrosion resistant stainless steel; and it is well-known that chromium partakes in strengthening of the materials by forming various carbides at the grain boundaries. Based on the previously-observed effect of chromium ink in and the above-mentioned role of chromium in stainless steel, it was it has been decided to investigate the effect of controlled introduction of chromium into the CVD process. The presence of chromium can be employed to manage the excess carbon during growth by sequestering it within carbides. Thus one can ensure that the growth will proceed without interruption. Various characterisation techniques namely optical microscopy, SEM, Raman spectroscopy imaging and X-ray photoelectron spectroscopy (XPS) were used. Additionally, carbon isotope labelling in conjunction with scanning Raman spectroscopy was employed to elucidate the CVD growth process in presence of chromium. We establish that chromium has a strong effect on multilayer formation and propose a mechanism for this effect.

4.2 Methodology

To enable assertive analysis of the evolution of growth under the effect of chromium, a thin layer of chromium was site-specifically sputter-deposited onto the copper foils through a shadow mask (see Figure 4.1, step 1-3). This way, there was always a clear border between the region on the copper surface in which the graphene growth had been altered by chromium. In order to investigate the evolution of graphene islands during the growth in the regions containing chromium, the isotope methane labelling method [156] together with various growth times was used. The growth step was performed,

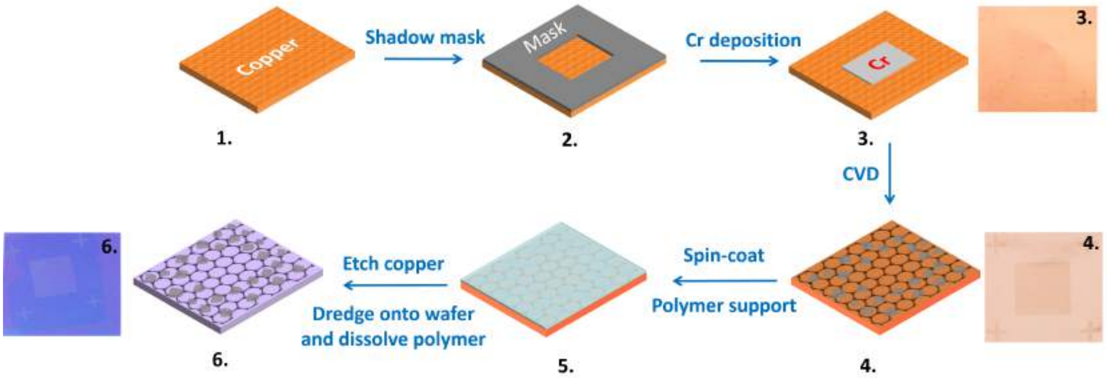

Figure 4.1 Schematic representation of sample preparation process flow.

by introducing a gas mixture 10 sccm of $^{12}CH_4$ or $^{13}CH_4$ and 5 sccm of H_2. Then a dribble flow of $^{12}CH_4$ and hydrogen was set and the furnace was force-cooled to room temperature via compressed air. The as-grown graphene was transferred to the desired substrate according to the procedure outlined in Chapter 2.

4.3 Chromium Influence on Closed Graphene Layers

Formation of multilayer islands is an undesirable element in the CVD of graphene, the common belief is that the multilayer islands grow by catalytic decomposition of active carbon radicals, CH_x $(0 \leq x \leq 3)$, between the first layer and copper substrate [156, 157]. A convenient way to suppress the formation of these multilayers is to bind them and hence eliminate them from any further involvement in the reactions taking place during the CVD process.

Transition metals and their compounds are widely used as catalysts; for example in hydrogenation and dehydrogenation, polymerisation [158, 159] and in the field of carbon research in carburisation reactions [160, 161]. Among transition metals, those with a large number of d-vacancies (chromium has 5 d-vacancies) decompose the carbon precursor and form stable carbides. Comparing the binding energies of various active carbon species on the copper surface during CVD [50] to those of different chromium carbides, indicates that nucleation of carbides is thermodynamically more favourable [162–165]. To this end, chromium was chosen for the purpose of multilayer suppression. In order to ascertain the behaviour of chromium in the actual experimental conditions of growth, two sets of samples were grown with the same experimental conditions: one with a thin layer of chromium on top of the copper substrate and the other with no chromium. Then, the as-grown samples were examined using high-resolution SEM and EDX analysis to determine the resulting growth qualities. Figure 4.2 shows the effect of

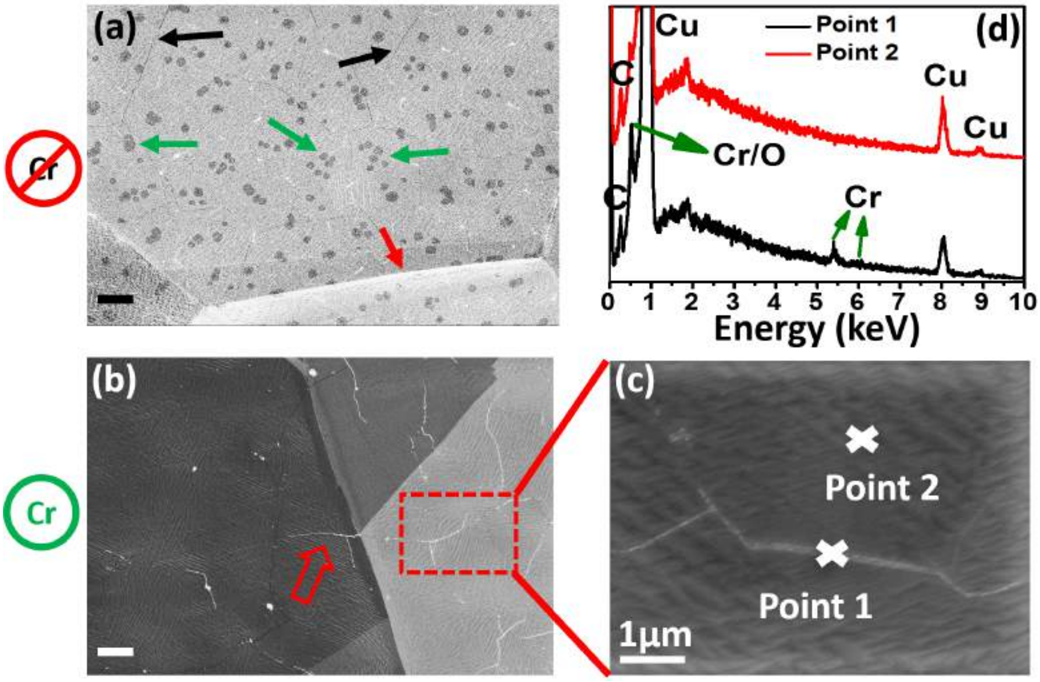

Figure 4.2 Effect of chromium on the suppression of multilayer (ML) islands. (a) SEM image of a sample with no Cr. The black, green and red arrows show wrinkles, monolayer graphene and Cu grain boundary (b) SEM image of a sample with 40 at. % chromium. The red arrow shows an individual nanowire-like feature. (c) Zoomed-in image of the dashed red box in (b) showing an area with an individual worm used for recording EDX. (d) EDX spectra taken from point 1 and 2 in image (c). (e) Growth model in the area with no chromium. (f) Growth model of chromium-containing area. The growth time was 10 min for both samples. Scale bars in (a) and (b) are 4 µm.

chromium on graphene growth. Figure 4.2(a) shows an SEM image of an area of normal growth that contains no chromium. The dark spots spread over the image are multilayer islands indicated by green arrows. On the bottom of the image, the brighter area is another copper grain whose boundary is marked with a red arrow and the black arrows show the wrinkles which are usually observed in CVD-grown graphene and attributed to thermal expansion mismatch between graphene and copper [166, 167]. Figure 4.2(b) depicts an area influenced by chromium. The first difference is that the dark spots seen in (a) are absent here, suggesting the formation of multilayers has been suppressed. However, we do see additional white features (marked with unfilled red arrow) that have a nanowire-like morphology. The nanowire features are shown in more detail in Figure 4.2 (c). Figure 4.2(d) shows the EDX spectra taken from an individual nanowire feature (point 1) and a reference point (point 2) indicated in Figure 4.2 (c). The EDX spectra shows that in addition to carbon and copper the nanowire feature also contains chromium, suggesting that some chromium carbide has formed in these regions. Based on these results, we propose that some carbon reacts with chromium forming a carbide during growth. Both chromium and carbon are largely insoluble in copper, suggesting

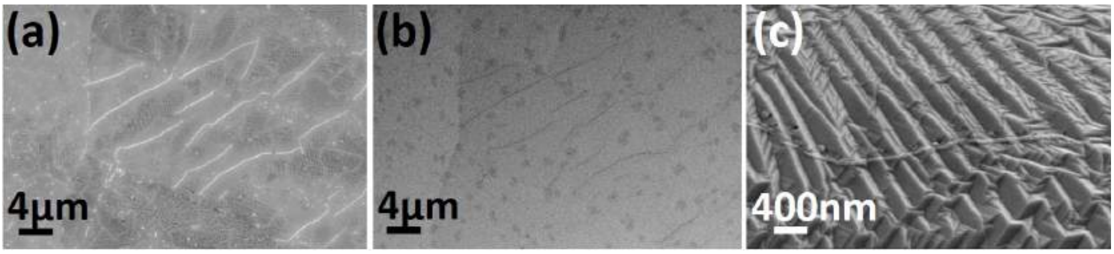

Figure 4.3 (a) SEM image of nanowire-like features taken with the InLens detector at 0.7 kV. (b) The same area shown in (a) but taken by EsB detector; and (c) SEM image of an individual nanowire-like feature.

that they will exist almost completely as surface species. More detailed morphological and compositional analyses of the nanowire feature are presented in Figure 4.3.

SEM images of the same nanowires were recorded with an InLens detector, shown in Figure 4.3 (a), and an EsB detector which is shown in Figure 4.3 (b). By means of the EsB detector, a clear compositional contrast of the surface can be afforded. This is due to the special design of this detector which enables exclusive detection of low-loss backscattered electrons which carry compositional information of the sample surface. The major benefit of this detector is that imaging can be done at very low voltages, which offers both minimal beam-induced damage for sensitive samples like graphene, as well as ensuring surface detection sensitivity and compositional contrast from the outermost layers of the sample. Since the backscattering cross-section dramatically drops for lighter elements, lighter elements appear darker in the images taken by this detector. To this end, we can ascertain that the dark contrast of the features in Figure 4.3 (b) suggests that the nanowires are made of elements with lower atomic number than that of the copper matrix ($_6$C, $_{24}$Cr, $_{29}$Cu). It should be noted that the reason why the nanowires appear brighter in (a) is that, since the InLens detector is basically a SE detector which is positioned inside the microscope column, then contrast enhancement due to the *edge effect* [168], observed in standard SE images, occurs here as well. It should also be noted that dark spots in image (b) (and less pronounced in image (a)) are indeed multilayer islands. Since multilayer islands are located underneath the monolayer graphene [157], the probability of generated signal electrons that can reach the detectors are less than that of monolayer graphene; hence they appear darker in the electron micrograph. This effect is more prominent in EsB image comparing to the InLens image, as basically the cross-section of BSEs is smaller than SEs.

Additionally, XPS measurements on copper foil before and after growth are presented in Figure 4.4 (performed by Dr. N. C. Berner in our group), indicating there was no chromium detectable on the surface after growth. XPS was performed to investigate the chemical composition (see the table in Figure 4.4(a)) of the catalyst surface before and

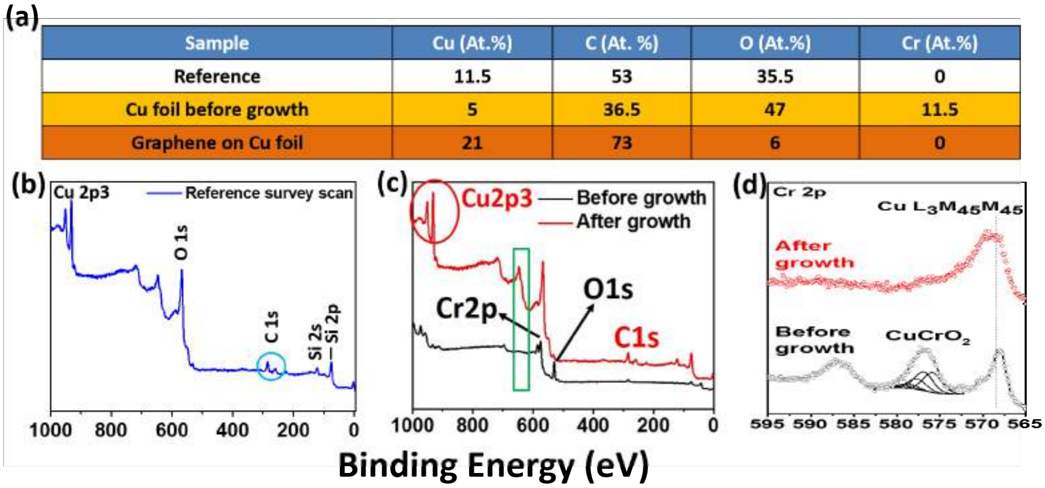

(a)

Sample	Cu (At.%)	C (At. %)	O (At.%)	Cr (At.%)
Reference	11.5	53	35.5	0
Cu foil before growth	5	36.5	47	11.5
Graphene on Cu foil	21	73	6	0

Figure 4.4 XPS analysis of the chemical composition of the catalyst surface. (a) Table of chemical composition of the three samples. (b) The survey scan of the reference sample. (c) The survey scans of the sample before and after growth. (c) Cr-2p core-level spectra of the sample before and graphene growth.

after growth. Three samples were measured by XPS: a blank copper foil (labelled as reference sample in Figure 4.4), a copper foil with a 1 nm thick chromium layer deposited on top through a shadow mask (labelled as before growth), and the same sample after the growth of graphene (labelled as after growth). The spectrum in (a) shows the survey scan of the reference sample containing a number of prominent peaks related to carbon, copper and oxygen which are attributed to the copper foil and hydrocarbon contaminants formed during sample preparation and handling. The survey scan spectra from the sample before (black spectrum) and after the graphene growth (red spectrum) are shown in Figure 4.4(b). The presence of chromium before growth (11.5 at.% for a nominal thickness of 1 nm chromium) was established by XPS. The greater oxygen content in comparison to the reference sample is attributed to the formation of chromium oxide. The spectrum of the sample after growth contains important information about the surface species. Firstly, the free chromium signal is absent (574.3 eV); this could be due to the diffusion of chromium into the copper substrate as well as reaction of chromium with carbon to form carbides. The reason why the chromium carbide signal has not been detected is ascribed to the surface abundance of carbides being lower than the required 5% detection limit of the XPS machine. The high content of carbon in the as-grown sample (73 at.%) is related to the graphene. Figure 4.4(d) shows the Cr 2p core-level spectra. The spectrum of the sample before growth (marked with the vertical grey line), contains three major peaks. The first peak appears at ≈ 568.5 eV and is related to the metallic copper Cu^0 [169]. The second peak emerges at ≈ 575.7 eV and the third peak occurs at ≈ 586.8 eV. The deconvolution of the Cr 2p core-level spectrum, following the fitting parameters established by Allen *et al.* [170], suggests that the chromium present on the copper surface before growth is in the form of $CuCrO_2$ ($\approx$ 576 eV). The as-grown sample however, shows only the Cu^0 peak and there is no signal from chromium-related compounds. All these results again confirm that there was chromium present on the catalyst surface before the growth and it either reacted with carbon or diffused into the copper substrate.

4.4 Time-Resolved Graphene Growth

In this work graphene has been synthesised at 1035 °C (as this is known to effectively form high-quality graphene monolayers [39, 171]) and hence the growth is *diffusion-controlled* [172]. In this regime the growth rate is nearly independent of the temperature and is instead governed by the mass transport of reactants at the substrate surface. For diffusion-limited growth we may use Fick's laws such that:

$$J = -\mathrm{D}\nabla\phi \tag{4.1}$$

$$\frac{\partial\phi}{\partial t} = \mathrm{D}\Delta\phi \tag{4.2}$$

Where J is the diffusion flux vector, D is the diffusion coefficient, ϕ is the amount of substance per unit volume and t is the time. These differential equations highlight the importance of coverage as a function of time.

Figure 4.5 shows the SEM images and the rate versus time plots; highlighting the effect of growth time. Other factors involved in the CVD process such as partial pressure of methane and hydrogen and total pressure of the CVD reactor were kept unchanged to simplify the interpretation of the results.

Image (a) and (b) show the SEM image of the surface after 30s growth. Both areas show dendritic growth morphology which is expected for a diffusion-controlled growth [173]. However, graphene domains in the chromium-containing area display a more serrated type of dendrite. Observation of irregular morphologies with other number of lobes has been ascribed to the disturbed diffusion path of surface carbon [174]. Image (c) and (d) depict the SEM images of graphene growth after 120s, with and without the influence of chromium. Once again, the dark spots in (c) correspond to multilayer islands and the light background is monolayer graphene. In contrast the white areas in (d) are the substrate. This indicates that the influence of chromium has led to less complete growth. The coverage of monolayer graphene for surfaces with and without chromium has been determined from SEM images and reported in Figure 4.5 in which both areas were fitted with sigmoidal-type models.This was chosen as the sigmoid functions are typically used

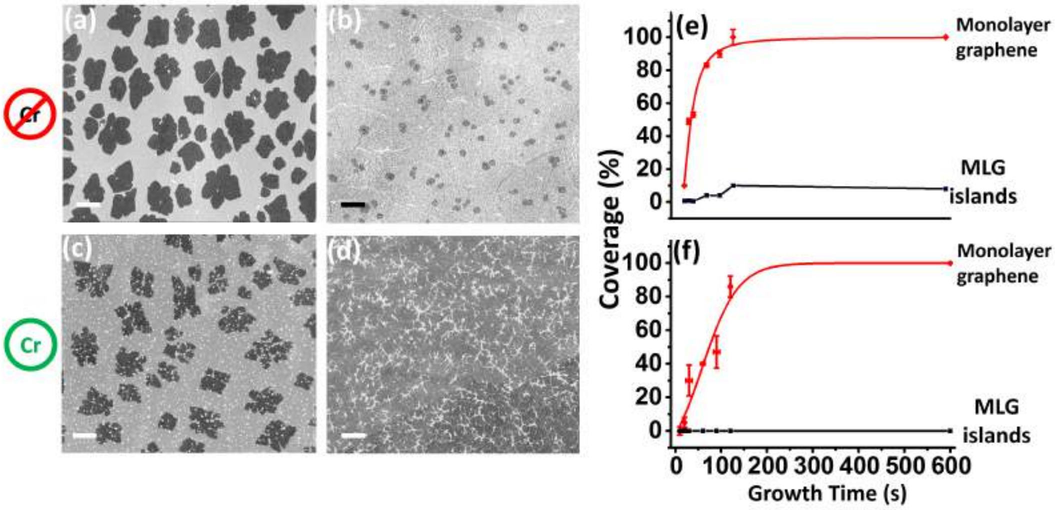

Figure 4.5 Effect of growth time. (a) SEM image of area with no chromium after 30 s growth. (b) No chromium area after 120 s. Note the complete coverage and the dark spots which are multilayers. (c) Area with chromium after 30 s. (d) Area with chromium after 120 s. (e) & (f) Monolayer coverage vs. time from the surfaces shown in a-d. All scale bars are $4\,\mu m$.

for modelling the systems that exhibit evolution from small beginnings (resembling the nucleation stage during graphene growth) and reach a saturation after a period of time (full coverage after the time t). The slope of the fitted curve in the areas with chromium was extracted to be 0.7 and that of area without chromium to be 1.9, meaning at the same experimental conditions the growth at the area with chromium was nearly times slower. In addition to a more serrated growth morphology the surface is covered with white spots. Measurement of the white spots with EDX (see Figure 4.6) indicates that they are chromium-related and most likely are chromium carbide.

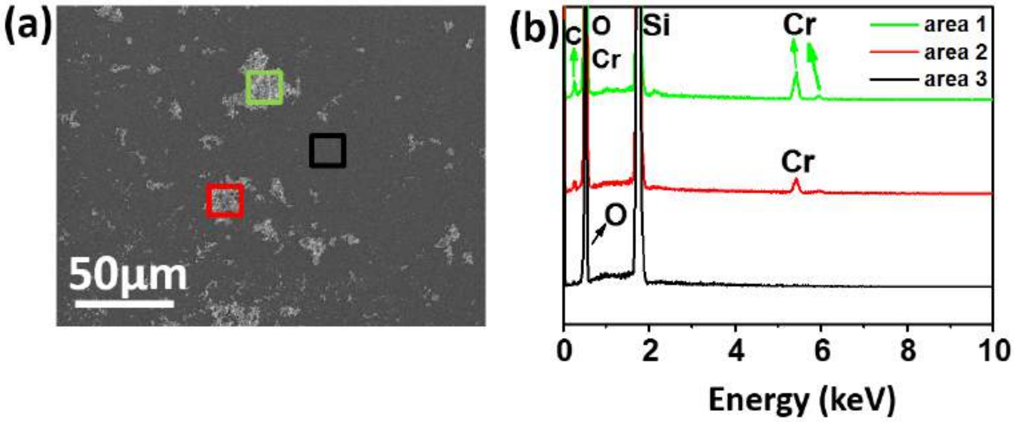

Figure 4.6 EDX analysis of white spots over the surface of the substrate.

In order to quantify the evolution of multilayer islands in the chromium-free and chromium-containing regions, a comprehensive statistical analysis of the size distribution of the multilayer islands was carried out. For this purpose, tens of SEM images from a number of samples with full graphene coverage and the same growth conditions were examined; and an overall area of $\approx 0.02\ \text{mm}^2$ was analysed to construct the statistics. This was achieved by first accurately calibrating the SEM images of both regions and subsequently counting the multilayer islands via ImageJ software. Then, standard statistical parameters were extracted and histograms of the size distribution of multilayer islands were plotted. The statistical analysis provides concrete proof of the effect of chromium on multilayer island suppression. Firstly, the total number of multilayer islands within the chromium-free regions was more than three times than that of chromium-containing regions. This clearly shows the suppression of multilayers under the effect of chromium. Secondly, the smaller average size of the multilayer islands in the chromium-containing regions (see the table below) strongly suggests that those islands which formed during the growth, could not grow as large as their counterparts in the chromium-free regions within the same time span. This suggests a delayed growth in the chromium-containing regions. The results of this analysis are presented in Figure 4.7.

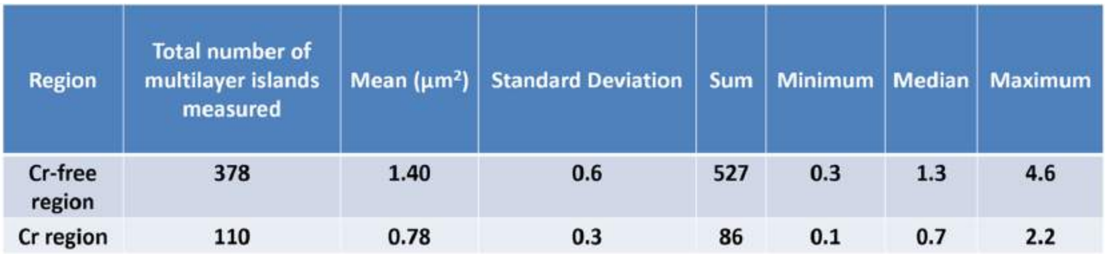

Region	Total number of multilayer islands measured	Mean (µm²)	Standard Deviation	Sum	Minimum	Median	Maximum
Cr-free region	378	1.40	0.6	527	0.3	1.3	4.6
Cr region	110	0.78	0.3	86	0.1	0.7	2.2

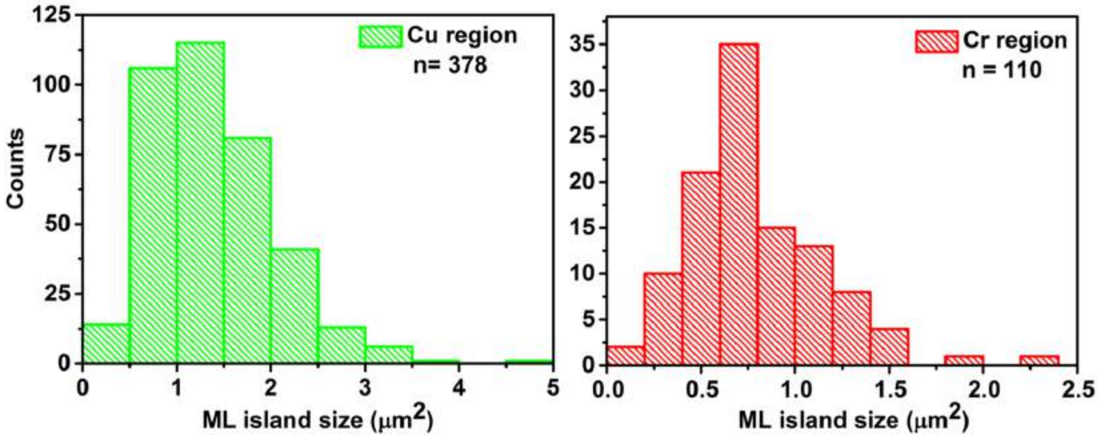

Figure 4.7 Statistical analysis of multilayer islands size distribution.

4.5 Isotope Labelling

As discussed in chapter 1, isotope composition has been employed as a way to study crystal growth mechanisms. The application of isotope labelling to graphene was pioneered by Li *et al.* [124] in an experiment where the evolution of graphene growth on nickel and copper substrates was investigated by varying the isotopic abundance of the carbon feedstock. The method is based on the atomic mass difference between ^{13}C isotope and abundant isotope ^{12}C. The isotope effect manifests itself as a down-shift in the position of graphene Raman peaks. The 2D band can be down-shifted by about 100 cm^{-1} and the G band by 60 cm^{-1} . This is a strong effect and can be used to label different regions as the graphene grows, and thereby, track the progression of the growth. In this work, we employed a sequential dosing approach for isotope labelling of graphene in order to examine the evolution of multilayer islands during growth.

Figure 4.9 (a) and (b) show optical micrographs of graphene formed by first dosing ^{13}CH$_4$ for 90s, then ^{12}CH$_4$ for an additional 90s. This cycle time was chosen such that the early and later stages of graphene growth are captured with distinct isotope labelling (see Figure 4.8). The objective of this labelling was to determine when during growth, multilayer formation occurs.

The graphene transfer to SiO$_2$ in this experiment, allows for easier optical identification of multilayer islands and eliminates the fluorescent background observed for Raman spectroscopy on copper. To analyse the growth, scanning Raman spectroscopy was performed in 25×25 μm^2 regions at a number of different locations within the sample. The spectroscopic information was used to create maps of the summed intensity for the 2D bands as obtained for ^{13}C (2573 cm^{-1}, width = 38 cm^{-1}) and ^{12}C (2680 cm^{-1}, width = 30 cm^{-1}) feedstock. The broader width of 2D peak for ^{13}C is attributed to those multilayer islands that are incommensurate (see Chapter 1 under 1.6.2.1). The small difference between the linewidth of two regions is due to the fact that first not all of the multilayers are incommensurate and that the multilayers are only small part of the whole surface area. Figure 4.9 (b) and (d) show the isotopic 2D intensity maps, for a region without chromium. In these figures we can immediately see that the multilayer graphene regions (marked with yellow arrows) are labelled by the ^{13}C carbon indicating that they form since the early stages of the growth. In addition, one can see that the ^{12}C regions are small and filamentary indicating that over 90% of graphene growth occurs within 90 seconds and the final stages of growth consist of a stitching together of the individually nucleated graphene grains. It is also important to discuss the role of interplay between the copper substrate and the carbon species on the surface in terms of the growth of graphene layers. The formation of a C−Cu−C bridging metal structures has been discussed previously when considering coalescence of carbon atoms and clusters

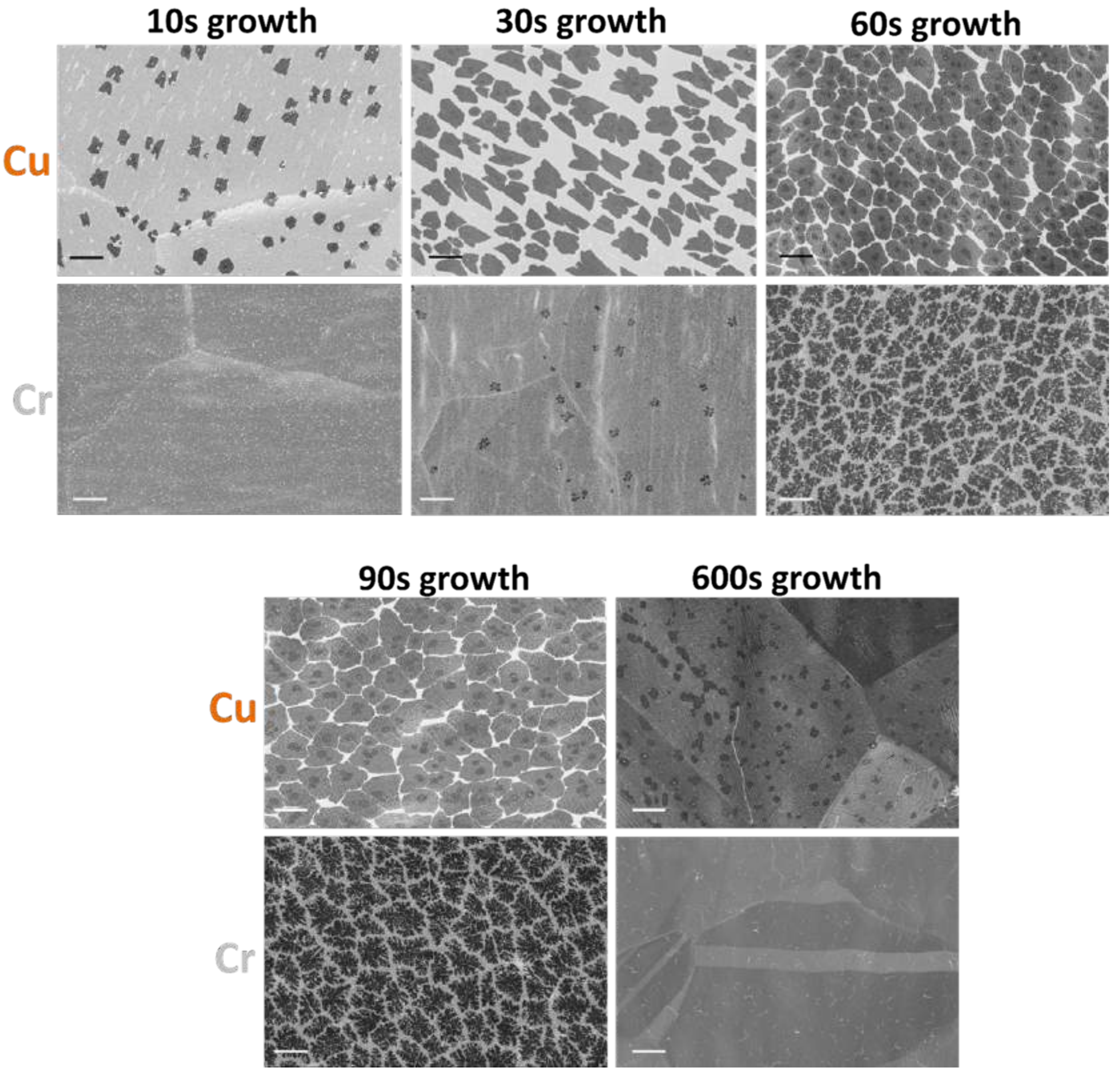

Figure 4.8 investigation of the onset time for the appearance of seeds and layer closing of graphene. The scale bars are 4 μm.

[175]. Such Cu−C coupling has also been observed experimentally during CVD growth of graphene on copper [176]. On this basis, it is suggested that the multilayer islands are in fact the initial graphene nucleation seeds.

Figure 4.9 (d) shows corresponding maps for a region with growth that has been influenced by chromium. The most notable feature in the optical image is that there are no multilayer islands. Raman 2D and G band maps reveal more information about the fate of multilayer islands in this region. Firstly, the absence of high intensity spots corresponding to multilayer graphene is a clear indication of their suppression. Additionally, in the G band map, the contribution of ^{12}C is greater than that of the chromium-free region which corroborates our previous finding that chromium inhibits the growth rate of graphene. Finally, the regions in which ^{13}C is detectable describe a rougher, more

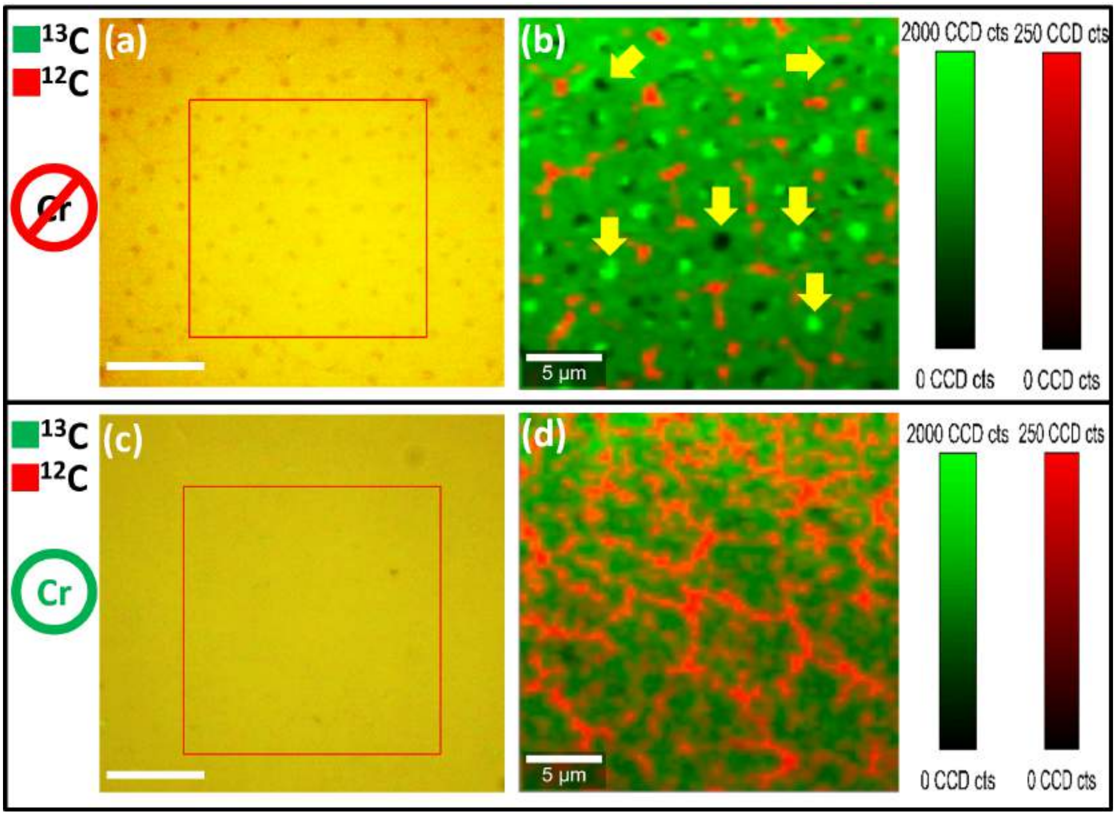

Figure 4.9 Isotope labelling study of multilayer islands. (a, c) Optical micrographs of the Cr-free and Cr-containing regions, respectively. The scale bars are $10\,\mu\mathrm{m}$. (b, d) $2D_{12}+2D_{13}$ combined maps of the area without and with chromium, respectively.

ornate geometry as would be expected by the strongly serrated growth mode identified earlier.

4.6 Proposed Mechanism

We may now put forward a tentative growth model for graphene in the presence of chromium and how it is able to suppress the nucleation of multilayer growth. Away from the influence of chromium, initial nucleation of graphene growth comes in the form of simultaneous monolayer and bilayer growth. This is possible because catalysed carbon species are easily able to reach the upper and lower layer growth fronts. As the size of the graphene regions increase the catalysed species are less able to reach the growth front of both layers of graphene and the bilayer formation slows and halts.

In the case of chromium influenced growth, the carbon species form chromium carbide. The isolated chromium carbide islands reduce the diffusive mobility of the carbon species on the surface and hence suppress the formation of second-layer growth. In addition, this leads to a slower graphene layer formation and a rough disordered growth front

[157]. The chromium carbide islands inhibit diffusion of other carbon species but at the growth temperature they, themselves are mobile and the gradual ripening of graphene domains during growth forces the carbide islands to group together at the growth front, finally coalescing into nanowire features at the final stage of graphene layer closing. So, the formation of chromium carbide species limits the diffusive mobility of the carbon growth species which means multilayer graphene islands cannot nucleate.

4.7 Conclusions

It is known that, in CVD growth of graphene on copper, despite the high quality of graphene obtained, some scattered multilayer graphene islands are also found. These multilayer are detrimental to the uniformity of graphene. In this Chapter, a viable method for obtaining an exclusively monolayer graphene has been presented. This method is based on the surface modification of the copper catalyst by a deposited thin film of chromium. It has been demonstrated via several characterisation techniques that, indeed this method ensures complete suppression of multilayer graphene islands, normally observed with CVD grown graphene. Using the isotope labelling method of graphene together with other methods, a reaction mechanism for the effect of chromium on the growth has been suggested.

The main advantage of this approach over the other proposed multilayer suppression methods is that, it can be utilised in the growth of graphene on other transition metals, as the basic mechanism responsible for this effect is the chromium mediated formation of carbides. With the ever-increasing demand for large-area high-quality monolayer graphene, this method can pave the way to a reliable entirely monolayer growth of graphene on transition metal substrates.

Chapter 5

Study of Isotope-enriched CVD Graphene

5.1 Isotope-enriched Graphene

This chapter is adapted from the paper [2] which is in preparation. Isotope-enriched methane was first used in graphene research by Li and co-workers [124] to study the evolution of graphene during CVD on nickel and copper substrates. Carbon atoms can be marked in this way based on the fact that there is a down-shift in the peak position of Raman spectrum of isotope graphene. Nevertheless, isotopes can impact the bond strength of the host structure and therefore potentially the mechanical properties. This is known as kinetic isotope effect [177]. To the best of our knowledge, atomic resolution study of isotope graphene has not been reported yet; which would be useful to understand the microstructural changes in the graphene lattice upon incorporation of ^{13}C atoms. In this chapter, the AC-TEM study of isotopically-labelled CVD graphene sheets is discussed. We show that graphene sheets grown from isotope-enriched methane show high electron-beam damage resistance; even at high probe currents and prolonged exposure times. Furthermore, clear alteration of the edges of this type of graphene sheet is discussed.

5.2 Methodology

There are different possibilities to introduce the two isotopes (using the $^{12}CH_4$ and $^{13}CH_4$ gases) into the CVD reactor: (a) Alternating dosing of each isotope into the reaction chamber over a certain period of time. (b) Pre-mixing the two gases with desired ratios before introducing to the furnace and, (c) separate independent two full growths for each isotope. For this study, graphene was grown using 99% pure $^{13}CH_4$ (Sigma Aldrich) feedstock, and by CVD technique as outlined in Chapter 2.

After transferring as-grown graphene onto Si/SiO$_2$ wafer, scanning Raman spectroscopy was employed to verify the isotopic composition of produced graphene films. The theoretical background of such technique is outlined in Chapter 1. The results are shown in Figure 5.1.

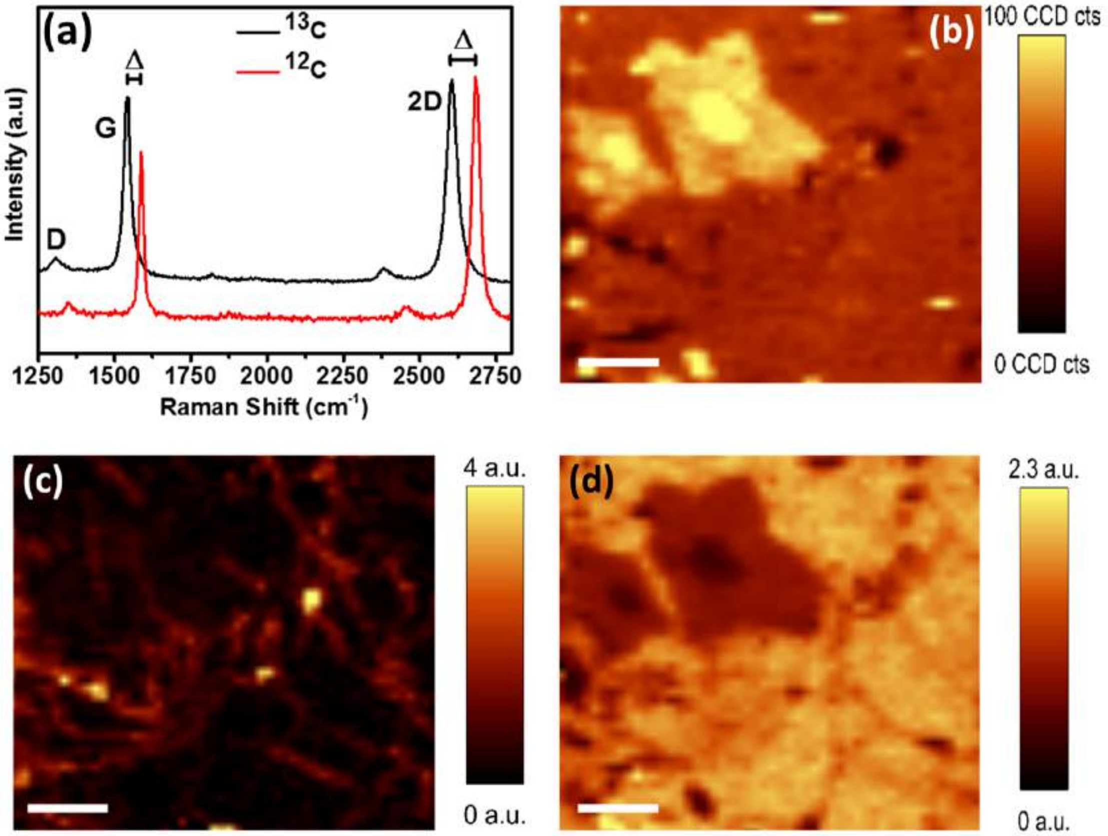

Figure 5.1 (a) Average spectrum of the scanned area shown in the optical micrograph (inset). The numbers are showing the 2D, G and D peaks expected for 100 % isotope graphene. The FWHM of 2D band was measured 48 cm^{-1}. (b) G band intensity map (c) D: G ratio map indicating low density of defects (d) 2D: G ratio map showing high quality graphene. All the scale bars are 3 µm.

Firstly, the expected down-shifts in the position of Raman bands (≈ 100 cm^{-1} for 2D peak and ≈ 60 cm^{-1} for G peak), shown by Δ, matches with the purity of isotope methane gas source used for the growth. Furthermore, the D:G peak intensity ratio map together with 2D:G ratio map are indicative of a high quality graphene with low density of defects grown by isotope methane [68, 178–180]. It is also notable the high intensity areas in G band intensity map and their dark corresponding areas in 2D: G ratio map, show multilayer islands normally seen in CVD growth [124].

To assess the quality of graphene samples on TEM grids prior to TEM studies, scanning electron microscopy and Raman spectroscopy of suspended graphene on TEM grid were employed. SEM images were taken in several places over the entire TEM grid and a typical image is shown in Figure 5.2.

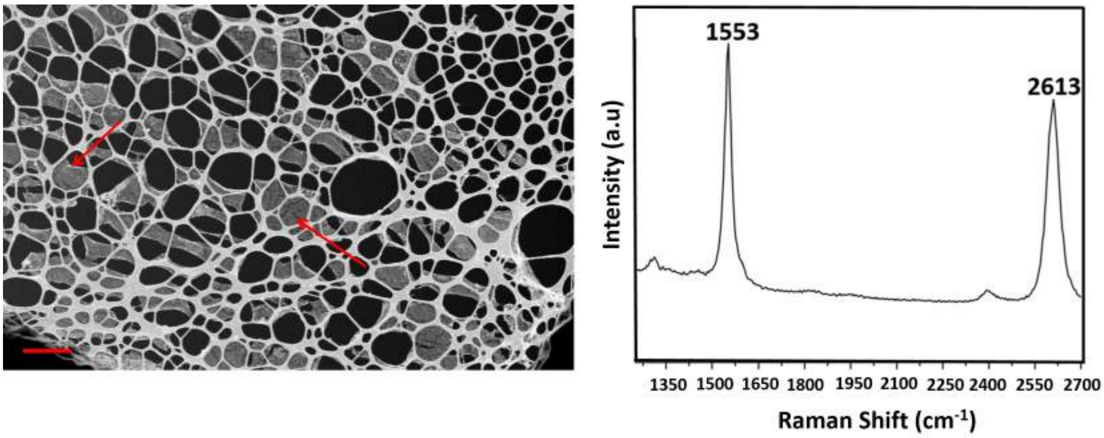

Figure 5.2 SEM inspection of transferred isotope graphene on TEM grid. (Right) Typical Raman spectrum of the graphene membranes marked with red arrows in the SEM image.

The SEM inspection suggests successful large area transfer of graphene sheet onto the grid. Typical Raman spectrum taken from a number of graphene membranes proves that they are indeed isotope graphene. The 13 cm^{-1} up-shift from the peak positions expected for the isotope sample is attributed to the chemical doping during transfer process [178, 181, 182]. Effectively, metal ions from the catalyst etchant or airborne contamination can act as dopant for graphene, moving the Fermi energy away from the Dirac point depending on the nature of the dopant. As mentioned in Chapter 1 under 1.6.2.3, this results in blueshift of the G and 2D peak.

To ensure the cleanliness of samples meets the minimum requirements for aberration-corrected TEM study, they were inspected by a standard FEI Titan in STEM mode whose results are shown in Figure 5.3.

As apparent in the STEM low magnification images (Figure 5.3 (a) and (b)), the coverage of graphene film on TEM grid is remarkable which ensures that there will be more than enough areas within the grid to be looked at higher resolutions. Furthermore, the high resolution TEM image (Figure 5.3 (c)) in conjunction with the typical diffraction pattern observed in the sample, indicate the graphene is of high quality and well-ordered which had been confirmed before by Raman. Despite all these qualities, the mobile general hydrocarbon contaminations were present (marked with red arrows in Figure 5.3 (a) and (c)) which are generally caused by sample box and sample exposure to air. This can be removed by high vacuum baking at elevated temperatures. To this end,

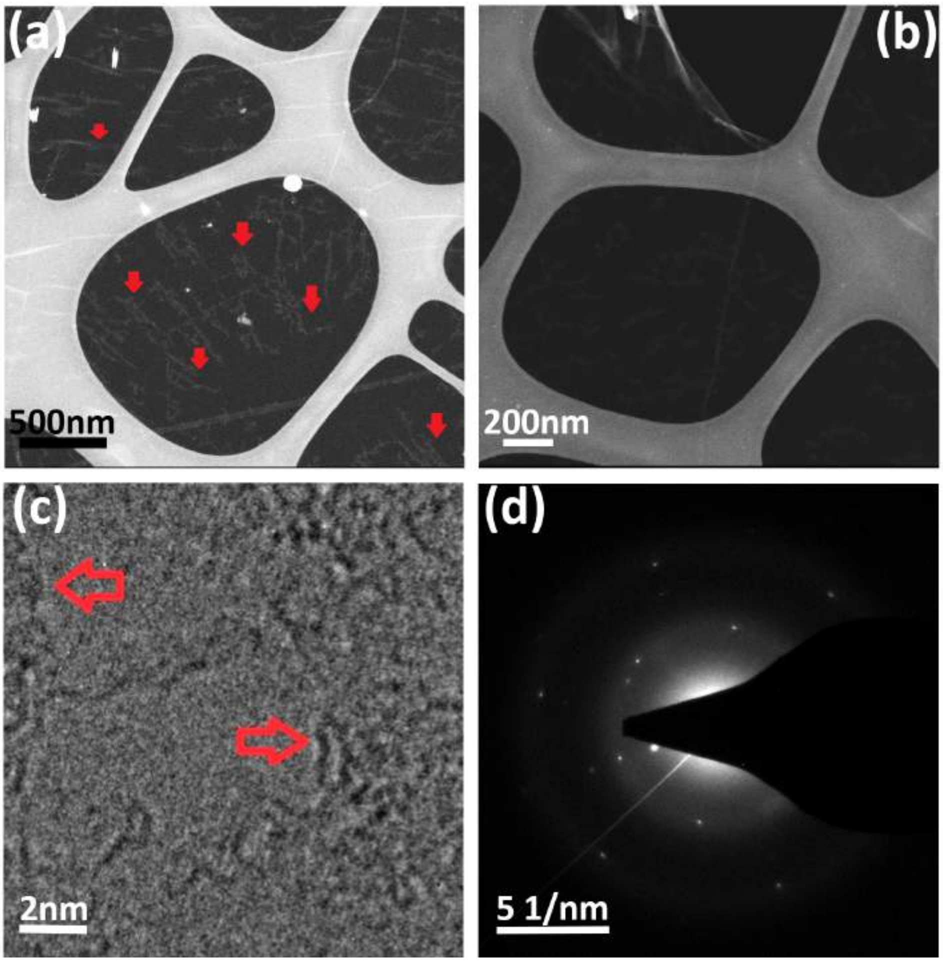

Figure 5.3 S/TEM inspection of transferred isotope graphene. (a,b) STEM low magnification images showing large area coverage. The red arrows in (a) show mark the contaminations. (c) HRTEM of the same sample. Again red arrows mark the hydrocarbon-based contaminations.

the samples were baked for several hours in a dedicated vacuum oven with the base pressure of 1.33×10^{-7} Pa at 200 °C just before loading into the aberration-corrected machine or else baked inside the TEM column. This was done to minimise the amount of hydrocarbon-based contamination caused by handling and other ambient exposure effects.

All the AC-TEM images were recorded by Dr. J. Kim using the Oxford JEOL JEM-2200MCO aberration-corrected and monochromated TEM [183, 184], at 80 kV acceleration voltage to reduce the knock-on damage of graphene caused by electron beam. The collected data was corrected using CEOS [64] hexapole correctors. The raw TEM images were further processed by E. Rezvani, using the customised filters available for Digital Micrograph software, for easier identification of graphene edge features as well as lattice alteration within the graphene sheet. All the TEM images presented were smoothed out by removing the high-frequency information. This was carried out by means of a low-pass 3rd order Butterworth filter with a radius of 64 pixels. Then the resulting image was processed with a band-pass filter with a structure filtering range of 3-1000 pixels. This was done to level out the frequency cut-off. Despite the fact the image processing enabled easier identification of Klein Edges (KLs) (carbon atoms protruding from a zigzag edge), but also caused some subtle features due to the Fourier filtered noise in the vacuum region next to the specimen.

5.3 Isotope-enriched Graphene: Bonding Properties

5.3.1 Bond Length

The electron beam-induced damage is a well-known phenomenon that adversely affects the samples being studied by TEM [185, 186]. This issue is particularly prevalent with fragile carbon nanostructures, especially in the case of HRTEM of 2D films [92, 187]. Knock-on damage, or sputtering of atoms, by the electron beam has been widely discussed in the literature. Meyer and co-workers [188] showed in a meticulous study that the knock-on damage, which is caused by the impact of probing electrons with the nucleus of the sample, differs from other radiation damage mechanisms such as chemical etching. They experimentally obtained a knock-on threshold of 80 kilovolt for monolayer defect free graphene. The same work reported that isotope-enriched graphene was more robust and showed lower radiation damage. We first discuss in simple terms the origin of the higher robustness of isotope and graphene and then will present some experimental evidence.

We begin by considering what actually dictates the inherent strength of a material; the strength of chemical bonds between the building units of that material. In order to analyse the chemical bonds, understanding potential energy surfaces and hence internuclear potential energy is important. In quantum chemistry, the harmonic oscillator approximation is used to explain the vibrations of a diatomic system and the quantum mechanics solution for it, help to formalise the potential energy. The heavier the molecule or atom, the lower the frequency of vibration and the smaller the zero point energy. Conversely, lighter molecules or atoms have a greater frequency of vibration and a higher zero point energy. This results in different bond dissociation energies meaning heavier isotopes have higher dissociation energies. This effect is called *kinetic isotope effect (KIE)* which makes the isotopic labelling a very powerful method in physical organic chemistry to determine the reaction pathways and other bonding characteristics [189]. Nonetheless, based on the potential energy curves, heavier isotopes should have shorter bond length. In contrast to this principle, in this work experimental evidence of significant bond lengthening in isotope graphene samples was observed compared to normal graphene. Figure 5.4 represents the $^{13}C-^{13}C$ bond length analysis in the bulk lattice of graphene.

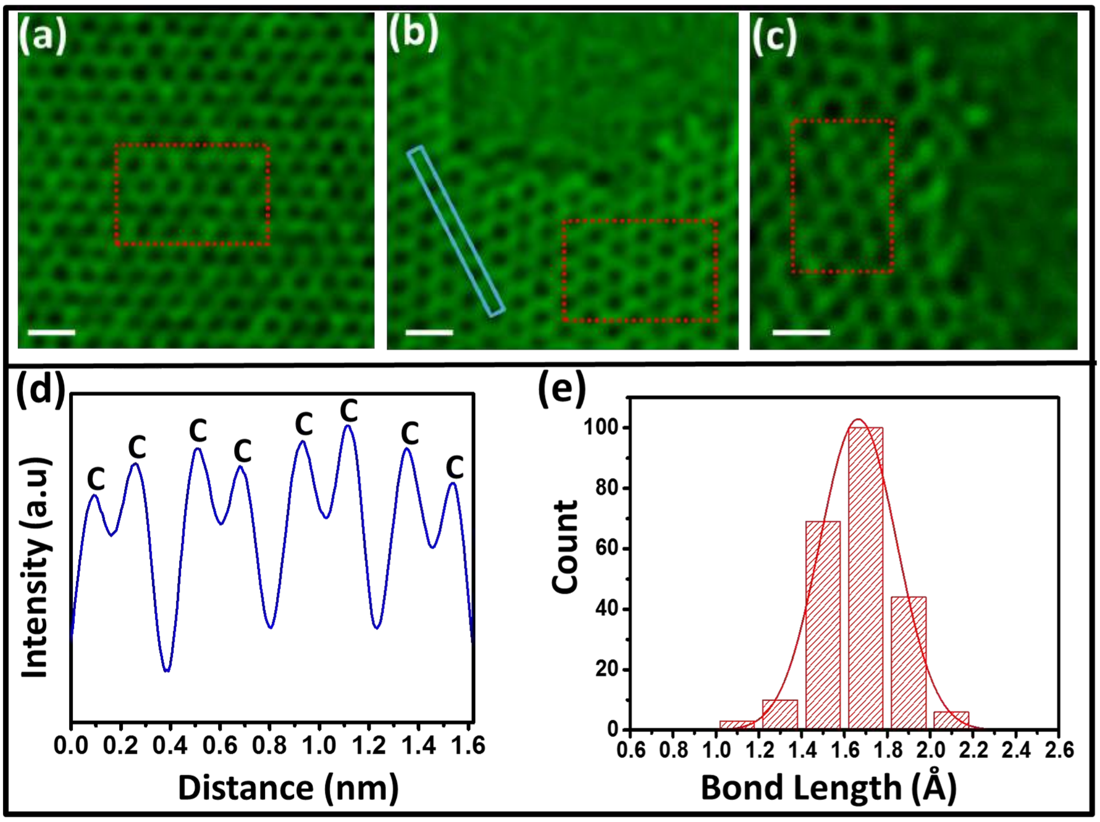

Figure 5.4 Bond length analysis (a), (b) AC-TEM images of the isotope graphene with Klein edges (c) typical intensity profile taken from a box around the Klein edge (e.g. black box in (b)). (d) Distribution of bond length in the inland of graphene landscape (e.g. red boxes in (a) and (b)). (e) Distribution of bond length of Klein edges measured in a number of samples (e.g. green boxes in (a) and (b)). Scale bars are 5 Å.

To ensure the reliability of bond length measurements, after calibration of scale bars produced by the microscope, a comprehensive analysis was carried out on over 300 pairs of atoms. This was implemented by measuring the intensity profile of each pair of atoms across 5 sets of samples and several locations within each set of samples were examined. Figure 5.4 (a-c) show representative AC-HRTEM images of isotope graphene recorded from three different samples. A typical intensity profile (taken from the blue dotted box in Figure 5.4(b)) is shown in Figure 5.4(d). A histogram was constructed to analyse the distribution of bond length in the bulk-lattice of isotope graphene (Figure 5.4(e)). The areas marked by red in Figure 5.4 (a), (b) & (c) denote areas in which bond lengths were analysed. Then the histogram in Figure 5.4 (d) was fitted with a Gaussian curve and the peak position was taken as the average bond length value for $^{13}C-^{13}C$ bonds. The bond length was measured 166 pm ± 7.34 pm (measurement standard error plus a pixel size) for the isotope graphene which is considerably longer than that of “normal” graphene (142 pm). The $^{13}C-^{13}C$ bond length has been measured with accuracy of ±2 pm using Solid State Nuclear Magnetic Resonance (SSNMR) spectroscopy and values up to 400 pm have been reported [190]. Our results from AC-TEM assisted bond length measurements are in agreement with the trend of literature SSNMR values. Having presented all these data, it should also be noted that such long bond lengths question the established theories, which in itself could be exciting but also has to be treated very carefully to avoid any mistake. Therefore, further confirmation of this observed bond lengthening is crucial.

It should also be pointed out that the monolayer isotope graphene specimens were often observed over an unprecedented time space typically up to about half an hour prior to beam-induced damage at 0.2 nA spread over a circle of diameter of approximately 60 nm when the beam was diverged to a small 1.0 nm probe. This is a further empirical evidence of the excellent bond strength in isotope-enriched graphene. However, this could also be caused by a change in the cross-section of secondary electrons, leading to a more “gentle” beam. This scenario requires further investigation.

5.3.2 Abundant Klein Edges

Among all types of periodic edge configurations reported for graphene, the armchair edges are the most thermodynamically stable [92, 191, 192]. Accordingly, they are the most frequently observed. However, under the effect electron beam irradiation, the system moves away from thermodynamic equilibrium and, as a result, the probability of observing other less stable edge types such as zigzag edges increases. KLs are another type of thermodynamically unstable edges and are traditionally described as an (array of) extra carbon atom bonded to a graphene edge carbon atom in a zigzag edge and which contributes to the delocalised π-bonding network [98]. KL structures in the TEM environment stem from sputtering that creates a transient state before they are sputtered into another zigzag edge after several seconds. The Extended Klein edges (EKLs) were only recently observed experimentally [94] using monochromated AC-TEM; highly stable KLs had, however, been theoretically predicted before [98]. The abundant observation o KLs in isotope graphene is ascribed to the KIE that affects the bond strength in isotopically-labelled compounds. Isotope-enriched graphene is not an exception and upon replacing the ^{12}C with ^{13}C atoms during CVD growth, stronger bonds form within graphene lattice between isotope carbon atoms. This results in a net improvement of the lattice strength, emerging as for instance stabilisation of otherwise transient unstable edge states such as KLs.

This observation was not limited to one sample and a few places. Contrarily, these edge states were detected in several isotope-enriched graphene samples and in many locations in each sample.. Figure 5.5 shows two out of several EKLs observed in this study.

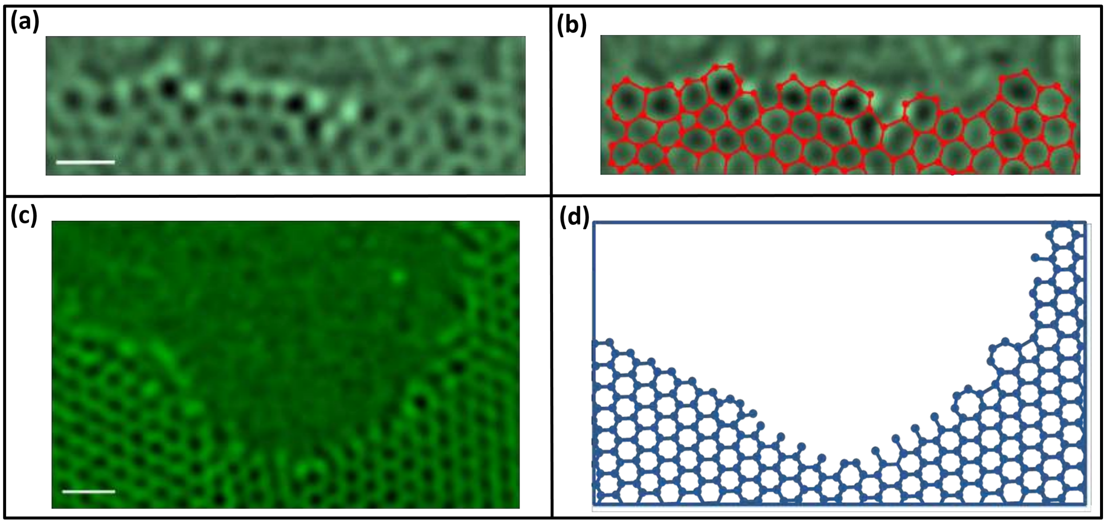

Figure 5.5 Abundant observation of extended Klein edges. (a, b) Representative AC-TEM images of EKLs in two different samples. (c, d) the corresponding schematic models of images in image (a) & (b). (e) Histogram of bond length distribution of KLs among all the samples studied in this work.

Figure 5.5 (a) & (b) represent EKLs in two different samples. Figure 5.5 (c) & (d) are the associated schematic model of the edge configuration and the histogram in (e) shows the KLs bond length distribution across all 5 samples.

The average bond of KLs was obtained via the same method described in the previous section and the same value (166 pm ± 27pm). Even though the average bond length of KLs was nearly equal to the bond length of bulk lattice of graphene, a higher degree of variation of bond length was observed. This is attributed to the nature of the KLs being singlet or doublet. Such configurations are shown in Figure 5.6. Once again, we ascribe the presence of such EKLs and EKLDs to the stronger bonds that are more resilient to the E-beam sputtering. More experimental evidence of abundant KLs is shown in Figure 5.7.

5.3.3 Unusual Heavily Deformed Edge

If we look back at Figure 5.5 (a) & (b), we can clearly see that the edge rings are neither normal 6-membered rings nor 5-7 ring pattern which is seen in some restructured edges [191, 192]. While these uncommon ring patterns have been predicted to be seen at grain boundaries [193, 194], but has not been reported experimentally in literature. It is

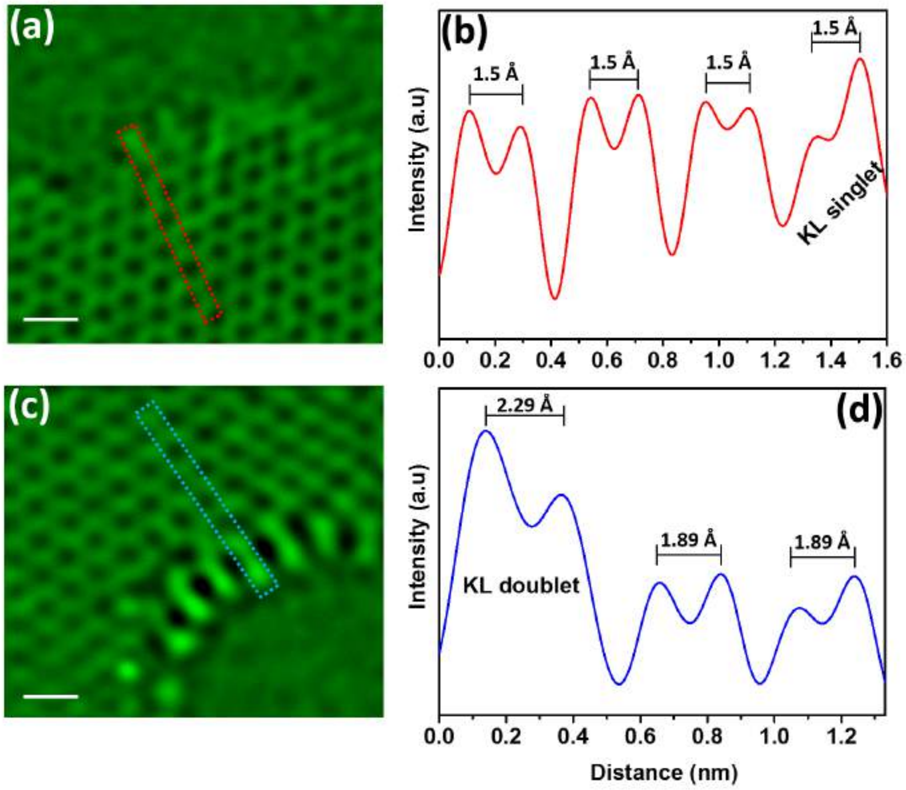

Figure 5.6 Klein edge singlets and doublets. (a) AC-TEM image of a KL singlet and (b) the intensity profile along the red box in image (a), highlighting the equal bond lengths. (c) AC-TEM image of a KL doublets and (d) the corresponding intensity profile taken from the blue box in image (c). Scale bars are 0.5 nm.

suggested that this edge reformation could be related again to different bonding characteristics of isotope graphene comparing to normal graphene, allowing bond modification during TEM observation.

5.4 Conclusions

In this Chapter, I showed that isotope graphene has different bonding properties comparing to normal graphene. Kinetic isotope effect, a well-known phenomenon that influences the bond strength in a material, was experimentally observed in isotope-enriched CVD-grown graphene. Despite these experimental proofs, further confirmation of such unusual bond lengthening is necessary as it it opposes established principles in quantum chemistry.

It is however postulated that the KIE manifests itself as longer bond length in isotope-enriched graphene. Furthermore, it was found that majority of the KLs have the same bond length as they are single KLs. The average bond length of KLDs was $\approx 33\%$

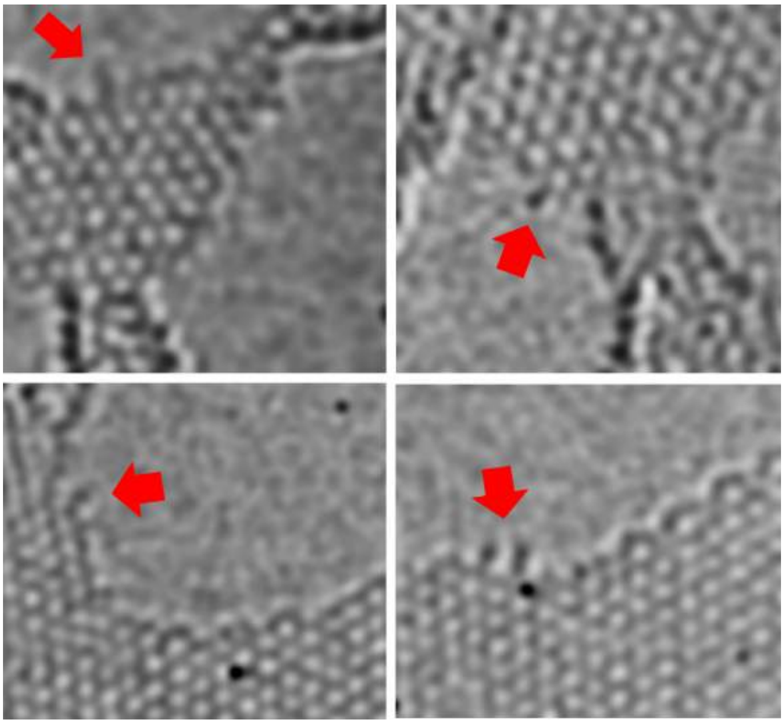

Figure 5.7 Abundant observation of KLs across various sets of isotope graphene samples. It should be noted that the images are raw TEM data.

longer than that of single KLs. Significant abundance of Klein edges of various types was another unusual observation in isotope graphene. Such abundant observation of KLs of any type is quite uncommon in “normal” graphene.

In order to theoretically explain three main experimental observations, longer bond length of isotope-enriched graphene and abundant observation of uncommon edge features, simulations are being run in collaboration with Oxford image analysis group. Density-functional theory (DFT) calculations of the ground-state of the bulk will be able to confirm the observed structural stability and reproduce the measured ${}^{13}\mathrm{C}-{}^{13}\mathrm{C}$ bond length reported here of 166 pm. Concerning the presence and frequency of the various Klein edges, DFT calculations can be done to test the stability and energetics of this behaviour as has been done previously for edges in ${}^{12}\mathrm{C}$ graphene [94, 195]. Comparison of these results should confirm that the stronger bonds in ${}^{13}\mathrm{C}$ graphene lead to the interesting edge behaviour.

Chapter 6

Study of Plasma-Functionalised Graphene

HRTEM/EELS has been used successfully before to characterise various form of carbon materials such as soot [196, 197], carbon onions [198], DLC [199] and indeed for analysis of graphitic carbons as a subcategory of this family [200–203], to name a few. Graphene as the mother of the all sp^2-bonded nanocarbons, is no exception to this, therefore , HRTEM/EELS should be applicable to study the microstructural changes of graphene.

Based on this motivation, this Chapter deals with the TEM/EELS investigation of plasma-functionalised CVD graphene. First, we present an overview of the reasons behind the functionalisation of graphene, some potential applications of the resulting graphene, as well as some of the state-of-the-art methods to carry out the functionalisation process. The remote plasma-functionalisation and its particular characteristics are then introduced. Finally, a TEM/EELS-based characterisation protocol is proposed as an assessment tool, for graphitic materials after plasma treatment.

6.1 Functionalisation of Graphene

Despite its extraordinary properties, graphene is inherently a gapless material so it can not be immediately used for digital electronic applications. However, introduction of dopants has been proposed for applications such as nanoelectronics [204, 205] sensing and catalysis [206].

In particular, nitrogen dopants can act as electron donors in nitrogen-doped (N-doped) graphitic systems. N-doping of graphene is advantageous for high frequency semiconductor device applications [207] and this material is considered an excellent candidate for energy storage and solar cell applications [208–211]. Most recently, N-doped graphene has been reported to act as a catalyst in oxygen reduction reactions (ORR) which are crucial in energy conversion [212–214].

For chemical functionalisation there are several sub-categories of doping, namely surface doping and substitutional doping which can both give rise to either p-type or n-type electronic behaviour. Substitutional nitrogen doping of graphene has been reported by means of different techniques such as chemical vapour deposition [215], annealing under ammonia atmosphere [207], arc-discharge of graphite under pyridine/ammonia ambient [216], wet chemical routes [217] and nitrogen plasma treatment [218].

6.2 Remote-Plasma Functionalisation

In order to realise the above-mentioned applications of functionalised graphene, a process that provides precise control over the quality and surface chemistry of graphene is required. Plasma treatments allow for the introduction of controlled levels of functionalities onto surfaces without the need for wet chemical steps. This makes it a clean, green technique and compatible with industrial processes. Nevertheless, one of the drawbacks of the plasma-based functionalisation methods is that it causes unfavourable physical damages to the surface, creating perforations, holes or tears.

We have developed a downstream plasma doping technique [79] using a custom-built apparatus in which the samples are placed at a location remote from the plasma source (described in Chapter 2), thereby minimising the destructive effect of plasma species. Using this approach, an initial oxygen plasma treatment is performed on the pristine sample creating active sites for accommodating further functional groups. A subsequent plasma treatment is then carried out with a mixture of hydrogen and ammonia which simultaneously reduces and N-dopes the graphene. Elsewhere, a similar approach has been shown to simultaneously reduce and N-dope graphene oxide powder [78]. In spite of its crucial importance, details on the mechanism of incorporation of heteroatoms into graphene remain unclear. Figure 6.1 illustrates the process flow in the plasma treatment process and shows possible configurations of nitrogen in N-doped graphene.

In the following sections, we aim to picture the capabilities of HRTEM in conjunction with EELS, to obtaining more insight into the evolution of graphene lattice upon each plasma treatment step by our remote-plasma system.

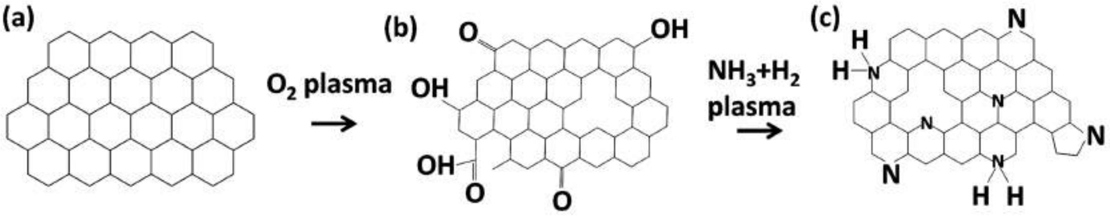

Figure 6.1 Schematic illustration of graphene lattice evolution upon plasma treatments (a) pristine graphene (b) oxygen-plasma treated graphene (c) H_2+NH_3 plasma treated graphene.

6.3 HRTEM/EELS in Graphitic Materials Research

While Raman spectroscopy is an excellent technique for characterisation of the crystalline nature of graphitic materials, it does not provide any chemical information about the sample such as the nature of dopants. HRTEM/EELS as a characterisation kit, being carried out with the same instrument, provide both imaging and compositional insights into the foreign atoms when properly set up. EELS is a powerful tool for characterising the extent of ordering in sp^2-bonded carbon systems. Interpretation of the definition, position and intensity of various features in the EEL spectrum, enables changes in the chemical states and crystalline structure [219–221] to be monitored. In particular, the appearance and definition of the features within the core loss region are excellent measures of the extent of ordering and graphitic character. Qualitative comparison of the carbon K-edge features provides an immediate measure of the extent of order and, as the sample gets more ordered, these features become more defined [220]. This stems from the fact that the more extensive the periodicity and symmetry between atomic positions, the higher the density of unoccupied states [222]. Before we discuss the case of plasma-functionalised graphene, a brief overview of some the topics related to EELS of carbon-based materials as a family, is presented.

6.3.1 Carbon K-edge EELS features

The features contained within the carbon K-edge are due to the loss of kinetic energy of electrons in the incident beam to the specimen, exciting an atomic $1s$ electron to unoccupied orbitals above the Fermi level. The first feature at 285 eV is due to a transition of a $1s$ electron to the π^* anti-bonding orbital, the next $\approx$ 20 eV contain features due to excitations to σ^* states. Furthermore, within the C K-edge NES, a feature is observed at approximately 330 eV caused by multiple scattering [223] (labelled as MS). Figure 6.2 shows a typical core-loss EEL spectrum obtained from a graphitic material.

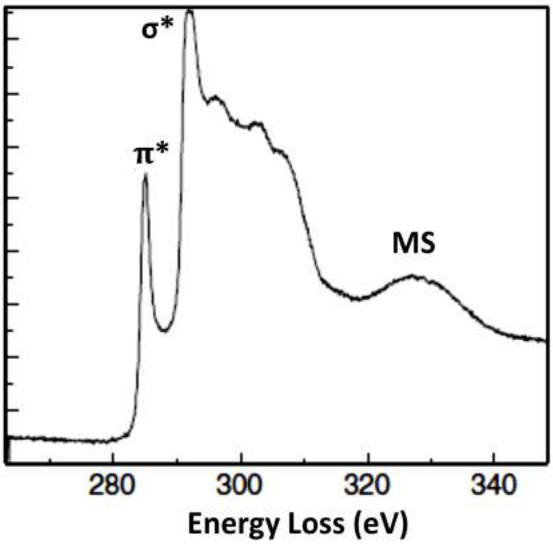

Figure 6.2 Typical carbon K-edge obtained from a graphitic material (reproduced from [224]).

6.3.2 Measurement of Bond Type

As mentioned in Chapter 1, carbon materials are highly versatile owing to the strong dependence of their physical properties on the ratio of sp^2 to sp^3 bonds. EELS performed in a TEM is currently the preferred method to quantitatively extract the sp^2 fraction of carbon-based materials at a high spatial resolution. The high-energy incident electrons can produce transitions from $1s$ core level electrons to unoccupied solid states, and the resulting ELNES reflects features in these unoccupied electronic states, namely π^* and σ^* for carbon atoms. The carbon K-edge spectrum can thus be interpreted as a superposition of integrated intensities over an energy window, which are related to transitions from the $1s$ core level to states projected distinctly on p_z or (p_x, p_y) symmetry orbitals. These two intensities are I_{π^*} and I_{σ^*}, and their relative weight is described by the normalised $R = \dfrac{I_{\pi^*}}{I_{\pi^*} + I_{\sigma^*}}$ ratio. As I_{π^*} is exclusively provided by carbon atoms in sp^2 hybridisation, the comparison of the normalised ratio of the unknown carbon material with that of a suitable 100% sp^2 reference material such as highly-ordered graphite, gives a quantity directly proportional to the sp^2 fraction [225, 226]. The usual methods dedicated to extract R-ratios from experimental C K-edge spectra can be divided in two groups. The first group is based on the assumption that there is no overlap between the π^* and σ^* peaks. The most widely-used method is the “two-window method” established by Berger and McKenzie [225, 226] by which to characterize the sp^2/sp^3 contents of DLC films by taking the ratio of the area within an integration window centred upon the π^* feature at the C K-edge (e.g. a 5 eV window onset at 282.5 eV) to the area within a window containing both π^* and σ^* features (e.g. a 20 eV window onset at 282.5 eV). It is also possible to perform the integration at the lower edge of both windows aligned to the edge onset. In the second group, there are methods which take into account the overlapping between the π^* and σ^* components. Within this group, the most feasible method involves fitting a portion of the spectrum by combination of only three Gaussian functions [227, 228]. Briefly, the *1s* to π^* peak intensity at the C K-edge (background subtracted and deconvoluted to remove plural scattering), I_{π^*}, is measured using a Gaussian fitting procedure and normalised to the total C K-edge intensity in a window of up to 20 eV extending from the edge onset. The major drawback of the second type of methods is that the fluctuations in the fitting process, can give rise to significant uncertainties in the R-ratio calculations. Therefore, as previously pointed out in an earlier study [229], this method can not reliably extract R-ratios from EELS C K-edge spectra. Hence, the first category of methods are favourable to deduce the sp^2. In order to calculate the sp^2 from the normalised intensity ratio, the most used formula is what was proposed first by Cuomo *et al.* [226]:

$$\frac{I^{\mathrm{u}}_{\pi^*}/I^{\mathrm{u}}_{\sigma^*}}{I^{\mathrm{s}}_{\pi^*}/I^{\mathrm{s}}_{\sigma^*}} = \frac{3x}{4-x} \tag{6.1}$$

where x is the sp^2 fraction, and u and s stand for unknown and standard (reference) samples, respectively.

6.4 Electron Microscopy of Plasma-Treated Graphene

The graphene samples for this work were prepared using the method described in Chapter 2. The same holds true for subsequent transfer of as-grown samples onto the TEM support. The as-transferred samples were then loaded into our house-built furnace for performing the remote plasma treatment as explained before in Chapter 2.

6.4.1 HRTEM Studies

Figure 6.3 shows HRTEM images and corresponding fast Fourier transforms (FFT) of pristine and plasma treated graphene. At least 10 areas were assessed when performing HRTEM to ensure the reproducibility of the results. Thus, the presented images here are representative of the microstructures observed for each set of samples.

In the case of pristine graphene (Figure 6.3 (a_1)) lattice fringes are resolved, indicating the presence of a highly-crystalline structure. To further evaluate the quality of graphene, EDP was recorded (Figure 6.3 (a_2)) which shows perfect six-fold symmetry spots indicative of a highly-crystalline lattice. Furthermore, one can get more information about the number of layers present based on the intensity of inner and outer

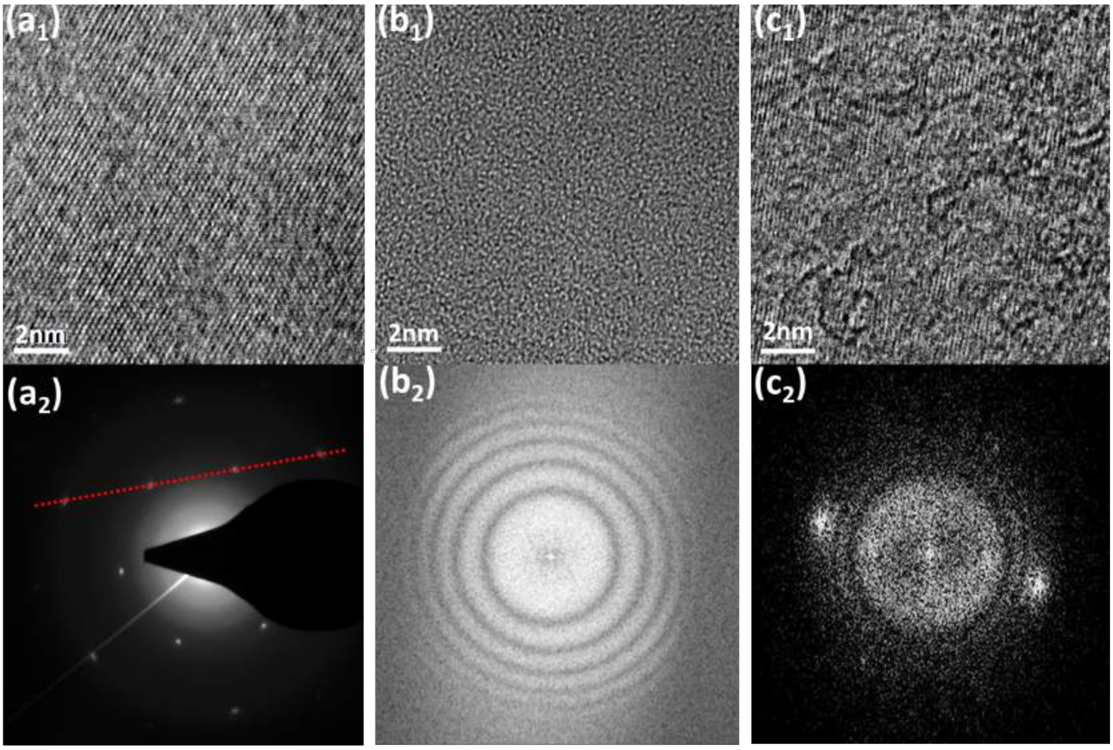

Figure 6.3 HRTEM analysis of pristine and plasma-functionalised graphene. (a_1) Smoothed HRTEM image of pristine graphene and, (a_2) the corresponding EDP. The red dotted line shows where the intensity profile was generated. (b_1) HRTEM image of O_2-plasma treated graphene and, (b_2) the corresponding FFT. (c_1) HRTEM image of H_2+HN_3 plasma treated graphene and, ($_2$) the corresponding FFT.

spots in the DP as elaborated in Chapter 1. The intensity ratio analysis was performed along the red dotted line in Figure 6.3 (a_2). This result along with those from Raman spectroscopy (not presented here due to irrelevance), confirmed that the graphene was monolayer. The intensity profile of the EDP and the the FFT of Figure 6.3 (a_1) are shown in Figure 6.4.

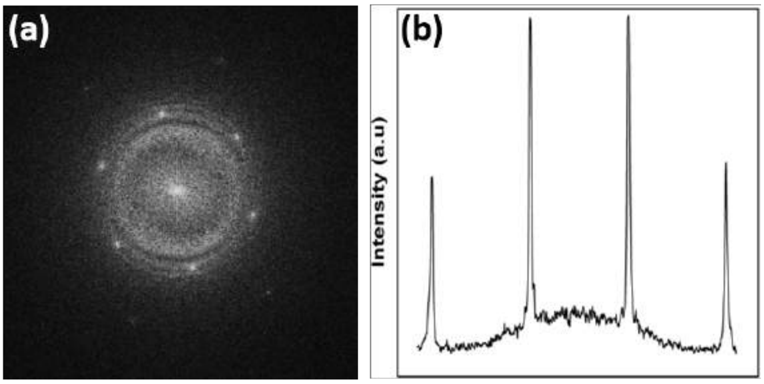

Figure 6.4 (a) FFT of HRTEM image of pristine graphene. (b) The intensity profile along the red dotted line in image (a_2).

The HRTEM image and FFT of an O_2-plasma treated sample (see Figure 6.3 (b_1) & (b_2)) undergo a significant change. No considerable features can be resolved in the HRTEM image. From the corresponding FFT of the HRTEM image, no discrete diffraction spots can be resolved and it consists of diffused concentric rings which are typical for randomly arranged structures with very small structural units with short range ordering.

Upon reducing with the subsequent H_2+NH_3 plasma treatment, the sample experiences an obvious change in terms of crystallinity and ordering once again. This is apparent in the HRTEM image (Figure 6.3 (c_1)), as lattice fringes have appeared to some extent, indicative of some lattice restoration and partial ordering. The corresponding FFT of the HRTEM (shown in Figure 6.3 (c_2)), displays some reversion from diffuse rings to discrete spots, however, a full set of spots is not observed as was the case for pristine graphene; which implies partial ordering or crystallinity following the H_2+NH_3 plasma treatment.

6.4.2 EELS Studies

Figure 6.5 shows EEL spectrum and the carbon K-energy ELNES of pristine graphene, O_2-plasma treated and H_2+NH_3-plasma treated graphene. In the case of pristine graphene, as evident in Figure 6.5 (a) and (b), the sharp and very well-defined π^* and σ^* peaks, with four well defined shoulders detectable for σ^* peak within ELNES, are all signs of long-range periodicity and symmetry in the extremely crystalline structure of graphene. To some extent, it is appropriate to assume that the density of these unoccupied states is intrinsically linked to and in some cases mirror the density of the actual bonding orbitals.

In the case of the O_2-plasma treated sample, shown in Figure 6.5 (c), poorly-defined π^* and σ^* peaks are indications of a highly disordered graphitic carbon. Moreover, an intense oxygen K-edge peak shows the successful oxidation of graphene with our remote plasma.

The subsequent H_2+NH_3 plasma treatment of the oxidised graphene (see Figure 6.5 (c)) leads to better definition and higher intensity of the π^* peak, indicating an increase in the extent of ordering and a restoration of crystallinity in the graphene lattice. Moreover, the now less intense O K-edge peak implies that oxygen has been removed. The oxygen functional groups are removed through reactions with hydrogen and ammonia radicals and are either substitutionally replaced by nitrogen groups or else restoration of the graphitic lattice occurs.

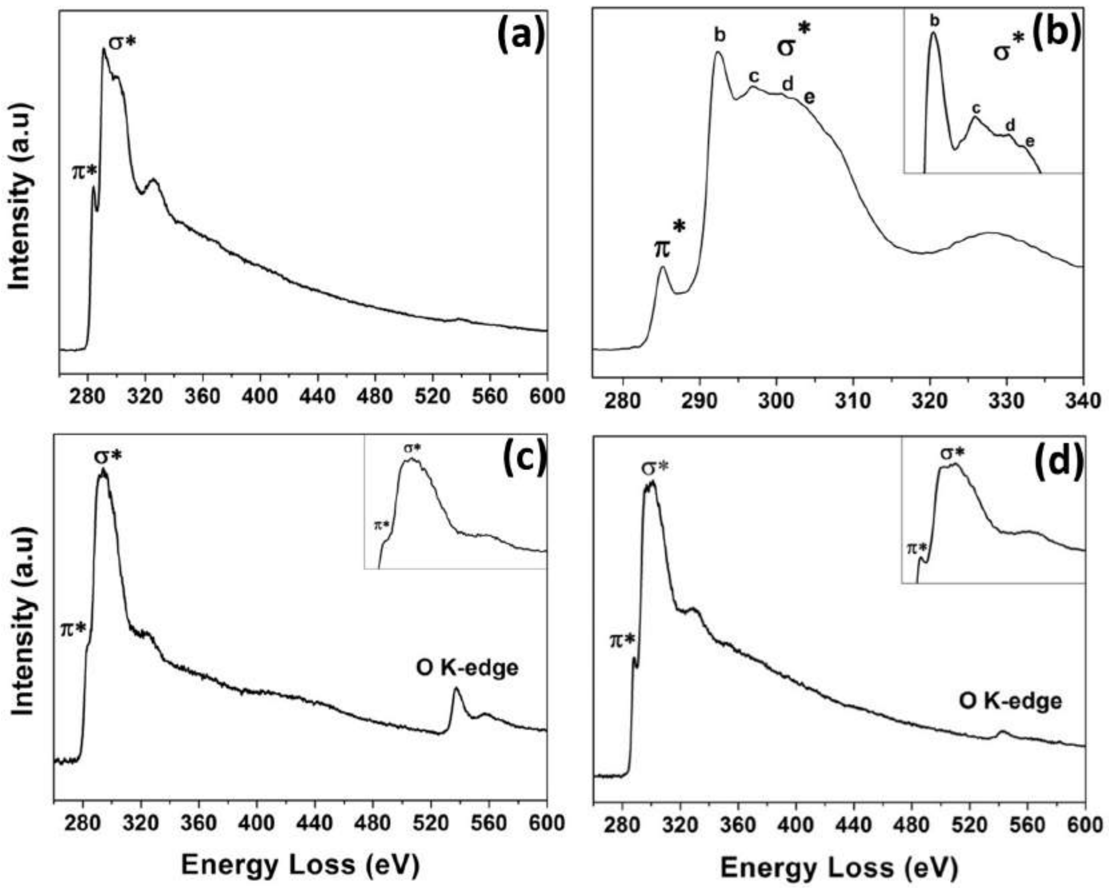

Figure 6.5 EEL spectra of pristine and plasma-treated graphene samples. (a) Pristine graphene. (b) Carbon ELNES of pristine graphene sample. The inset is a zoomed-in view of the σ^* peak. (c) EEL spectrum of O_2-plasma treated graphene. The inset is zoomed-in view of C K-edge. (d) EEL spectrum of H_2+NH_3 plasma treated graphene. The inset is enlarged view of C K-edge.

6.5 Conclusions

In this Chapter I have demonstrated the capability of HRTEM/EELS as a powerful characterisation tool for quality assessment of the plasma treated graphene. This method is relatively straightforward to implement and fairly trivial to interpret. The reason behind this is that the C K-edge ELNES contains three distinct peaks that evolve upon any perturbation to the carbon lattice under examination. This method can be extended to other members of the family of nanocarbons to reliably monitor the structural evolution upon plasma functionalisation as an intervening method to the crystal lattice of carbon.

In the case of our system, we showed the evolution of pristine untreated graphene to a disordered oxygenated graphene upon O_2 plasma treatment and subsequent partial restoration of crystallinity of the graphene lattice following H_2+NH_3 plasma. This study further probes our N-doped graphene using several spectroscopic techniques, thus offering further information on the nature of doping in graphene.

Chapter 7

Conclusions and Outlook

This study set out to explore the potential and the capabilities of TEM-based characterisation techniques in the emerging field of carbon nanomaterials, graphene in particular. The study was divided into parts; the first part has been exploring the potential application of HRTEM/EELS as a characterisation tool in the field of functionalised graphene. Despite existence of a rich literature on EELS study of graphene and other carbon based materials, a dedicated coherent body of literature on HRTEM/EELS of plasma-functionalised graphene is lacking. The main empirical findings on this topic were summarised in Chapter 6: Electron Microscopic Study of Plasma-Functionalised Graphene. Within this Chapter, we showed for the first time that, HRTEM/EELS can be employed as a quality control check after various plasma treatments on graphene. It is shown that by careful monitoring the evolution of carbon K-edge spectrum, one can extract useful information on the extent of ordering and the nature of functionlities.

One of the key factors to attain the most from a TEM study of 2D materials is sample quality. Particularly in the case of graphene and related systems, one of the main goals is to be able to investigate directly the individual carbon atoms and edges in the crystal lattice. To do so, it was envisaged a potential pathway would be to develop a production method that leads to solely monolayer graphene films; and this comprised the main goal of the second part of this study. The general theoretical and experimental literature on this subject and specifically in the context of defining a certain mechanism is inconclusive and rather scattered and, there still remain many open questions to be addressed. This study sought to answer two of these questions: (a) How can the substrate for CVD process be modified in order to achieve large area entirely monolayer graphene. (b) How could one further increase the robustness of graphene when it is transferred to a TEM support.

The empirical findings are chapter specific and were summarised within respective empirical chapters: Chapter 4-Modification of CVD of Graphene via Catalyst Optimisation, and Chapter 5-AC-TEM study of Isotope-enriched Graphene. To answer the first question, I investigated the effect of optimising a copper catalyst surface with an element that is inexpensive, carbide forming, and can be feasibly deposited onto the copper surface. After much research, chromium was chosen as it meets all the requirements. By depositing a thin chromium film on copper, I could successfully suppress the formation on multilayer graphene formation. Comprehensive study of all aspects of growth process, paved the way to propose a reaction mechanism for the observed effect.

The second question of this part is answered in Chapter 5, where the effect of kinetic isotope effect on the strength of bonds in isotope graphene is investigated. The results obtained by AC-TEM, showed that the bonding properties are different from that of “normal” graphene and they showed an unprecedented beam induced damage resistance, as well other uncommon edge features that have not been reported to date. Nonetheless, the experimentally observed ultralong bond lengths in isotope-enriched graphene, contrasts the stablished principles in quantum chemistry and therefore, further confirmation of such long bonds is necessary. For instance, more studies needed with sophisticated AC-STEM instruments to undoubtedly measure the bonds in the isotope-enriched graphene. This technique has been used previously in graphene research to identify structural defects and foreign atoms incorporation in the lattice. Another avenue would be employing molecular dynamic simulations to calculate the unsual edge states such as those containing large rings and extended KLs. Exploring the mechanical properties of isotope graphene by Scanning Probe Microscopic techniques and a dedicated STEM analysis of bonding characteristics can be considered as future research strategies. Furthermore, more simulation work could also be beneficial for a more comprehensive understanding of isotope graphene as the “stronger” sibling of normal graphene.

This study has offered alternative routes for a yet more efficient application of TEM in nanocarbon research. As a direct consequence, the study encountered a number of limitation in sample cleanliness, which need to be addressed.

In spite of outstanding achievements that have been made in graphene research, insufficient effort has been put into the area of isotope graphene and some potential applications such as stronger graphene-based TEM support are envisaged for this material.

Bibliography

[1] H. W. Kroto, J. R. Heath, S. C. O'Brien, R. F. Curl, and R. E. Smalley. C_{60}: Buckminsterfullerene. *Nature*, 318(6042):162–163, 1985.

[2] S. Iijima. Helical microtubules of graphitic carbon. *Nature*, 354(6348):56–58, 1991.

[3] K. S. Novoselov, A. K. Geim, S. V. Morozov, D. Jiang, Y. Zhang, S. V. Dubonos, I. V. Grigorieva, and A. A. Firsov. Electric field effect in atomically thin carbon films. *Science*, 306(5696):666–9, 2004.

[4] M. Scarselli, P. Castrucci, and M. De Crescenzi. Electronic and optoelectronic nano-devices based on carbon nanotubes. *Journal of Physics: Condensed Matter*, 24(31):313202, 2012.

[5] J. Robertson. Diamond-like amorphous carbon. *Materials Science and Engineering: R: Reports*, 37(4-6):129 – 281, 2002.

[6] J. C. Meyer, A.K. Geim, M.I. Katsnelson, K.S. Novoselov, T.J. Booth, and S. Roth. The structure of suspended graphene sheets. *Nature*, 446:60–63, 2007.

[7] R. C. Thompson-Flagg, M. J. B Moura, and M. Marder. Rippling of graphene. *EPL (Europhysics Letters)*, 85(4):46002, 2009.

[8] A. K. Geim and K. S. Novoselov. The rise of graphene. *Nature Materials*, 6(3): 183–191, 2007.

[9] S. Morozov, K. Novoselov, M. Katsnelson, F. Schedin, D. Elias, J. Jaszczak, and A. Geim. Giant intrinsic carrier mobilities in graphene and its bilayer. *Physical Review Letters*, 100(1), 2008.

[10] J.E. Hill. *One-dimensional Electron Systems on Graphene Edges*. University of Texas at Austin, 2007. ISBN 9780549435808.

[11] C. Lee, X. Wei, J. W. Kysar, and J. Hone. Measurement of the elastic properties and intrinsic strength of monolayer graphene. *Science*, 321(5887):385–388, 2008.

[12] I. W. Frank, D. M. Tanenbaum, A. M. van der Zande, and P. L. McEuen. Mechanical properties of suspended graphene sheets. *Journal of Vacuum Science & Technology B*, 25(6):2558–2561, 2007.

[13] R. Faccio, P. A. Denis, H. Pardo, C. Goyenola, and A. W. Mombrú. Mechanical properties of graphene nanoribbons. *Journal of Physics: Condensed Matter*, 21 (28):285304, 2009.

[14] A. A. Balandin, S. Ghosh, W. Bao, I. Calizo, D. Teweldebrhan, F. Miao, and C. N. Lau. Superior thermal conductivity of single-layer graphene. *Nano Letters*, 8(3): 902–907, 2008.

[15] W. Bao, F. Miao, Z. Chen, H. Zhang, W. Jang, C. Dames, and C. Lau. Controlled ripple texturing of suspended graphene and ultrathin graphite membranes. *Nature Nanotechnology*, 4(9):562–566, 2009.

[16] R. R. Nair, P. Blake, A. N. Grigorenko, K. S. Novoselov, T. J. Booth, T. Stauber, N. M. R. Peres, and A. K. Geim. Fine structure constant defines visual transparency of graphene. *Science*, 320(5881):1308–1308, 2008.

[17] K. S. Novoselov, V. I. Fal'ko, L. Colombo, P. R. Gellert, M. G. Schwab, and K. Kim. A roadmap for graphene. *Nature*, 490(7419):192–200, 2012.

[18] Y. Hernandez, V. Nicolosi, M. Lotya, F. M. Blighe, Z. Sun, S. De, I. T. McGovern, B. Holland, M. Byrne, Y. K. Gun'Ko, et al. High-yield production of graphene by liquid-phase exfoliation of graphite. *Nature Nanotechnology*, 3(9):563–568, 2008.

[19] K. R. Paton, E. Varrla, C. Backes, R. J. Smith, U. Khan, A. O'Neill, C. Boland, M. Lotya, O. M Istrate, P. King, et al. Scalable production of large quantities of defect-free few-layer graphene by shear exfoliation in liquids. *Nature Materials*, 13 (6):624–630, 2014.

[20] C. Berger, Z. Song, T. Li, X. Li, A. Y. Ogbazghi, R. Feng, Z. Dai, A. N. Marchenkov, E. H. Conrad, P. N. First, et al. Ultrathin epitaxial graphite: 2d electron gas properties and a route toward graphene-based nanoelectronics. *The Journal of Physical Chemistry B*, 108(52):19912–19916, 2004.

[21] C. Berger, Z. Song, X. Li, X. Wu, N. Brown, C. Naud, D. Mayou, T. Li, J. Hass, A. N. Marchenkov, et al. Electronic confinement and coherence in patterned epitaxial graphene. *Science*, 312(5777):1191–1196, 2006.

[22] W. A. De Heer, C. Berger, X. Wu, P. N. First, E. H. Conrad, X. Li, T. Li, M. Sprinkle, J. Hass, M. L. Sadowski, et al. Epitaxial graphene. *Solid State Communications*, 143(1):92–100, 2007.

[23] J. Cai, P. Ruffieux, R. Jaafar, M. Bieri, T. Braun, S. Blankenburg, M. Muoth, A. P. Seitsonen, M. Saleh, X. Feng, et al. Atomically precise bottom-up fabrication of graphene nanoribbons. *Nature*, 466(7305):470–473, 2010.

[24] X. Li, W. Cai, J. An, S. Kim, J. Nah, D. Yang, R. Piner, A. Velamakanni, I. Jung, E. Tutuc, S. K. Banerjee, L. Colombo, and R. S. Ruoff. Large-area synthesis of high-quality and uniform graphene films on copper foils. *Science*, 324(5932): 1312–4, 2009.

[25] A. C. Ferrari, F. Bonaccorso, V. Fal'Ko, K. S. Novoselov, S. Roche, P. Bøggild, S. Borini, F. H. L. Koppens, V. Palermo, N. Pugno, et al. Science and technology roadmap for graphene, related two-dimensional crystals, and hybrid systems. *Nanoscale*, 7(11):4598–4810, 2015.

[26] A. W. Cummings, D. Duong, V. Nguyen, D. Van Tuan, J. Kotakoski, J. E. Barrios Vargas, Y. Lee, and S. Roche. Charge transport in polycrystalline graphene: challenges and opportunities. *Advanced Materials*, 26(30):5079–5094, 2014.

[27] A. H. Castro Neto and K. Novoselov. New directions in science and technology two-dimensional crystals. *Reports on Progress in Physics*, 74(8):082501, 2011.

[28] Y. Wu, T. Yu, and Z. Shen. Two-dimensional carbon nanostructures: Fundamental properties, synthesis, characterization, and potential applications. *Journal of Applied Physics*, 108(7):071301, 2010.

[29] H. Lipson and A. R. Stokes. The structure of graphite. In *Proceedings of the Royal Society of London A: Mathematical, Physical and Engineering Sciences*, volume 181, pages 101–105. The Royal Society, 1942.

[30] M. Aoki and H. Amawashi. Dependence of band structures on stacking and field in layered graphene. *Solid State Communications*, 142(3):123–127, 2007.

[31] M. Koshino. Stacking-dependent optical absorption in multilayer graphene. *New Journal of Physics*, 15(1):015010, 2013.

[32] A. I. Cocemasov, D. L. Nika, and A. A. Balandin. Phonons in twisted bilayer graphene. *Physical Review B*, 88(3):035428, 2013.

[33] K. Kim, A. L. Walter, L. Moreschini, T. Seyller, K. Horn, E. Rotenberg, and A. Bostwick. Coexisting massive and massless dirac fermions in symmetry-broken bilayer graphene. *Nature Materials*, 12(10):887–892, 2013.

[34] C. Lu, Y. Lin, Z. Liu, C. Yeh, K. Suenaga, and P. Chiu. Twisting bilayer graphene superlattices. *ACS Nano*, 7(3):2587–2594, 2013.

[35] C. Wirtz, N. C. Berner, and G. S. Duesberg. Large-scale diffusion barriers from cvd grown graphene. *Advanced Materials Interfaces*, 2(14):2587–2594, 2015.

[36] J. Gao, J. Yip, J. Zhao, B. I. Yakobson, and F. Ding. Graphene nucleation on transition metal surface: Structure transformation and role of the metal step edge. *Journal of the American Chemical Society*, 133(13):5009–5015, 2011.

[37] Jürn WP Schmelzer, Gerd Röpke, and Vyatcheslav B Priezzhev. *Nucleation theory and applications*. Wiley Online Library, 2005. ISBN 9783527604791.

[38] A. Reina, X. Jia, J. Ho, D. Nezich, H. Son, V. Bulovic, M. S. Dresselhaus, and J. Kong. Large area, few-layer graphene films on arbitrary substrates by chemical vapor deposition. *Nano Letters*, 9(1):30–35, 2008.

[39] C. Mattevi, H. Kim, and M. Chhowalla. A review of chemical vapour deposition of graphene on copper. *Journal of Materials Chemistry*, 21(10):3324, 2011.

[40] K. Kim, Y. Zhao, H. Jang, S. Lee, J. Kim, K. S. Kim, J. Ahn, P. Kim, J. Choi, and B. Hong. Large-scale pattern growth of graphene films for stretchable transparent electrodes. *Nature*, 457(7230):706–710, 2009.

[41] S. Chae, F. Gunes, K. Kim, E. Kim, G. Han, S. Kim, H. Shin, S. Yoon, J. Choi, M. Park, et al. Synthesis of large-area graphene layers on poly-nickel substrate by chemical vapor deposition: wrinkle formation. *Advanced Materials*, 21(22): 2328–2333, 2009.

[42] Q. Yu, J. Lian, S. Siriponglert, H. Li, Y. P. Chen, and S. Pei. Graphene segregated on ni surfaces and transferred to insulators. *Applied Physics Letters*, 93(11):113103, 2008.

[43] H. Kim, E. Saiz, M. Chhowalla, and C. Mattevi. Modeling of the self-limited growth in catalytic chemical vapor deposition of graphene. *New Journal of Physics*, 15(5):053012, 2013.

[44] I. Vlassiouk, M. Regmi, P. Fulvio, S. Dai, P. Datskos, G. Eres, and S. Smirnov. Role of hydrogen in chemical vapor deposition growth of large single-crystal graphene. *ACS Nano*, 5(7):6069–6076, 2011.

[45] S. Bhaviripudi, X. Jia, M. S. Dresselhaus, and J. Kong. Role of kinetic factors in chemical vapor deposition synthesis of uniform large area graphene using copper catalyst. *Nano Letters*, 10(10):4128–33, 2010.

[46] X. Zhang, J. Ning, X. Li, B. Wang, L. Hao, M. Liang, M. Jin, and L. Zhi. Hydrogen-induced effects on the cvd growth of high-quality graphene structures. *Nanoscale*, 5(18):8363–8366, 2013.

[47] M. Losurdo, M. M. Giangregorio, P. Capezzuto, and G. Bruno. Graphene cvd growth on copper and nickel: role of hydrogen in kinetics and structure. *Physical Chemistry Chemical Physics*, 13(46):20836–20843, 2011.

[48] G. Wang and J. Nakamura. Structure sensitivity for forward and reverse water-gas shift reactions on copper surfaces: a dft study. *The Journal of Physical Chemistry Letters*, 1(20):3053–3057, 2010.

[49] J. Greeley and M. Mavrikakis. Surface and subsurface hydrogen: adsorption properties on transition metals and near-surface alloys. *The Journal of Physical Chemistry B*, 109(8):3460–3471, 2005.

[50] H. Shu, X. Tao, and F. Ding. What are the active carbon species during graphene chemical vapor deposition growth? *Nanoscale*, 7:1627–1634, 2015.

[51] T. Ohta, A. Bostwick, T. Seyller, K. Horn, and E. Rotenberg. Controlling the electronic structure of bilayer graphene. *Science*, 313(5789):951–954, 2006.

[52] Y. Zhang, T. Tang, C. Girit, Z. Hao, M. C. Martin, A. Zettl, M. F. Crommie, Y. Shen, and F. Wang. Direct observation of a widely tunable bandgap in bilayer graphene. *Nature*, 459(7248):820–823, 2009.

[53] C. Lui, Z. Li, K. Mak, E. Cappelluti, and T. F. Heinz. Observation of an electrically tunable band gap in trilayer graphene. *Nature Physics*, 7(12):944–947, 2011.

[54] F. Schwierz. Graphene transistors. *Nature Nanotechnology*, 5(7):487–496, 2010.

[55] S. Lee, K. Lee, and Z. Zhong. Wafer scale homogeneous bilayer graphene films by chemical vapor deposition. *Nano Letters*, 10(11):4702–4707, 2010.

[56] W. Liu, H. Li, C. Xu, Y. Khatami, and K. Banerjee. Synthesis of high-quality monolayer and bilayer graphene on copper using chemical vapor deposition. *Carbon*, 49(13):4122–4130, 2011.

[57] D. B. Williams and C. B. Carter. *Transmission Electron Microscopy: A Textbook for Materials Science*. Springer, 2009. ISBN 9780387765006.

[58] M. De Graef. *Introduction to Conventional Transmission Electron Microscopy*. Cambridge University Press, 2003. ISBN 9780521629959.

[59] P. J. Goodhew, J. Humphreys, and R. Beanland. *Electron Microscopy and Analysis, Third Edition*. Taylor & Francis, 2000. ISBN 9780748409686.

[60] A. V. Crewe, J. Wall, and L. M. Welter. A high-resolution scanning transmission electron microscope. *Journal of Applied Physics*, 39(13):5861–5868, 1968.

[61] J. Wall, J. Langmore, M. Isaacson, and A. V. Crewe. Scanning transmission electron microscopy at high resolution. *Proceedings of the National Academy of Sciences*, 71(1):1–5, 1974.

[62] S. J. Pennycook and P. D. Nellist. *Scanning Transmission Electron Microscopy: Imaging and Analysis*. Springer New York, 2011. ISBN 9781441972002.

[63] R. Brydson. *Aberration-Corrected Analytical Transmission Electron Microscopy*. RMS - Royal Microscopical Society. Wiley, 2011. ISBN 9781119979906.

[64] M. Haider, S. Uhlemann, E. Schwan, H. Rose, B. Kabius, and K. Urban. Electron microscopy image enhanced. *Nature*, 392:768–769, 1998.

[65] O. L. Krivanek, P. D. Nellist, N. Dellby, M. F. Murfitt, and Z. Szilagyi. Towards sub-0.5 å electron beams. *Ultramicroscopy*, 96(3):229–237, 2003.

[66] P. E. Batson, N. Dellby, and O. L. Krivanek. Sub-ångstrom resolution using aberration corrected electron optics. *Nature*, 418(6898):617–620, 2002.

[67] Y. Lin, C. Jin, J. Lee, S. Jen, K. Suenaga, and P. Chiu. Clean transfer of graphene for isolation and suspension. *ACS Nano*, 5(3):2362–2368, 2011.

[68] A. C. Ferrari, J. C. Meyer, V. Scardaci, C. Casiraghi, M. Lazzeri, F. Mauri, S. Piscanec, D. Jiang, K. S. Novoselov, S. Roth, and A. K. Geim. Raman spectrum of graphene and graphene layers. *Physical Review Letters*, 97(18):187401–4, 2006.

[69] C. Casiraghi, A. Hartschuh, E. Lidorikis, H. Qian, H. Harutyunyan, T. Gokus, K. S. Novoselov, and A. C. Ferrari. Rayleigh imaging of graphene and graphene layers. *Nano Letters*, 7(9):2711–2717, 2007.

[70] S. Roddaro, P. Pingue, V. Piazza, V. Pellegrini, and F. Beltram. The optical visibility of graphene: Interference colors of ultrathin graphite on sio2. *Nano Letters*, 7(9):2707–2710, 2007.

[71] P. Blake, E. W. Hill, A. H. Castro Neto, K. S. Novoselov, D. Jiang, R. Yang, T. J. Booth, and A. K. Geim. Making graphene visible. *Applied Physics Letters*, 91(6): 063124, 2007.

[72] D. L. Dorset. *Structural Electron Crystallography*. Springer US, 2013. ISBN 9781475766219.

[73] A. Doerr. Structural biology: Electron crystallography goes 3d with micro electron diffraction. *Nature methods*, 11(1):6–7, 2014.

[74] B. Fultz and J.M. Howe. *Transmission Electron Microscopy and Diffractometry of Materials*. Graduate Texts in Physics. Springer Berlin Heidelberg, 2012. ISBN 9783642297618.

[75] J. C. Meyer, A. K. Geim, M. I. Katsnelson, K. S. Novoselov, D. Obergfell, S. Roth, C. Girit, and A. Zettl. On the roughness of single-and bi-layer graphene membranes. *Solid State Communications*, 143(1):101–109, 2007.

[76] J.M. Zuo and J.C.H. Spence. *Electron Microdiffraction*. Springer US, 2013. ISBN 9781489923530.

[77] J.C.H. Spence. *High-Resolution Electron Microscopy*. OUP Oxford, 2013. ISBN 9780191508400.

[78] A. Kumar, H. Nolan, N. McEvoy, E. Rezvani, R. L. Doyle, M. E. G. Lyons, and G. S. Duesberg. Plasma-assisted simultaneous reduction and nitrogen doping of graphene oxide nanosheets. *Journal of Materials Chemistry A*, 1(14):4431–4435, 2013.

[79] N. McEvoy, H. Nolan, A. Kumar Nanjundan, T. Hallam, and G. S. Duesberg Duesberg. Functionalisation of graphene surfaces with downstream plasma treatments. *Carbon*, 54:283–290, 2013.

[80] A. Lherbier, S. M. Dubois, X. Declerck, Y. Niquet, S. Roche, and J. Charlier. Transport properties of graphene containing structural defects. *Physical Review B*, 86(7):075402, 2012.

[81] A. W. Tsen, L. Brown, M. P. Levendorf, F. Ghahari, P. Y. Huang, R. W. Havener, C. S. Ruiz-Vargas, D. A. Muller, P. Kim, and J. Park. Tailoring electrical transport across grain boundaries in polycrystalline graphene. *Science*, 336(6085):1143–1146, 2012.

[82] A. J. Stone and D. J. Wales. Theoretical studies of icosahedral c_{60} and some related species. *Chemical Physics Letters*, 128(5):501–503, 1986.

[83] K. Suenaga, H. Wakabayashi, M. Koshino, Y. Sato, K. Urita, and S. Iijima. Imaging active topological defects in carbon nanotubes. *Nature Nanotechnology*, 2(6): 358–360, 2007.

[84] J. Kotakoski, A. V. Krasheninnikov, U. Kaiser, and J. C. Meyer. From point defects in graphene to two-dimensional amorphous carbon. *Physical Review Letters*, 106(10):105505, 2011.

[85] J. Chen, W. G. Cullen, C. Jang, M. S. Fuhrer, and E. D. Williams. Defect scattering in graphene. *Physical Review Letters*, 102(23):236805, 2009.

[86] X. Wang, Y. Zhang, F. Liu, Y. Ma, W. Feng, and X. Zhang. Dynamic nano-pulling effect of the boron-functionalized graphene monovacancy for molecule dissociation. *Journal of Physics D: Applied Physics*, 46(38):385302, 2013.

[87] Y. Kim, J. Ihm, E. Yoon, and G. Lee. Dynamics and stability of divacancy defects in graphene. *Physical Review B*, 84(7):075445, 2011.

[88] G. Lee, C. Z. Wang, E. Yoon, N. Hwang, D. Kim, and K. Ho. Diffusion, coalescence, and reconstruction of vacancy defects in graphene layers. *Physical Review Letters*, 95(20):205501, 2005.

[89] J. Guo, J. Lee, C. I. Contescu, N. C. Gallego, S. T. Pantelides, S. J. Pennycook, B. A. Moyer, and M. F. Chisholm. Crown ethers in graphene. *Nature Communications*, 5, 2014.

[90] F. Banhart, J. Kotakoski, and A. V. Krasheninnikov. Structural defects in graphene. *ACS Nano*, 5(1):26–41, 2010.

[91] C. Weeks, J. Hu, J. Alicea, M. Franz, and R. Wu. Engineering a robust quantum spin hall state in graphene via adatom deposition. *Physical Review X*, 1(2):021001, 2011.

[92] C. O. Girit, J. C. Meyer, R. Erni, M. D. Rossell, C. Kisielowski, L. Yang, C. H. Park, M. F. Crommie, M. L. Cohen, S. G. Louie, and A. Zettl. Graphene at the edge: stability and dynamics. *Science*, 323(5922):1705–8, 2009.

[93] Y. Son, M. L. Cohen, and S. G. Louie. Half-metallic graphene nanoribbons. *Nature*, 444(7117):347–349, 2006.

[94] K. He, A. W. Robertson, S. Lee, E. Yoon, G. Lee, and J. H. Warner. Extended klein edges in graphene. *ACS Nano*, 8(12):12272–12279, 2014.

[95] J. S. Kim, J. H. Warner, A. W. Robertson, and A. I. Kirkland. Formation of klein edge doublets from graphene monolayers. *ACS Nano*, 2015.

[96] P. Koskinen, S. Malola, and H. Häkkinen. Evidence for graphene edges beyond zigzag and armchair. *Physical Review B*, 80(7):073401, 2009.

[97] A. Chuvilin, J. C. Meyer, G. Algara-Siller, and U. Kaiser. From graphene constrictions to single carbon chains. *New Journal of Physics*, 11(8):083019, 2009.

[98] D. J. Klein. Graphitic polymer strips with edge states. *Chemical Physics Letters*, 217(3):261–265, 1994.

[99] J. C. Meyer, A. K. Geim, M. I. Katsnelson, K. S. Novoselov, T. J. Booth, and S. Roth. The structure of suspended graphene sheets. *Nature*, 446(7131):60–63, 2007.

[100] W. T. Read and W. Shockley. Dislocation models of crystal grain boundaries. *Physical Review*, 78(3):275, 1950.

[101] O. V. Yazyev and S. G. Louie. Electronic transport in polycrystalline graphene. *Nature Materials*, 9(10):806–809, 2010.

[102] P. Y. Huang, C. S. Ruiz-Vargas, A. M. Van der Zande, W. S. Whitney, M. P. Levendorf, J. W. Kevek, S. Garg, J. S. Alden, C. J. Hustedt, Y. Zhu, et al. Grains and grain boundaries in single-layer graphene atomic patchwork quilts. *Nature*, 469(7330):389–392, 2011.

[103] K. Kim, Z. Lee, W. Regan, C. Kisielowski, M. F. Crommie, and A. Zettl. Grain boundary mapping in polycrystalline graphene. *ACS Nano*, 5(3):2142–2146, 2011.

[104] V.J. Keast. Application of eels in materials science. *Materials Characterization*, 73(0):1–7, 2012.

[105] R. Egerton. *Electron Energy-Loss Spectroscopy in the Electron Microscope*. Springer US, 2011. ISBN 9781441995834.

[106] J. Park, S. Heo, J. Chung, H. Kim, H. Lee, K. Kim, and G. Park. Bandgap measurement of thin dielectric films using monochromated stem-eels. *Ultramicroscopy*, 109(9):1183 – 1188, 2009.

[107] L. Gu, V. Srot, W. Sigle, C. Koch, P. Van Aken, F. Scholz, S. B. Thapa, C. Kirchner, M. Jetter, and M. Ruhle. Band-gap measurements of direct and indirect semiconductors using monochromated electrons. *Physical Review B*, 75:195214, 2007.

[108] R. Erni, S. Lazar, and N. D. Browning. Prospects for analyzing the electronic properties in nanoscale systems by veels. *Ultramicroscopy*, 108(3):270–276, 2008.

[109] V. J. Keast. Bandstructure calculations for the simulation of low-loss eels and plasmon energies. *Microscopy and Microanalysis*, 10:854–855, 2004.

[110] V. J. Keast, A. J. Scott, R. Brydson, D. B. Williams, and J. Bruley. Electron energy-loss near-edge structure: a tool for the investigation of electronic structure on the nanometre scale. *Journal of Microscopy*, 203(2):135–175, 2001.

[111] F. Langenhorst and V. L. Solozhenko. Atem-eels study of new diamond-like phases in the b–c–n system. *Physical Chemistry Chemical Physics*, 4(20):5183–5188, 2002.

[112] M. H. Gass, U. Bangert, A. L. Bleloch, P. Wang, R. R Nair, and A. K. Geim. Free-standing graphene at atomic resolution. *Nature Nanotechnology*, 3(11):676–681, 2008.

[113] A. Dato, V. Radmilovic, Z. Lee, J. Phillips, and M. Frenklach. Substrate-free gas-phase synthesis of graphene sheets. *Nano Letters*, 8(7):2012–2016, 2008.

[114] T. Eberlein, U. Bangert, R. Nair, R. Jones, M. Gass, A. Bleloch, K. Novoselov, A. Geim, and P. Briddon. Plasmon spectroscopy of free-standing graphene films. *Physical Review B*, 77(23), 2008.

[115] J. Lu, K. Loh, H. Huang, W. Chen, and A. T. S. Wee. Plasmon dispersion on epitaxial graphene studied using high-resolution electron energy-loss spectroscopy. *Physical Review B*, 80(11):113410, 2009.

[116] Y. H. Wu, T. Yu, and Z. X. Shen. Two-dimensional carbon nanostructures: Fundamental properties, synthesis, characterization, and potential applications. *Journal of Applied Physics*, 108(7):071301, 2010.

[117] P. Larkin. *Infrared and Raman Spectroscopy; Principles and Spectral Interpretation*. Elsevier Science, 2011. ISBN 9780123870186.

[118] J.R. Ferraro. *Introductory Raman Spectroscopy*. Elsevier Science, 2003. ISBN 9780080509129.

[119] P. H. Tan, W. P. Han, W. J. Zhao, Z. H. Wu, K. Chang, H. Wang, Y. F. Wang, N. Bonini, N. Marzari, N. Pugno, et al. The shear mode of multilayer graphene. *Nature Materials*, 11(4):294–300, 2012.

[120] P. Venezuela, M. Lazzeri, and F. Mauri. Theory of double-resonant raman spectra in graphene: Intensity and line shape of defect-induced and two-phonon bands. *Physical Review B*, 84(3):035433, 2011.

[121] J. R. de Laeter, J. K. Böhlke, P. De Bièvre, H. Hidaka, H. S. Peiser, K. J. R. Rosman, and P. D. P. Taylor. Atomic weights of the elements. review 2000 (iupac technical report). *Pure and Applied Chemistry*, 75(6):683–800, 2003.

[122] W. Cai, R. D. Piner, F. J. Stadermann, S. Park, M. A Shaibat, Y. Ishii, D. Yang, A. Velamakanni, S. An, M. Stoller, et al. Synthesis and solid-state nmr structural characterization of ^{13}c-labeled graphite oxide. *Science*, 321(5897):1815–1817, 2008.

[123] S. D. Costa, C. Fantini, A. Righi, A. Bachmatiuk, M. H. Rümmeli, R. Saito, and M. A. Pimenta. Resonant raman spectroscopy on enriched 13c carbon nanotubes. *Carbon*, 49(14):4719–4723, 2011.

[124] X. Li, W. Cai, L. Colombo, and R. S. Ruoff. Evolution of graphene growth on ni and cu by carbon isotope labeling. *Nano Letters*, 9(12):4268–4272, 2009.

[125] M. Kalbac, H. Farhat, J. Kong, P. Janda, L. Kavan, and M. S. Dresselhaus. Raman spectroscopy and in situ raman spectroelectrochemistry of bilayer 12c/13c graphene. *Nano Letters*, 11(5):1957–63, 2011.

[126] J. F. Rodriguez-Nieva, R. Saito, S. D. Costa, and M. S. Dresselhaus. Effect of ^{13}c isotope doping on the optical phonon modes in graphene: Localization and raman spectroscopy. *Physical Review B*, 85(24):245406, 2012.

[127] Junmo Kang, Dolly Shin, Sukang Bae, and Byung Hee Hong. Graphene transfer: key for applications. *Nanoscale*, 4(18):5527–5537, 2012.

[128] A. Reina, H. Son, L. Jiao, B. Fan, M. S. Dresselhaus, Z. Liu, and J. Kong. Transferring and identification of single-and few-layer graphene on arbitrary substrates. *The Journal of Physical Chemistry C*, 112(46):17741–17744, 2008.

[129] X. Liang, B. A. Sperling, I. Calizo, G. Cheng, C. A. Hacker, Q. Zhang, Y. Obeng, K. Yan, H. Peng, Q. Li, X. Zhu, H. Yuan, A. R. Walker, Z. Liu, L. M. Peng, and C. A. Richter. Toward clean and crackless transfer of graphene. *ACS Nano*, 5(11): 9144–53, 2011.

[130] A. Pirkle, J. Chan, A. Venugopal, D. Hinojos, C. W. Magnuson, S. McDonnell, L. Colombo, E. M. Vogel, R. S. Ruoff, and R. M. Wallace. The effect of chemical residues on the physical and electrical properties of chemical vapor deposited graphene transferred to sio2. *Applied Physics Letters*, 99(12):122108, 2011.

[131] T. Hallam, N. C. Berner, C. Yim, and G. S. Duesberg. Strain, bubbles, dirt, and folds: A study of graphene polymer-assisted transfer. *Advanced Materials Interfaces*, 1(6), 2014.

[132] S. Kumar, E. Rezvani, V. Nicolosi, and G. S. Duesberg. Graphene resist interlacing process for versatile fabrication of free-standing graphene. *Nanotechnology*, 23(14): 145302, 2012.

[133] W. Regan, N. Alem, B. Aleman, B. Geng, C. Girit, L. Maserati, F. Wang, M. Crommie, and A. Zettl. A direct transfer of layer-area graphene. *Applied Physics Letters*, 96(11):113102, 2010.

[134] K. W. Urban. Studying atomic structures by aberration-corrected transmission electron microscopy. *Science*, 321(5888):506–510, 2008.

[135] M. Varela, S. D. Findlay, A. R. Lupini, H. M. Christen, A. Y. Borisevich, N. Dellby, O. L. Krivanek, P. D. Nellist, M. P. Oxley, L. J. Allen, et al. Spectroscopic imaging of single atoms within a bulk solid. *Physical Review Letters*, 92(9):095502, 2004.

[136] L. J. Allen, S. D. Findlay, A. R. Lupini, M. P. Oxley, and S. J. Pennycook. Atomic-resolution electron energy loss spectroscopy imaging in aberration corrected scanning transmission electron microscopy. *Physical Review Letters*, 91(10):105503, 2003.

[137] O. L. Krivanek, J. P. Ursin, N. J. Bacon, G. J. Corbin, N. Dellby, P. Hrncirik, M. F. Murfitt, C. S. Own, and Z. S. Szilagyi. High-energy-resolution monochromator for aberration-corrected scanning transmission electron microscopy/electron energy-loss spectroscopy. *Philosophical Transactions A*, 367(1903):3683–3697, 2009.

[138] M. Weyland, P. J. Thomas, and P. A. Midgley. *Advances in High Resolution Elemental Analysis Using Image-Spectroscopy*, pages 163–168. Wiley-VCH Verlag GmbH & Co., 2005. ISBN 9783527606207.

[139] I. Jung, M. Pelton, R. Piner, D. A. Dikin, S. Stankovich, S. Watcharotone, M. Hausner, and R. S. Ruoff. Simple approach for high-contrast optical imaging and characterization of graphene-based sheets. *Nano Letters*, 7(12):3569–3575, 2007.

[140] J. R. McBride, A. R. Lupini, M. A. Schreuder, N. J. Smith, S. J. Pennycook, and S. J. Rosenthal. Few-layer graphene as a support film for transmission electron microscopy imaging of nanoparticles. *ACS Applied Materials Interfaces*, 1(12): 2886–92, 2009.

[141] Z. Lee, K. Jeon, A. Dato, R. Erni, T. J. Richardson, M. Frenklach, and V. Radmilovic. Direct imaging of soft-hard interfaces enabled by graphene. *Nano Letters*, 9(9):3365–3369, 2009.

[142] R. R. Nair, P. Blake, J. R. Blake, R. Zan, S. Anissimova, U. Bangert, A. P. Golovanov, S. V. Morozov, A. K. Geim, K. S. Novoselov, et al. Graphene as a transparent conductive support for studying biological molecules by transmission electron microscopy. *Applied Physics Letters*, 97(15):153102, 2010.

[143] N. R. Wilson, P. A. Pandey, R. Beanland, R. J. Young, I. A. Kinloch, L. Gong, Z. Liu, K. Suenaga, J. P. Rourke, S. J. York, et al. Graphene oxide: structural analysis and application as a highly transparent support for electron microscopy. *ACS Nano*, 3(9):2547–2556, 2009.

[144] Y. Feng, J. Yang, H. Liu, F. Ye, and J. Yang. Selective electrocatalysts toward a prototype of the membraneless direct methanol fuel cell. *Scientific Reports*, 4: 3813, 2014.

[145] N. McEvoy, N. Peltekis, S. Kumar, E. Rezvani, H. Nolan, G. P. Keeley, W. J. Blau, and G. S. Duesberg. Synthesis and analysis of thin conducting pyrolytic carbon films. *Carbon*, 50(3):1216–1226, 2012.

[146] E. Lopez-Honorato, P. J. Meadows, and P. Xiao. Fluidized bed chemical vapor deposition of pyrolytic carbon i. effect of deposition conditions on microstructure. *Carbon*, 47(2):396–410, 2009.

[147] C. Yim, N. McEvoy, E. Rezvani, S. Kumar, and G. S. Duesberg. Carbon-silicon schottky barrier diodes. *Small*, 8(9):1360–1364, 2012.

[148] E. Rezvani, T. Hallam, N. McEvoy, N. C. Berner, and G. S. Duesberg. Optimisation of copper catalyst by the addition of chromium for the chemical vapour deposition growth of monolayer graphene. *Carbon*, 2015.

[149] N. O. Weiss, H. Zhou, L. Liao, Y. Liu, S. Jiang, Y. Huang, and X. Duan. Graphene: an emerging electronic material. *Advanced Materials*, 24(43):5782–825, 2012.

[150] A. W. Tsen, L. Brown, R. W. Havener, and J. Park. Polycrystallinity and stacking in cvd graphene. *Accounts of Chemical Research*, 46(10):2286–2296, 2012.

[151] Z. Han, A. Kimouche, D. Kalita, A. Allain, H. Arjmandi-Tash, A. Reserbat-Plantey, L. Marty, S. Pairis, V. Reita, N. Bendiab, et al. Homogeneous optical and electronic properties of graphene due to the suppression of multilayer patches during cvd on copper foils. *Advanced Functional Materials*, 24(7):964–970, 2014.

[152] M. Kalbac, O. Frank, and L. Kavan. The control of graphene double-layer formation in copper-catalyzed chemical vapor deposition. *Carbon*, 50(10):3682–3687, 2012.

[153] Y. Cheolashin et al. Application of tungsten as a carbon sink for synthesis of large-domain uniform monolayer graphene free of bilayers/multilayers. *Nanoscale*, 7(11):4929–4934, 2015.

[154] S. Hurch, H. Nolan, T. Hallam, N. C. Berner, N. McEvoy, and G. S. Duesberg. Inkjet-defined field-effect transistors from chemical vapour deposited graphene. *Carbon*, 71:332–337, 2014.

[155] R. S. Weatherup, B. C. Bayer, R. Blume, C. Ducati, C. Baehtz, R. Schlogl, and S. Hofmann. In situ characterization of alloy catalysts for low-temperature graphene growth. *Nano Letters*, 11(10):4154–60, 2011.

[156] O. Frank, L. Kavan, and M. Kalbac. Carbon isotope labelling in graphene research. *Nanoscale*, 6(12):6363–6370, 2014.

[157] Q. Li, H. Chou, J. H. Zhong, J. Y. Liu, A. Dolocan, J. Zhang, Y. Zhou, R. S. Ruoff, S. Chen, and W. Cai. Growth of adlayer graphene on cu studied by carbon isotope labeling. *Nano Letters*, 13(2):486–90, 2013.

[158] C. W. Bauschlicher. *Transition Metals: Applications*. John Wiley & Sons, Ltd, 2002. ISBN 9780470845011.

[159] L. Toth. *Transition Metal Carbides and Nitrides*. Elsevier Science, 2014. ISBN 9780323157223.

[160] S. T. Oyama. Preparation and catalytic properties of transition metal carbides and nitrides. *Catalysis Today*, 15(2):179–200, 1992.

[161] S.T. Oyama. *The Chemistry of Transition Metal Carbides and Nitrides*. NATO Science Series C. Springer, 1996. ISBN 9780751403657.

[162] M. D. Healy, D. C. Smith, R. R. Rubiano, N. E. Elliott, and R. W. Springer. Use of tetraneopentylchromium as a precursor for the organometallic chemical vapor deposition of chromium carbide: a reinvestigation. *Chemistry of Materials*, 6(4): 448–453, 1994.

[163] A. Kalemos, T. H. Dunning Jr, and A. Mavridis. First principles investigation of chromium carbide, crc. *The Journal of Chemical Physics*, 123(1):014302, 2005.

[164] H. Lin, P. K. Nayak, S. Wang, S. Chang, and J. Huang. Electron-energy loss spectroscopy and raman studies of nanosized chromium carbide synthesized during carbothermal reduction process from precursor cr(co)$_6$. *Journal of the European Ceramic Society*, 31(14):2481–2487, 2011.

[165] Z. Zhao, H. Zheng, Y. Wang, S. Mao, J. Niu, Y. Chen, and M. Shang. Synthesis of chromium carbide (cr3c2) nanopowders by the carbonization of the precursor. *International Journal of Refractory Metals and Hard Materials*, 29(5):614–617, 2011.

[166] W. Zhu, T. Low, V. Perebeinos, A. A. Bol, Y. Zhu, H. Yan, J. Tersoff, and P. Avouris. Structure and electronic transport in graphene wrinkles. *Nano Letters*, 12(7):3431–3436, 2012.

[167] C. Wang, Y. Liu, L. Lan, and H. Tan. Graphene wrinkling: formation, evolution and collapse. *Nanoscale*, 5(10):4454–4461, 2013.

[168] H. Seiler. Secondary electron emission in the scanning electron microscope. *Journal of Applied Physics*, 54(11):R1–R18, 1983.

[169] L. Martin, H. Martinez, D. Poinot, B. Pecquenard, and F. Le Cras. Comprehensive x-ray photoelectron spectroscopy study of the conversion reaction mechanism of cuo in lithiated thin film electrodes. *The Journal of Physical Chemistry C*, 117 (9):4421–4430, 2013.

[170] G. C. Allen and P. M. Tucker. Multiplet splitting of x-ray photoelectron lines of chromium complexes. the effect of covalency on the 2p core level spin-orbit separation. *Inorganica Chimica Acta*, 16:41–45, 1976.

[171] Y. Zhang, L. Zhang, and C. Zhou. Review of chemical vapor deposition of graphene and related applications. *Accounts of Chemical Research*, 46(10):2329–2339, 2013.

[172] A.C. Jones and M.L. Hitchman. *Chemical Vapour Deposition: Precursors, Processes and Applications*. Royal Society of Chemistry, 2009. ISBN 9780854044658.

[173] C. Wu, F. Li, W. Chen, C. P. Veeramalai, P. Ooi, and . Guo. Electromagnetic induction heating for single crystal graphene growth: morphology control by rapid heating and quenching. *Scientific Reports*, 5:9034–9039, 2015.

[174] Y. Zhang, L. Zhang, P. Kim, M. Ge, Z. Li, and C. Zhou. Vapor trapping growth of single-crystalline graphene flowers: synthesis, morphology, and electronic properties. *Nano Letters*, 12(6):2810–2816, 2012.

[175] W. Zhang, P. Wu, Z. Li, and J. Yang. First-principles thermodynamics of graphene growth on cu surfaces. *The Journal of Physical Chemistry C*, 115(36):17782–17787, 2011.

[176] P. R. Kidambi, B. C. Bayer, R. Blume, Z. Wang, C. Baehtz, R. S. Weatherup, M. G. Willinger, R. Schloegl, and S. Hofmann. Observing graphene grow: Catalyst-graphene interactions during scalable graphene growth on polycrystalline copper. *Nano Letters*, 13(10):4769–4778, 2013.

[177] J. Bigeleisen and M. Wolfsberg. *Theoretical and Experimental Aspects of Isotope Effects in Chemical Kinetics*, pages 15–76. John Wiley & Sons, Inc., 2007. ISBN 9780470143476.

[178] A. C. Ferrari. Raman spectroscopy of graphene and graphite: disorder, electron-phonon coupling, doping and nonadiabatic effects. *Solid State Communications*, 143(1-2):47–57, 2007.

[179] L. G. Cancado, A. Jorio, E. H. Ferreira, F. Stavale, C. A. Achete, R. B. Capaz, M. V. Moutinho, A. Lombardo, T. S. Kulmala, and A. C. Ferrari. Quantifying defects in graphene via raman spectroscopy at different excitation energies. *Nano Letters*, 11(8):3190–6, 2011.

[180] Y. Hao, Y. Wang, L. Wang, Z. Ni, Z. Wang, R. Wang, C. K. Koo, Z. Shen, and J. T. Thong. Probing layer number and stacking order of few-layer graphene by raman spectroscopy. *Small*, 6(2):195–200, 2010.

[181] C. Casiraghi. Doping dependence of the raman peaks intensity of graphene close to the dirac point. *Physical Review B*, 80(23), 2009.

[182] M. Kalbac, A. Reina-Cecco, H. Farhat, J. Kong, L. Kavan, and M. S. Dresselhaus. The influence of strong electron and hole doping on the raman intensity of chemical vapor-deposition graphene. *ACS Nano*, 4(10):6055–6063, 2010.

[183] M. Mukai, J. S. Kim, K. Omoto, H. Sawada, A. Kimura, A. Ikeda, J. Zhou, T. Kaneyama, N. P. Young, J. H. Warner, et al. The development of a 200kv monochromated field emission electron source. *Ultramicroscopy*, 140:37–43, 2014.

[184] P. D. Nellist and A. I. Kirkland. Applications of the oxford-jeol aberration-corrected electron microscope. *Philosophical Magazine*, 90(35-36):4751–4767, 2010.

[185] F. Banhart. Irradiation effects in carbon nanostructures. *Reports on Progress in Physics*, 62(8):1181, 1999.

[186] R. F. Egerton, P. Li, and M. Malac. Radiation damage in the tem and sem. *Micron*, 35(6):399–409, 2004.

[187] J. S. Kim, K. B. Borisenko, V. Nicolosi, and A. I. Kirkland. Controlled radiation damage and edge structures in boron nitride membranes. *ACS Nano*, 5(5):3977–3986, 2011.

[188] J. C. Meyer, F. Eder, S. Kurasch, V. Skakalova, J. Kotakoski, H. Park, S. Roth, A. Chuvilin, S. Eyhusen, G. Benner, et al. Accurate measurement of electron beam induced displacement cross sections for single-layer graphene. *Physical Review Letters*, 108(19):196102, 2012.

[189] E.V. Anslyn and D.A. Dougherty. *Modern Physical Organic Chemistry.* University Science, 2006. ISBN 9781891389313.

[190] M. Carravetta, M. Eden, O. G. Johannessen, H. Luthman, P. J. E. Verdegem, J. Lugtenburg, A. Sebald, and M. H. Levitt. Estimation of carbon-carbon bond lengths and medium-range internuclear distances by solid-state nuclear magnetic resonance. *Journal of the American Chemical Society*, 123(43):10628–10638, 2001.

[191] X. Jia, J. Campos-Delgado, M. Terrones, V. Meunier, and M. S. Dresselhaus. Graphene edges: a review of their fabrication and characterization. *Nanoscale*, 3 (1):86–95, 2011.

[192] Z. Liu, K. Suenaga, P. J. F. Harris, and S. Iijima. Open and closed edges of graphene layers. *Physical Review Letters*, 102(1):015501, 2009.

[193] P. Vancsó, G. I. Márk, P. Lambin, A. Mayer, C. Hwang, and L. P. Biró. Effect of the disorder in graphene grain boundaries: A wave packet dynamics study. *Applied Surface Science*, 291:58–63, 2014.

[194] J. da Silva-Araújo, A. J. M. Nascimento, H. Chacham, and R. W. Nunes. Non-hexagonal-ring defects and structures induced by healing and strain in graphene and functionalized graphene. *Nanotechnology*, 24(3):035708, 2013.

[195] J. Kotakoski, D. Santos-Cottin, and A. V. Krasheninnikov. Stability of graphene edges under electron beam: equilibrium energetics versus dynamic effects. *ACS Nano*, 6(1):671–676, 2011.

[196] N. D. Browning, D. J. Wallis, P. D. Nellist, and S. J. Pennycook. Eels in the stem: Determination of materials properties on the atomic scale. *Micron*, 28(5):333–348, 1997.

[197] J. Song, M. Alam, A. L. Boehman, and U. Kim. Examination of the oxidation behavior of biodiesel soot. *Combustion and Flame*, 146(4):589–604, 2006.

[198] S. Tomita, M. Fujii, S. Hayashi, and K. Yamamoto. Electron energy-loss spectroscopy of carbon onions. *Chemical Physics Letters*, 305(3):225–229, 1999.

[199] Y. Lifshitz. Diamond-like carbon: present status. *Diamond and Related materials*, 8(8):1659–1676, 1999.

[200] D. R. McKenzie, D. Muller, and B. A. Pailthorpe. Compressive-stress-induced formation of thin-film tetrahedral amorphous carbon. *Physical Review Letters*, 67 (6):773, 1991.

[201] K. Suenaga, E. Sandre, C. Colliex, C. J. Pickard, H. Kataura, and S. Iijima. Electron energy-loss spectroscopy of electron states in isolated carbon nanostructures. *Physical Review B*, 63(16):165408, 2001.

[202] K. Suenaga, M. Tence, C. Mory, C. Colliex, H. Kato, T. Okazaki, H. Shinohara, K. Hirahara, S. Bandow, and S. Iijima. Element-selective single atom imaging. *Science*, 290(5500):2280–2282, 2000.

[203] T. Okazaki, K. Suenaga, K. Hirahara, S. Bandow, S. Iijima, and H. Shinohara. Real time reaction dynamics in carbon nanotubes. *Journal of the American Chemical Society*, 123(39):9673–9674, 2001.

[204] K. Kwon, K. Choi, and S. Kim. Increased work function in few-layer graphene sheets via metal chloride doping. *Advanced Functional Materials*, 22(22):4724–4731, 2012.

[205] H. Medina, Y. Lin, D. Obergfell, and P. Chiu. Tuning of charge densities in graphene by molecule doping. *Advanced Functional Materials*, 21(14):2687–2692, 2011.

[206] L. Yan, Y. Zheng, F. Zhao, S. Li, X. Gao, B. Xu, P. S. Weiss, and Y. Zhao. Chemistry and physics of a single atomic layer: strategies and challenges for functionalization of graphene and graphene-based materials. *Chemical Society Reviews*, 41(1):97–114, 2012.

[207] X. Wang, X. Li, L. Zhang, Y. Yoon, P. K. Weber, H. Wang, J. Guo, and H. Dai. N-doping of graphene through electrothermal reactions with ammonia. *Science*, 324(5928):768–771, 2009.

[208] D. R. Kauffman and A. Star. Graphene versus carbon nanotubes for chemical sensor and fuel cell applications. *Analyst*, 135(11):2790–2797, 2010.

[209] Z. Lin, M. Song, Y. Ding, Y. Liu, M. Liu, and C. Wong. Facile preparation of nitrogen-doped graphene as a metal-free catalyst for oxygen reduction reaction. *Physical Chemistry Chemical Physics*, 14(10):3381–3387, 2012.

[210] L. Qu, Y. Liu, J. Baek, and L. Dai. Nitrogen-doped graphene as efficient metal-free electrocatalyst for oxygen reduction in fuel cells. *ACS Nano*, 4(3):1321–1326, 2010.

[211] A. L. M. Reddy, A. Srivastava, S. R. Gowda, H. Gullapalli, M. Dubey, and P. M. Ajayan. Synthesis of nitrogen-doped graphene films for lithium battery application. *ACS Nano*, 4(11):6337–6342, 2010.

[212] L. Lai, J. R. Potts, D. Zhan, L. Wang, C. Poh, C. Tang, H. Gong, Z. Shen, J. Lin, and R. S. Ruoff. Exploration of the active center structure of nitrogen-doped graphene-based catalysts for oxygen reduction reaction. *Energy & Environmental Science*, 5(7):7936–7942, 2012.

[213] H. Peng, Z. Mo, S. Liao, H. Liang, L. Yang, F. Luo, H. Song, Y. Zhong, and B. Zhang. High performance fe-and n-doped carbon catalyst with graphene structure for oxygen reduction. *Scientific Reports*, 3, 2013.

[214] Y. Zhang, K. Fugane, T. Mori, L. Niu, and J. Ye. Wet chemical synthesis of nitrogen-doped graphene towards oxygen reduction electrocatalysts without high-temperature pyrolysis. *Journal of Materials Chemistry*, 22(14):6575–6580, 2012.

[215] D. Wei, Y. Liu, Y. Wang, H. Zhang, L. Huang, and G. Yu. Synthesis of n-doped graphene by chemical vapor deposition and its electrical properties. *Nano Letters*, 9(5):1752–1758, 2009.

[216] L. S. Panchakarla, K. S. Subrahmanyam, S. K. Saha, A. Govindaraj, H. R. Krishnamurthy, U. V. Waghmare, and C. N. R. Rao. Synthesis, structure, and properties of boron-and nitrogen-doped graphene. *Advanced Materials*, 21(46): 4726–4730, 2009.

[217] A. Hirsch, J. M. Englert, and F. Hauke. Wet chemical functionalization of graphene. *Accounts of Chemical Research*, 46(1):87–96, 2012.

[218] Y. Wang, Y. Shao, D. W. Matson, J. Li, and Y. Lin. Nitrogen-doped graphene and its application in electrochemical biosensing. *ACS Nano*, 4(4):1790–1798, 2010.

[219] R. Brydson. *Nanocharacterisation*, chapter Electron energy-loss spectroscopy and energy dispersive X-ray analysis, pages 94–137. Number 9780854042418 in RSC nanoscience and nanotechnology. RSC Publishing, 2007.

[220] Z. Zhang, R. Brydson, Z. Aslam, S. Reddy, A. Brown, A. Westwood, and B. Rand. Investigating the structure of non-graphitising carbons using electron energy loss spectroscopy in the transmission electron microscope. *Carbon*, 49(15):5049–5063, 2011.

[221] Z. Zhang, R. Brydson, S. Reddy, A. Westwood, A. Brown, and B. Rand. Nanostructural development of non-graphitising carbons probed using tem/eels: The importance of fullerenes? In *Journal of Physics: Conference Series*, volume 241, page 012094. IOP Publishing, 2010.

[222] R. F. Egerton. Electron energy-loss spectroscopy in the tem. *Reports on Progress in Physics*, 72(1):016502, 2009.

[223] C. C. Ahn. *Transmission Electron Energy Loss Spectrometry in Materials Science and the EELS Atlas*. Wiley, 2006. ISBN 9783527604777.

[224] R. F. Egerton and M. J. Whelan. Electron energy loss spectra of diamond, graphite and amorphous carbon. *Journal of Electron Spectroscopy and Related Phenomena*, 3(3):232–236, 1974.

[225] S. D. Berger, D. R. McKenzie, and P. J. Martin. Eels analysis of vacuum arc-deposited diamond-like films. *Philosophical Magazine Letters*, 57(6):285–290, 1988.

[226] J. J. Cuomo, J. P. Doyle, J. Bruley, and J. C. Liu. Sputter deposition of dense diamond-like carbon films at low temperature. *Applied Physics Letters*, 58(5): 466–468, 1991.

[227] L. Wan and R. F. Egerton. Preparation and characterization of carbon nitride thin films. *Thin Solid Films*, 279(1):34–42, 1996.

[228] A. J. Papworth, C. J. Kiely, A. P. Burden, S. R. P. Silva, and G. A. J. Amaratunga. Electron-energy-loss spectroscopy characterization of the sp 2 bonding fraction within carbon thin films. *Physical Review B*, 62(19):12628, 2000.

[229] J. T. Titantah and D. Lamoen. Technique for the sp^2/ sp^3 characterization of carbon materials: Ab initio calculation of near-edge structure in electron-energy-loss spectra. *Physical Review B*, 70(7):075115, 2004.